

Towards a read-out
for capacitive displacement sensor
in an engineered heart tissue device

Towards a read-out for capacitive sensor in an EHT device

Filippo Pfaiffer



Filippo Pfaiffer

Towards a read-out for capacitive displacement sensor in an engineered heart tissue device

By

Filippo Pfaiffer

f.pfaiffer@student.tudelft.nl

Student n. 5368308

in partial fulfilment of the requirements for the degree of

Master of Science
in Electrical Engineering

at the Delft University of Technology,
to be defended publicly on Monday, November 28, 2022, at 3.30 PM.

Supervisor:	Dr. M. Mastrangeli,	TU Delft
Daily Supervisors:	M. Dostanic,	TU Delft
	Prof. dr. ir. G. C. M. Meijer,	TU Delft
Thesis committee:	Prof. dr. P.M. Sarro,	TU Delft
	Prof. dr. ir. W. Serdijn,	TU Delft

This thesis is confidential and cannot be made public until December 31st, 2023.

An electronic version of this thesis is available at <http://repository.tudelft.nl/>.



Alle parole che non escono

*E a Gina,
Che faceva poco rumore
Che rendeva il mondo un po' più leggero
E che ha provato fino all'ultimo a insegnarmi a fare altrettanto*

Abstract

Engineered Heart Tissues (EHTs) are a valuable approach enabled by Organ-on-Chip (OoC) technology to model human cardiac tissue. These small microfluidic devices allow the culture and development of living cardiac cells in 3D structures, to reproduce tissue dynamics and functionality in-vitro, thus fostering the development of new and more precise models for human diseases and organs' physiological response.

One of the most important gaps in this recent technology is the lack of integration of electronic devices in the platforms, such as electrodes for tissue stimulation or sensors for real-time monitoring of the tissue.

To cover this gap, a polymer-based platform with microwell and micropillars for culturing EHTs and measuring their contractile properties was developed in ECTM group at TU Delft. The contraction force exerted by the beating cardiac tissue, self-assembled around the micropillars, is quantified by measuring the displacement of the micropillars with spiral capacitive sensors embedded in the substrate. The force generated by the tissue corresponds to a capacitance change which is simulated to be in the aF range, requiring a high-precision, sensitive, and portable read-out circuitry.

The investigation and development of this readout electronics is the final goal of this Master Thesis. A literature survey about possible capacitive readout techniques was conducted to identify suitable architectures for measuring such small dynamic changes in capacitance. Two solutions available on the market (Smarte UTI and Analog Devices AD7746) implementing two of these architectures were chosen, tested, and characterised. Benchmark measurements with accurate laboratory instrumentation were performed, and noise figures of the two solutions were evaluated.

To allow the readout, EHT platforms with embedded sensors need to be transferred and assembled on a custom Printed Circuit Board (PCB): the viability of this challenging assembly process was evaluated. The multiple constraints deriving from such a complex project determined the development of a non-standard assembly process, which proved to be delicate and gave origin to multiple failure modes. Those were documented and analysed, to identify alternative or improved assembly procedures which need to be developed to fabricate reliable samples, since these weaknesses were identified as the most critical aspect at this point of the project.

The results obtained showed how the two solutions for the readout provided results in good agreement with more precise non-portable laboratory instrumentation, and promising noise figures. The platforms with embedded sensors were successfully transferred to the developed PCBs, and measurements showed good agreement with the simulated static behaviour of the sensors, thus providing a valuable proof-of-concept for the whole project.

The dynamic behaviour of the sensors was preliminarily investigated and characterized using nanoindentation tests, indicating the possibility to measure a linear relationship between the force applied and the difference in the sensed capacitance. Despite this good result, further tests need to be performed to verify it and to address some criticalities that were identified.

Cardiac tissue was cultured on platforms with integrated sensors and the biocompatibility of the entire system was proved. The behaviour of the sensors during biological measurement with cardiac cells is left to future investigation.

Acknowledgements

I always thought that writing these few lines would have been the easiest task of my whole scholastic path. But now I find myself sitting in front of a semi-white sheet and sentences struggle to stick on the page. I guess it is because I would like to find the perfect words to express my gratitude to every single of the countless people I shared my path with, but the truth is “things rarely go exactly the way you want them to, so sometimes you make do with whatever you can get”, which is also one of the broadest and most relatable lessons learned from the work contained in this book. So, let me start with those who helped me to complete this work.

Above all, I would like to express my deepest gratitude to my supervisors Massimo Mastrangeli and Milica Dostanic for trusting me and for being my guidance during the last year. Every suggestion I received from you was a treasure, and your restless passion for your daily research was inspirational. Thank you for pushing me to never give up, especially when I only wanted to frustratingly stop in front of what looked like an insurmountable wall. You brought out the best part of me. I really enjoyed working on your side in this extraordinary research field, and I appreciate your every single effort on the road to make this world a better – and healthier – place.

I would also like to thank Professor Gerard Meijer for his spontaneous and heart-warming support in every step of my work. Our discussions were among the most fascinating and formative experiences I was gifted with, and your experienced help was a lighthouse in the darkest nights. The world needs more people like you.

I also want to thank those who created perfect “boundary conditions” to reach this achievement.

In first place thanks to the Netherlands – for the wind that stepped up my cycling skills – for the rain that soaked my clothes but not my spirit – for the tulips that blossomed every spring regardless of the winter hardness – and for the lovely hospitality that often warmed my heart.

To my flatmates: thanks for sharing our paths, finding you was the biggest luck I could ask for. I hope I left you at least a part of what you left me. Hippo is, and will always be, home.

Thanks to Bas for being one of the reasons why TU Delft got on my radar, and for giving me The Goldfinch, which accomplished its task and might now retire happily.

And now, finally, to the most important people in my life.

To my grandparents, for creating the amazing group of people that I call family, and that makes it so heavy to take every single VCE-AMS plane – *“How lucky I am to have something that makes saying goodbye so hard”* – and to mamma e papà, for their unconditioned support, far from being only financial, for their love, for their understanding, for always being my safe harbour, and above all for raising me with values that make me feel appreciated in every path I walk worldwide.

To my sister Federica, for being for 25 years (and many more to come) my model and my answer to the question “how do you wish to be in five years?”, and to Tullio for being an acquired brother and for talking sense and courage into me in one of the darkest days. I will always remember it.

Last, but never least, to Anna for allowing me to see clearly in the shade. Literally - thanks to the coolest glasses ever - and figuratively - thanks to the ability to always clear my mind and guide me to the right solution. Thanks for being back into my life, for waiting for me every single day, for understanding me and bearing with my bad temper. And finally, for being my personal graphic designer in the last couple of weeks.

If I have to sum up the last two years with one word I would probably say “intense”, in every possible meaning that this word might have. Thanks to Henley for the continuous reminder to be unbowed in the fell clutch of circumstances, and thanks to the fate, or to however you want to call it, for bringing me to a point where the future does not scare me anymore. On the 22nd of August 2020, a young boy was hopping on a plane to Amsterdam. He did not know what he was looking for, but he was full of hopes and expectations. Two years later, he looks back at it with a bag full of satisfied expectations. He now knows what he was looking for, and he is sure and proud when he says that he found it. He is one - or many - steps closer to being an adult.

F. Pfaffner
Delft, November 2022

Table of Contents

Abstract.....	v
Acknowledgements.....	vii
Introduction.....	1
1.1. Background.....	1
1.2. Engineered Heart Tissue at TU Delft.....	2
1.3. Integration of displacement sensors in the EHT.....	3
1.4. Aim of this thesis.....	4
1.5. Thesis structure.....	4
Previous works.....	5
2.1. The EHT Platform at TU Delft.....	5
2.1.1 Design.....	5
2.1.2 Microfabrication.....	6
2.1.3 Measurements of pillar displacement.....	7
2.2. Integration of capacitive displacement sensors.....	8
2.2.1 Design.....	9
2.2.2 Microfabrication.....	10
2.2.3 Simulations.....	12
2.3. Visual inspection and measurements.....	13
Capacitive Readout.....	15
3.1. Introduction to capacitive sensing.....	15
3.2. Specific techniques for accurate readout.....	16
3.2.1 Chopping.....	16
3.2.2 Autocalibration.....	17
3.2.3 Four-point measurement.....	18
3.3. Architectures for capacitive readout.....	18
3.3.1 Capacitance to Current.....	19
3.3.2 Capacitance to Frequency.....	20
3.3.3 Capacitance to Time.....	20
3.3.4 Capacitance to Voltage.....	21
3.3.5 Capacitance to Digital.....	24
3.4. Comparison and conclusions.....	25
Commercial solutions: UTI and AD7746.....	27
4.1. Smartec UTI.....	27
4.1.1 Architecture and functionalities.....	28
4.1.2 Interfacing.....	30
4.1.3 Improvements.....	31

4.2. Analog Devices AD7746.....	32
4.2.1 Architecture and functionalities.....	33
4.2.2 Interfacing.....	34
4.3. Preliminary tests: accuracy.....	34
4.3.1 Static benchmarking.....	34
4.3.2 Investigation of variable capacitors and dynamic benchmarking.....	36
4.4. Preliminary tests: Noise behaviour.....	38
4.4.1 Johnson-Nyquist noise.....	39
4.4.2 Flicker noise.....	40
4.4.3 Quantization noise.....	40
4.4.4 Noise analysis.....	41
4.5. Conclusion and final choice.....	42
System Fabrication and Assembly.....	43
5.1. PCB Design.....	43
5.2. The assembly procedure.....	46
5.3. Mechanical failure modes.....	47
5.3.1 Failures related to wire bonding.....	49
5.3.2 Failures related to detachment from the wafer.....	49
5.4. Improved assembly procedure.....	51
5.5. Final assembly steps.....	52
5.6. Interconnects and external disturbances.....	53
Measurements and system characterization.....	55
6.1. Base Capacitance.....	55
6.2. Electrical failure modes.....	57
6.3. Results after improved assembly.....	60
6.4. Manual pillar displacement.....	62
6.5. Nanoindentation.....	63
6.5.1 Discussion of the results.....	68
6.6. Cell culture and biological measurements.....	69
Conclusions and outlook.....	71
7.1. Conclusions.....	71
7.2. Suggestions for future works.....	72
References.....	77
Appendix A.....	- 1 -
A.1 Introduction.....	- 1 -
A.2. Organs-on-Chip.....	- 2 -
A.2.1 Reasons for the development.....	- 3 -
A.2.2 A multidisciplinary field.....	- 5 -

A.2.3 Different types of OoC	- 6 -
A.2.4 Gaps and unmet needs	- 7 -
A.2.5 Next steps to be taken	- 7 -
A.3. Engineered Heart Tissue	- 8 -
A.3.1 Different platforms for EHT and HoC.....	- 8 -
A.4. Summary	- 12 -
References.....	- 13 -
Appendix B.....	- 15 -
B.1. Capacitive board	- 16 -
B.1.1 Version 1	- 16 -
B.1.2 Version 2	- 17 -
B.2. UTI_To_Ali Board	- 18 -
B.3. EHT_Wire_bonding board.....	- 19 -
B.3.1 Version 1	- 19 -
B.3.2 Version 2	- 20 -
B.3.3 Version 3	- 21 -
B.4. Inverter_Buffer Board.....	- 22 -
Appendix C.....	- 25 -
Appendix D.....	- 27 -
Appendix E.....	- 31 -
Appendix F.....	- 33 -
Appendix G.....	- 35 -
Appendix H.....	- 37 -
Appendix I.....	- 39 -
Appendix J.....	- 41 -
Appendix K.....	- 43 -

Introduction

In this brief chapter, a general introduction to this Master Thesis is provided. The reader will first be guided through the background information related to the research field, and then through the basic ideas that stand behind the development of this project. A first work related to the development of a Heart-on-Chip device in the ECTM group of TU Delft will be presented, followed by an explanation of an improvement that was implemented during a second work. The needs deriving from these two studies, together with the information related to the background, will serve as input to highlight the motivations of this thesis, and consequentially will be used to define its aims. After that, a short outline of this thesis will be provided.

1.1. Background

In the last years, the number of published papers concerning Organs-on-Chip (OoC) constantly increased, reflecting the interest that this new research field aroused [1]. OoC are small microfluidics devices that allow the culture and development of living human cells in 3D structures. These microdevices allow easy control of the culture environment and of the stimuli received by the cultured tissues, which mimic one or more aspects of the organ's dynamics, functionality, and physiological response [2]. At present, drug development strictly relies on animal testing and on 2D cell cultures that often derive from a single ethnical group, making drugs ineffective on a large part of the population and precluding the road to personalized medicine [3]. In many cases, disease models developed using previous technologies and protocols are not sufficiently accurate, leading to the impossibility to find cures or drugs that are effective against certain diseases. Moreover, drugs development process is becoming long and expensive and, according to the trends, this will keep worsening unless innovative technologies and paradigms – like OoC – will be developed [3].

Many different organs and tissues have been reproduced on-chip in the last decade, to provide better models for their functionalities and to assess platforms' suitability for drug testing. Among all the organs that have been investigated, special attention is given to Heart-on-Chip devices: cardiac diseases are the main cause of death in western society, and cardiotoxicity is often discovered in the late stages of drug development, highlighting therefore the urgent need to develop more precise models for cardiac physiology [4].

Multiple Heart-on-Chip platforms have been developed in the last years, and devices with different structures and shapes can be found in the literature. The general trend is to develop devices with pillars, scaffolds, cavities, and other mechanical structures that allow the stimulation of the tissue, in order to study its dynamic properties [5]. This stimulation is often mechanical and relates to the force that these mechanical structures exert on the tissues - for example creating a reaction to the natural

contraction of healthy cardiac tissue. Many studies proved that, thanks to this stimulation, tissues are fully developed and that their dynamics and physiology can be investigated with good relevance [6]. In the context of these studies, aimed to assess the contractile properties of EHTs, a platform was developed at TU Delft.

1.2. Engineered Heart Tissue at TU Delft

The project relates to the development of an Engineered Heart Tissue (EHT) device, which is an OoC platform suitable for the culture of heart cells: such a device was developed in the ECTM group of TU Delft by M. Dostanic in 2018 [7]. The device is made by an elastic Polydimethylsiloxane (PDMS) substrate and by an elliptical PDMS microwell whose function is to confine the medium needed to culture cardiac cells derived from stem cells. Inside this microwell, two flexible PDMS micropillars serve as an anchoring point for the self-assembly of the cells and, in a later stage, as a mechanical reaction to the autonomous contraction of the tissue. In Figure 1.1 a 3D model of the platform is shown, in which the PDMS substrate, microwell, and pillars can be seen in turquoise, and the formed cardiac tissue is highlighted in brown.

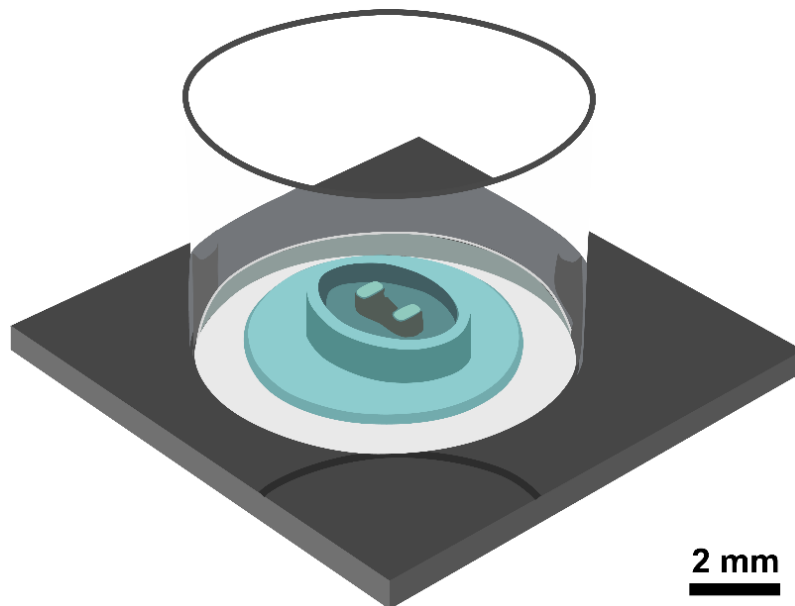


Figure 1.1: The EHT platform developed at TU Delft (Derived from [7]).

After assembly around the micropillars, a healthy EHT autonomously starts to contract periodically, thus exerting force on the micropillars, causing a deflection of the pillars and substrate deformation.

This study is framed in the background explained earlier: a platform with two pillars whose aim is to provide mechanical stimulation of cardiac tissue, with the final aim to exploit the information derived from the deflection of the pillars in order to gain information on EHT dynamics, thus assessing contractile properties of the tissue.

In general, in the OoC scenario, the stimulation of the tissue is very often exclusively mechanical, and only in the last years research showed the trend to shift towards the use of both mechanical stimulation and electrical stimulation (pacing), which proved to favour a faster and more complete maturation of the tissue [8]. Despite this trend, very few studies investigated the possibility to integrate devices for electrical stimulation (pacing electrodes) in the platforms. Even fewer studies investigated the possibility to integrate sensors for real-time monitoring of the cells, which could at

first refine and then replace the main technique used for measurements, that currently is optical displacement tracking.

This gap in the current OoC technology served as motivation for a complementary study conducted at TU Delft in relation to the previously developed EHT device: the integration of sensors embedded in the platform to allow real-time monitoring of the cells' behaviour.

1.3. Integration of displacement sensors in the EHT

One of the possibilities to gain precise information about the motion of an EHT platform is to embed a sensor in its substrate, which is a breakthrough and challenging solution still not explored in the literature. This idea gave origin to a second work that is related to the one conducted by Dostanic, and that constitutes a base for this Master Thesis: the design and fabrication of capacitive sensors integrated into the EHT platform, which allow real-time measurement of the behaviour of cultured cells. This second work was conducted by Shojaei Baghini in 2020 [9]. The design of coplanar capacitive sensors patterned in a spiral shape was chosen due to the higher responsivity of this solution compared to other alternatives. These sensors exploit the fringe-field effect generated by the interdigitated traces of the spirals to generate a capacitor. The value of this capacitor changes because of the deformation applied to the spiral. The positioning of the sensors also played a significant role in the design of the solution: these spirals were integrated into the PDMS substrate just below the pillar base, because pillar deflection also causes a deformation in the substrate (which therefore causes a change in the shape of the spirals). This change in the shape is eventually associated with a change in capacitance. A 3D model of the integration of one spiral capacitor below one pillar of the platform is shown in Figure 1.2.

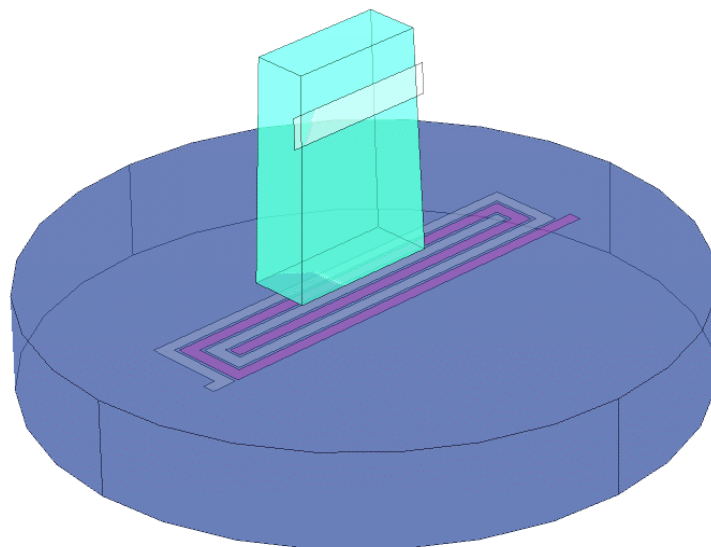


Figure 1.2: Spiral capacitive sensors integrated into the EHT substrate (Derived from [9]).

The developed sensors provide in principle high responsivity, but the expected force applied by the cardiac tissues is very small (in the order of 10-100 μN), and this translates to a worst-case expected change in the base capacitance of the sensors of around 10-100 aF. Detection of such a small capacitance change requires a sensitive and high-precision read-out circuit, which was the main motivation for the development of this Master Thesis.

1.4. Aim of this thesis

As explained, this whole project was developed as a response to the stimuli and to the challenges that OoC's vivid research field offers, and this Master Thesis is configured as a follow-up of multiple works previously conducted at Delft University of Technology.

The highlighted gap related to the lack of integration of electronics in the platform gave origin to the just explained investigation, and the technical challenges that emerged in relation to that work originated the need to develop this Master Thesis.

The motivations of this study are to fill the above-mentioned gap, investigating the possibility to fabricate and exploit sensors integrated into the EHT platform for tissue characterization, and in detail to overcome the technical challenges provided by the readout of a capacitive sensor with an expected change in the aF range.

The objectives of the thesis are therefore to:

- **Assess the feasibility and viability of the integrated displacement sensor approach**, providing important proofs-of-concept and highlighting possible obstacles (also concerning the manufacturability of such an approach). Devices will be brought from the end of sensor manufacturing to the final application (cell culture), and suggestions that will pave the road for further developments in the same project scope will be provided.
- **Research a sensitive, high-precision, and portable read-out strategy**, allowing the final characterization of the system, and consequently the measurement of cells' behaviour. This will be done by investigating read-out architectures suitable to overcome the challenging requirements of the sensors derived from the downscaling of the EHT platform and from its intrinsically multi-disciplinary domain, selecting the most suitable strategy, and testing first its suitability and finally its behaviour in the final application.

1.5. Thesis structure

This brief introduction provided an overview of the OoC scenario and of its challenges. A detailed literature review on OoC and on several types of Heart-on-Chip devices that have been developed in the last years was conducted to highlight the trends in this research field, and is reported in Appendix A.

After this brief introduction, in Chapter 2 a more detailed explanation of the work that was previously performed at TU Delft on EHTs will be given, providing a solid base for the reader to understand the following chapters. Chapter 3 will relate to capacitive readout, showing suitable architectures found in the literature and specific techniques aimed to increase the quality of the readout.

This literature survey led to the selection of two suitable components, whose functionalities will be shown in Chapter 4 together with the first set of analyses, aimed to verify their suitability for the needed application.

Chapter 5 will be dedicated to the complex assembly process that is needed to allow the routing of the input and output signals of the sensors, and to all the challenges related to it.

The results of the static characterization of the platform and the preliminary evaluation of the dynamic characterization will be treated in Chapter 6.

Finally, in Chapter 7 conclusions will be drawn and suggestions for future works will be provided.

Previous works

In this chapter, a more detailed presentation of the two works that constitute the starting point for this Master Thesis will be given. The development of an EHT platform is treated by evaluating design and fabrication aspects, and a proven measurement method for tissue contraction will be shown. The drawbacks of such a method highlighted the need to look for an alternative approach: the solution was found in the integration of a capacitive displacement sensor in the platform substrate. The design and the fabrication process of this sensor will be reviewed, and the results of previously conducted simulations will be provided to serve as requirements for the readout that will be investigated by this thesis. Finally, as the first step of this thesis, fabricated sensors will be visually inspected and measured using microscopy, to verify the quality of the microfabrication process.

2.1. The EHT Platform at TU Delft

The platform developed by M. Dostanic at TU Delft [7] is a downscaled version of the Heart Dyno system [10]. The reason for downscaling is to make it compatible with a wafer-level microfabrication process, and to reduce the number of cells used for culturing. The study aims to precisely assess the contractile properties of the tissue that is cultured in the platform. To do that, a platform suitable for cell culturing was designed. A cleanroom-compatible microfabrication process was then developed to manufacture the platform, and mechanical characterization of the platform was performed to obtain a precise force-displacement curve. After cell culture, optical displacement measurements were performed on the structure, which allowed accurate measurements of the contractile force exerted by cardiac cells [7].

2.1.1 Design

The platform, microfabricated using PDMS, consists of an elliptic microwell fabricated around two elastic micropillars (Figure 1.1). The well confines a defined volume for the cell culture, while the pillars are used as anchors for the developed tissue. The general idea is that the tissue, after culture, spontaneously develops around the two micropillars with a certain thickness and height from the substrate, which were estimated in the study. This tissue spontaneously starts to contract, applying a force to the pillars in correspondence with its anchoring points. This force, as shown in Figure 2.1, makes the pillars bend, one towards each other, causing a displacement in the pillar tip (denoted with δ) and also a small deformation in the substrate.

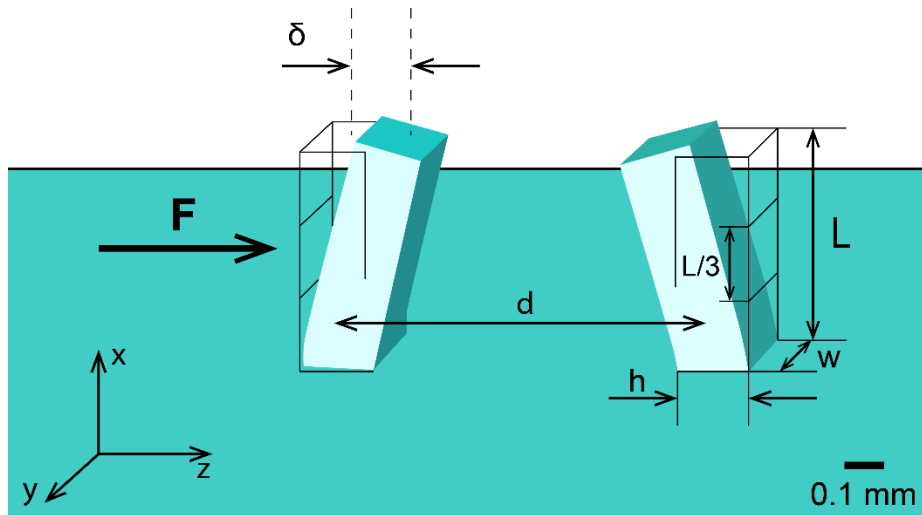


Figure 2.1: Working principle of EHT platform (Derived from [7]).

Dimensions of the platform as denoted in Figure 2.1 are:

- Micropillar width w : $478\mu\text{m}$
- Micropillar height h : $191\mu\text{m}$
- Micropillar length L : $700\mu\text{m}$
- Distance between the micropillars d : $970\mu\text{m}$

Thanks to the downscaling of the dimensions of the platform, it was possible to develop a cleanroom-compatible microfabrication process.

2.1.2 Microfabrication

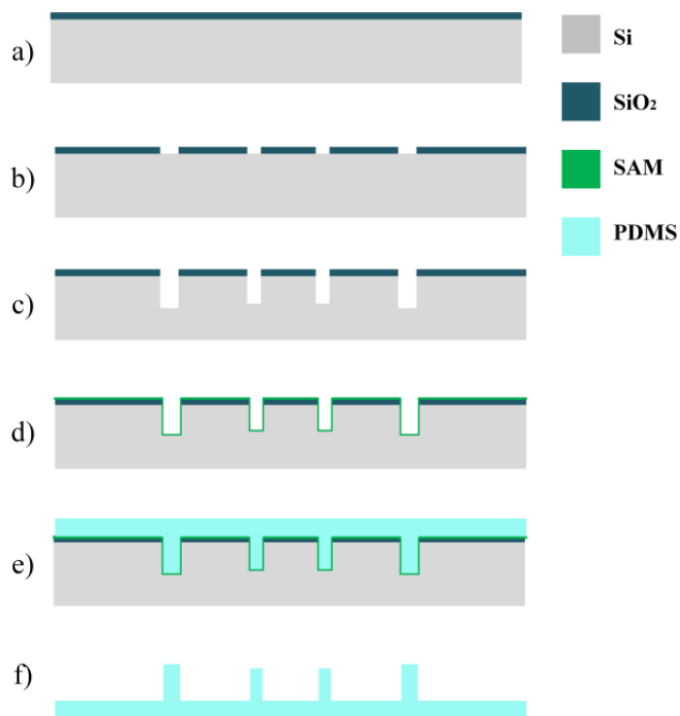


Figure 2.2: Microfabrication steps for the EHT platform (Derived from [7]).

The process for microfabrication of the platform using cleanroom-compatible micromachining and molding techniques can be seen in Figure 2.2.

A Silicon wafer was patterned and used as a mold for platform fabrication. The first step was to oxidize the wafer (a), to use SiO_2 as a hard mask. Openings were patterned on this oxide layer to define the desired shape for pillars and wells (b). The third passage was to perform Deep Reactive Ion Etching (DRIE) on the wafer to etch high aspect-ratio holes (c), to be used as a mold. The surface of the mold was then spin-coated with an anti-adhesion Self-Assembled Monolayer (SAM) to facilitate the final removal of the platform (d). Then PDMS was spin-coated on the wafer to fill the patterned holes and to create a thin uniform top layer of about $300\mu\text{m}$ (e). Finally, after curing, the PDMS structure was demolded and manually cut (f).

2.1.3 Measurements of pillar displacement

As previously mentioned, it is possible to estimate the force applied to the pillars by simply quantifying the displacement of the pillars while knowing their mechanical properties (in particular their stiffness).

Precise characterization of the mechanical properties of the platform, and in detail of the pillars, was performed by nanoindentation using a FemtoTools Nanomechanical Testing System (FT-NMT03). This process aimed to characterize the stiffness of the structure and create a relation between the displacement of the pillars and a known force applied to them.

After characterization, EHT was cultured inside the microwell within an incubator environment and spontaneously developed and aligned around the two micropillars (Figure 2.3a). After 72 hours, the tissues were active and showed cyclic contraction, which caused a deflection in the elastic pillars making them bend one towards the other. Electrical stimulation was also applied to the tissue using platinum electrodes, to assess the response of the tissue to several types of stimulation.

The displacement of the top of the pillars was tracked with optical measurement: first, the displacement was translated in pixels thanks to imaging algorithms, then this displacement was translated from pixel to micrometers. Knowing the displacement of the pillars, the application point of the force, and the displacement-force relation, it was possible to accurately assess the contractile force generated by the tissue. The results of this approach are shown in Figure 2.3b: the plot shows the change in the force applied by the tissue as a function of time. Intuitively, every peak indicates a contraction in the tissue.

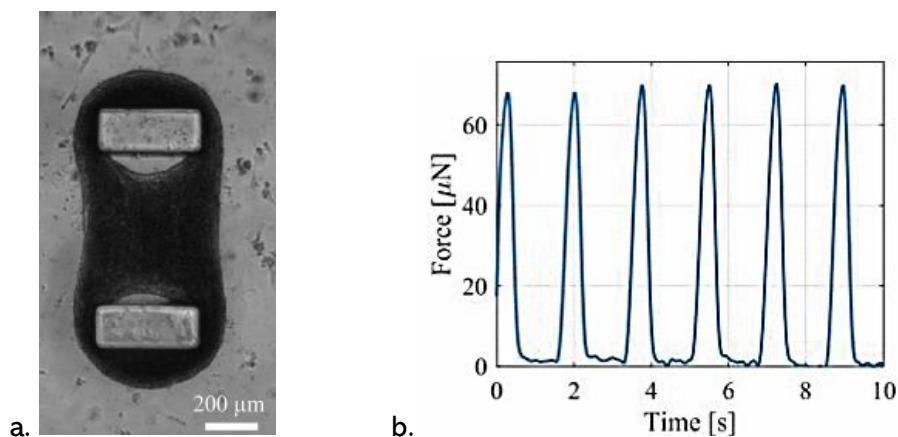


Figure 2.3: Top view of cardiac tissue successfully formed around pillars (Derived from [7]) (a), and contraction force of cardiac tissue derived using optical tracking (Derived from [7]) (b).

Optical displacement tracking is generally used for biological measurements due to its biocompatibility, and is still the main sensing technique highlighted in the literature in relation to OoC studies. Despite this, the trend is now shifting towards the integration of optical sensing and electrical sensing, because of the problems related to optical measurements. In particular, this approach requires bulky instrumentations that need to be placed around the sample, resulting in a system that is not easily portable. Moreover, displacement tracking requires the development of complicated imaging algorithms. Since these algorithms are based on pattern recognition, they might also prove unreliable when the surface they need to track is not smooth, clear, or defined. To overcome these problems an alternative to optical displacement sensing is needed, and electric motion tracking was investigated through the design and development of a sensor integrated into the platform.

2.2. Integration of capacitive displacement sensors

The investigation, design, and development of a sensor to be integrated into the platform was conducted during a Master Thesis project by Mahdiah Shojaei Baghini in 2020 [9]. Precise mechanical simulations of the platform were performed using COMSOL to highlight its behavior and identify techniques to sense the displacement induced by the tissue contraction. One of the most important results of these investigations is that the deflection of the pillar also causes a small, but not negligible, deformation in the substrate, which is made of the same elastic material as the pillars. The result of a simulation showing this substrate deformation can be seen in Figure 2.4.

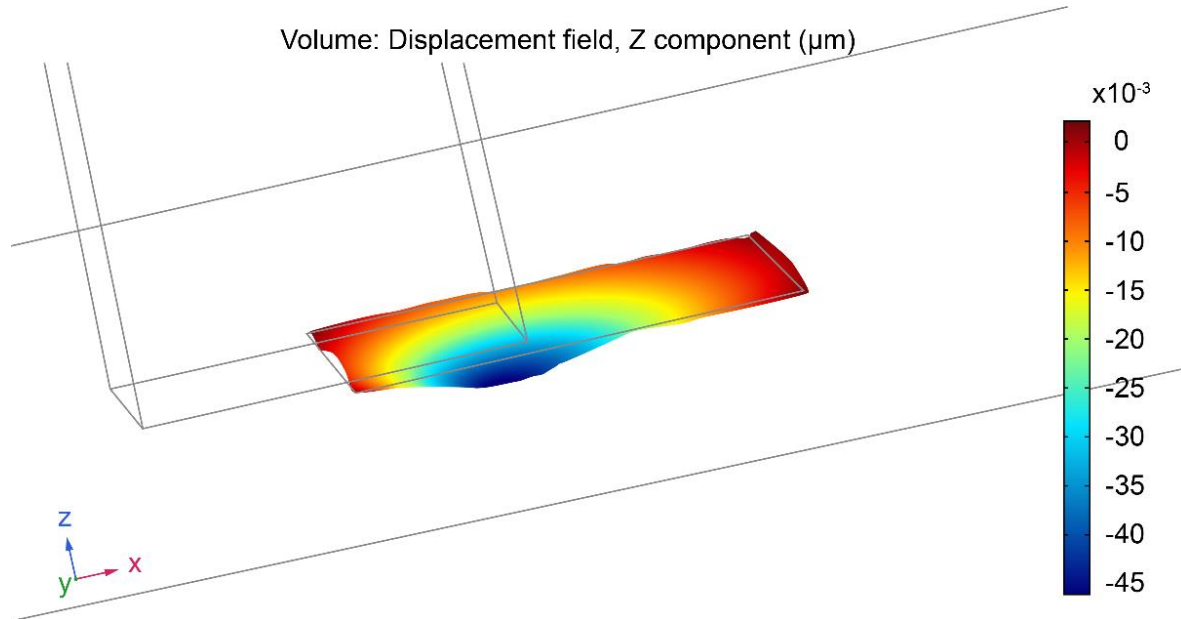


Figure 2.4: COMSOL simulation of substrate deformation as an effect of pillar displacement (Derived from [9]).

Multiple sensing techniques that can exploit this phenomenon, such as piezoresistive, piezoelectric, and capacitive, have been analyzed to identify a solution that allows the integration of the sensor into the substrate of the platform. A multiphysics study of the identified solutions was performed, highlighting the higher responsivity offered by the capacitive solution.

2.2.1 Design

Because of this higher responsivity compared to other sensors, capacitive sensors were chosen for design and development. The small depth at which deformation of the substrate happens led to the choice of co-planar capacitive sensors. Those sensors, according to waveguide theory, exploit the mutual capacitance that is created between two conductive lines, generated by the fringe effect of the electric field, as can be seen in Figure 2.5a.

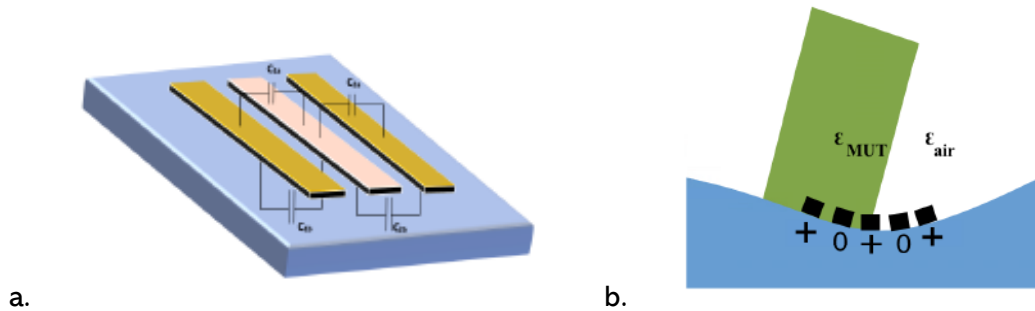


Figure 2.5: Co-planar waveguide capacitor (Derived from [9]) (a.), and cross-section of deformation and working principle of the substrate with integrated sensor (Derived from [9]) (b.).

This principle was used to design the sensors, in which two parallel aluminum lines were twisted one around each other in a spiral fashion, as was shown in Figure 1.2.

Aluminum was chosen as a material for sensor fabrication due to its flexibility, to avoid the use of stress buffering layers, since the presence of the sensor in the substrate shall not interfere with the mechanical properties and behavior of the platform.

The positioning of the sensors also played a significant role in the research for maximum responsivity: studies led to the positioning of the center of each sensor in the substrate right below the pillar, aligned with the long side of its base (where simulations showed higher displacement).

The movement of the pillar, and subsequent deformation of the substrate with the integrated sensor, causes warping in the fringe electric field lines of the sensor, leading to a capacitance change. A cross-section of the device illustrating the working principle can be seen in Figure 2.5.b.

Since the behavior of the substrate is equal and opposite with respect to the middle line of the pillar, two sensors could be integrated below each pillar, for them to behave differentially. In a whole platform, therefore, four spiral sensors are placed, two per pillar, as can be seen in Figure 2.6.

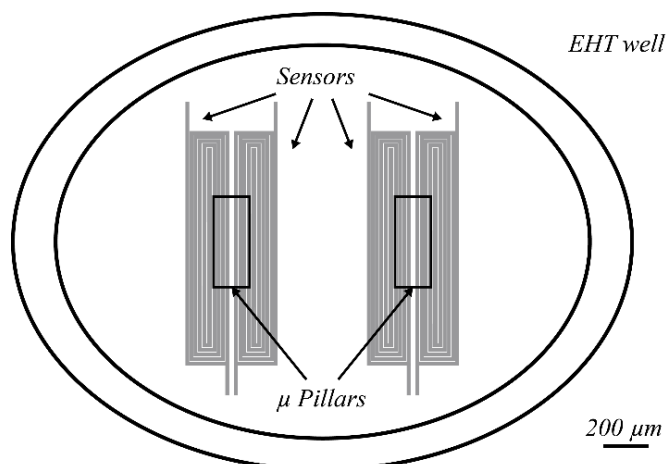


Figure 2.6: Layout and location of spiral capacitive sensors with respect to pillars and well (Derived from [9]).

The geometrical design of the sensors also proved to influence their behavior. The dimensions of the spiral were fixed for the spiral to cover the whole area where substrate deformation happens. The design space focused therefore on two variables: the trace width (w) and the gap (g) between the traces. A parameter called Metallization Ratio (MR) was defined as $MR = \frac{w}{w+g}$ to evaluate both w and g at the same time. It was shown that, as the metallization ratio increases, the responsivity of the sensors decreases.

Four distinct types of sensors were designed with different values for w and g , as can be seen in Table 2.1 and Figure 2.7.

Table 2.1: Geometrical properties of the different sensor types (Derived from [9]).

	Sensor Type A	Sensor Type B	Sensor Type C	Sensor Type D	Unit
Gap (g)	5	10	5	10	μm
Trace width (w)	20	10	5	40	μm
Metallization ratio (MR)	0.8	0.5	0.5	0.8	

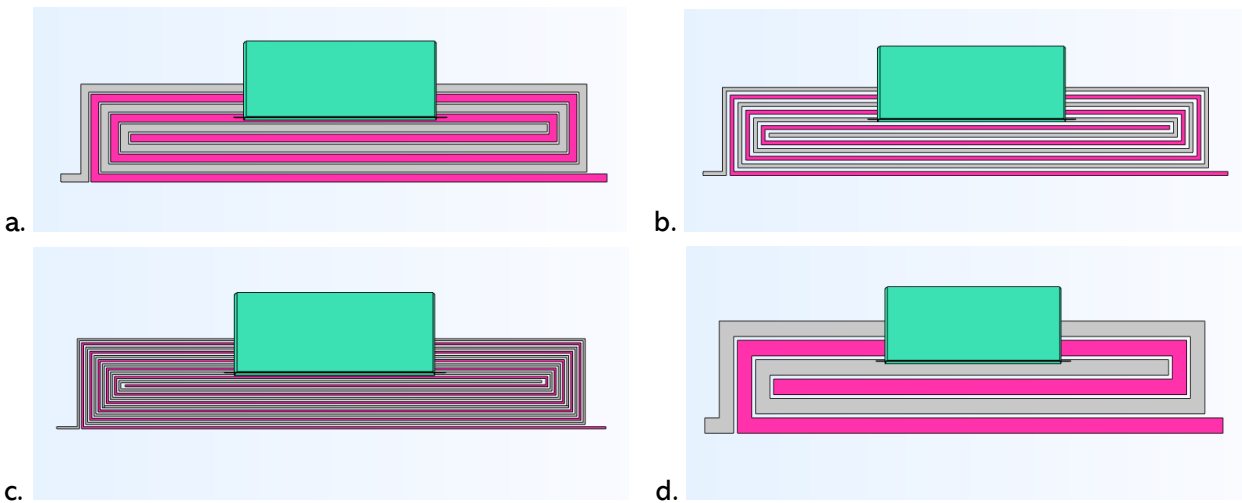


Figure 2.7: Layout of sensor types (Derived from [9]).

2.2.2 Microfabrication

These small features and structures required the use of microfabrication processes for manufacturing. Cleanroom processing was therefore used for the integration of the sensors in the platform. A modification of the process shown in Section 2.1.2 was developed, adding extra steps for the microfabrication of aluminum sensors. First, a quartz mask (Figure 2.8) was designed for aluminum patterning.

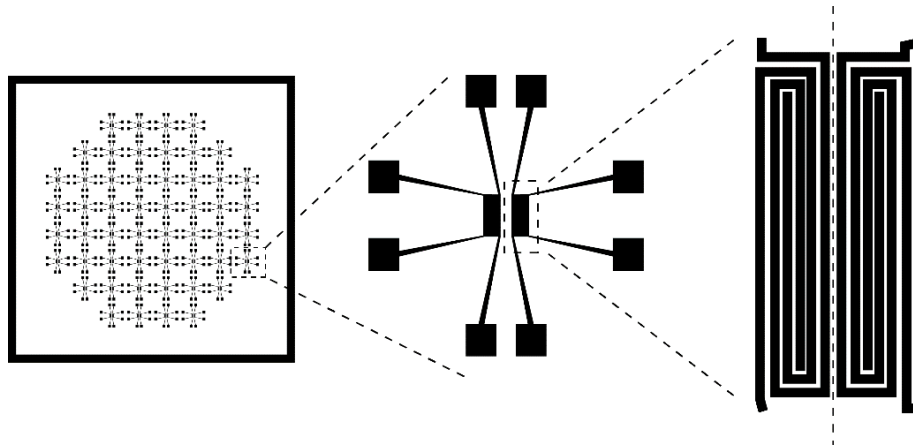


Figure 2.8: Quartz mask design (Derived from [9]).

The process of Figure 2.9 was developed for the fabrication of aluminum sensors on top of a layer of PDMS. This process provides, as a result, a thin layer of PDMS with a top layer of aluminum, which is patterned to create the sensors. The aluminum patterning of the whole wafer is performed during the same fabrication step, which explains why the whole aluminum structures (including the contact pads of the sensors) are patterned on top of a PDMS flexible substrate. This aspect will be evaluated in detail in Chapter 5, especially in relation to its criticalities.

A different process using Polyimide (PI) as a stress buffer and insulation layer between the PDMS substrate and the aluminum traces was previously developed for similar applications, and is reported in Appendix K. It was discarded in relation to this application because it would have altered the mechanical properties of the structure.

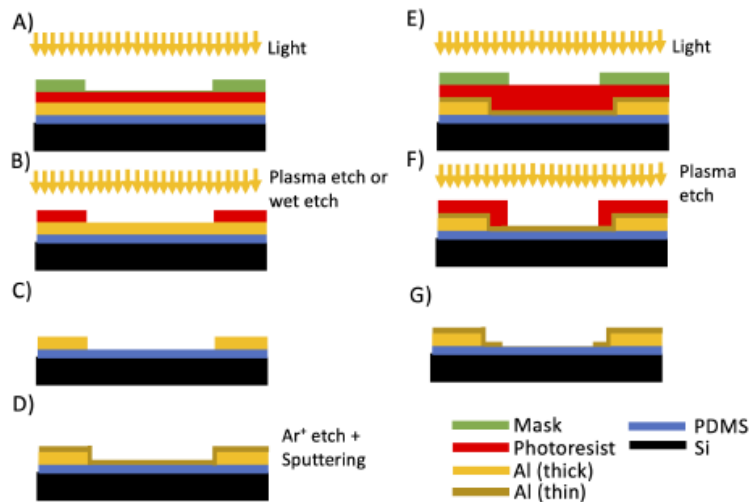


Figure 2.9: Microfabrication steps for spiral sensors on top of PDMS (Derived from [9]).

After the fabrication, therefore, there will be no EHT platforms (and consequentially no pillars) on top of the sensors. It is possible to produce EHT platforms with pillars and wells and with a thin substrate using a process like the one illustrated in Section 2.1.2, and to manually place the platforms on top of the devices obtained using the process of Figure 2.9. A thin layer of uncured PDMS that will function as a glue can be used for this process. The passage, as can be seen in Figures 2.10a and 2.10b, was investigated and proved to be effective despite the need for accurate manual alignment.

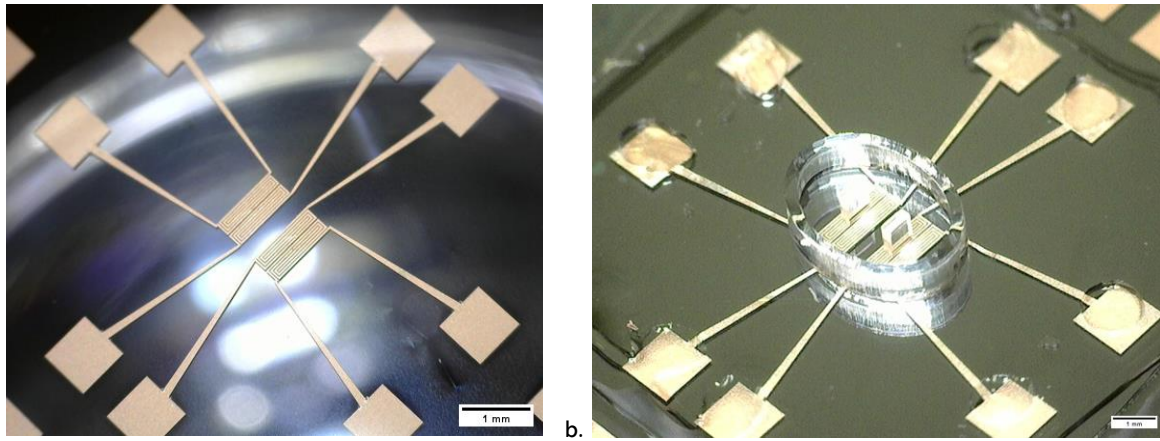


Figure 2.10: Fabricated sensors on PDMS layer before (a.) and after (b.) gluing of PDMS layer, pillars and well on top.

2.2.3 Simulations

Precise multiphysics simulations have been performed on all the designed sensors, together with calculations deriving from co-planar waveguide theory. The simulations focus on two values: the capacitance of the sensors when no force is applied to the pillar (base capacitance, related to static behavior) and the responsivity of the sensors, which is the relation between the force applied to the system and the change in capacitance of the sensors. Results obtained are listed in Table 2.2 and show good agreement between simulation and calculations derived from theory.

Table 2.2: Simulated and calculated values for static and dynamic properties of different designed sensors.

	Sensor Type A	Sensor Type B	Sensor Type C	Sensor Type D	Unit
Base capacitance (CPW theory)	0.55092	0.41017	0.73418	0.34865	pF
Base capacitance (COMSOL)	0.59279	0.43321	0.77640	0.36013	pF
Responsivity (COMSOL)	1.51	3.1	4.864	0.86	pF/N
Base capacitance (CPW theory) without top PDMS layer	0.374	0.279	0.497	0.231	pF

In Dostanic's study, the maximum force applied on the pillars by the cultured tissue was measured to be around 70 μN , but taking into account the downscaling of the platform and assuming that cells behavior may vary from batch to batch, a worst-case estimation lowers the force applied by the tissue down to 10 μN .

Assuming that the change in capacitance is linear, and that therefore the expected change in capacitance can be obtained by simply multiplying the expected applied force by the simulated responsivity of the sensors, the worst-case estimation for the capacitance change is around 10aF. Reading out such a small capacitance change is a challenging task, and the investigation of readout strategies is one of the aims of this Master Thesis. A literature review of possible suitable circuit architectures will be presented in the next chapter.

Base capacitance without top PDMS layer. As a last remark concerning the base capacitance values just shown, it is important to notice that these values are related to the final fabrication process in

which the sensor is integrated between two layers of PDMS. As explained in the previous section, a different process was developed for the fabrication of sensors on top of PDMS without a second covering layer and without pillars on top of the sensors. Because of the symmetrical behavior of the electric field lines, and because of the difference in the dielectric constant of PDMS (2.75) [9] and of air (1), the expectation is that the sensors developed with this latter process will provide lower base capacitances compared to the values reported in Table 2.2. For this verification, calculations have been performed again: assuming that half of the field lines will be located in PDMS and half in air, the intuitive expectation is that the sensors will have a base capacitance around 0.68 times the one reported in the table, that was obtained when all the field lines are located inside the PDMS medium. This ratio comes from

$$\sum (\%_{field_lines} \times \frac{\epsilon_{new_material}}{\epsilon_{old_material}}) = 0.5 \times \frac{2.75}{2.75} + 0.5 \times \frac{1}{2.75} = 0.68 \quad (2.1)$$

These rough calculations have been confirmed by more precise calculations obtained according to [11], which provided expected base capacitance values reported in the last row of Table 2.2.

Since the placement of the PDMS top layer is one of the latest steps in the assembly procedure of the sensors, most of the measurements presented in Chapter 7 need to be compared to these latter values. The values reported in the first rows of the table will only be valid in relation to some of the final measurements, when a second PDMS layer with well and pillars is placed on top of the sensors to allow measurement and tests of the dynamic behavior of the sensors.

2.3. Visual inspection and measurements

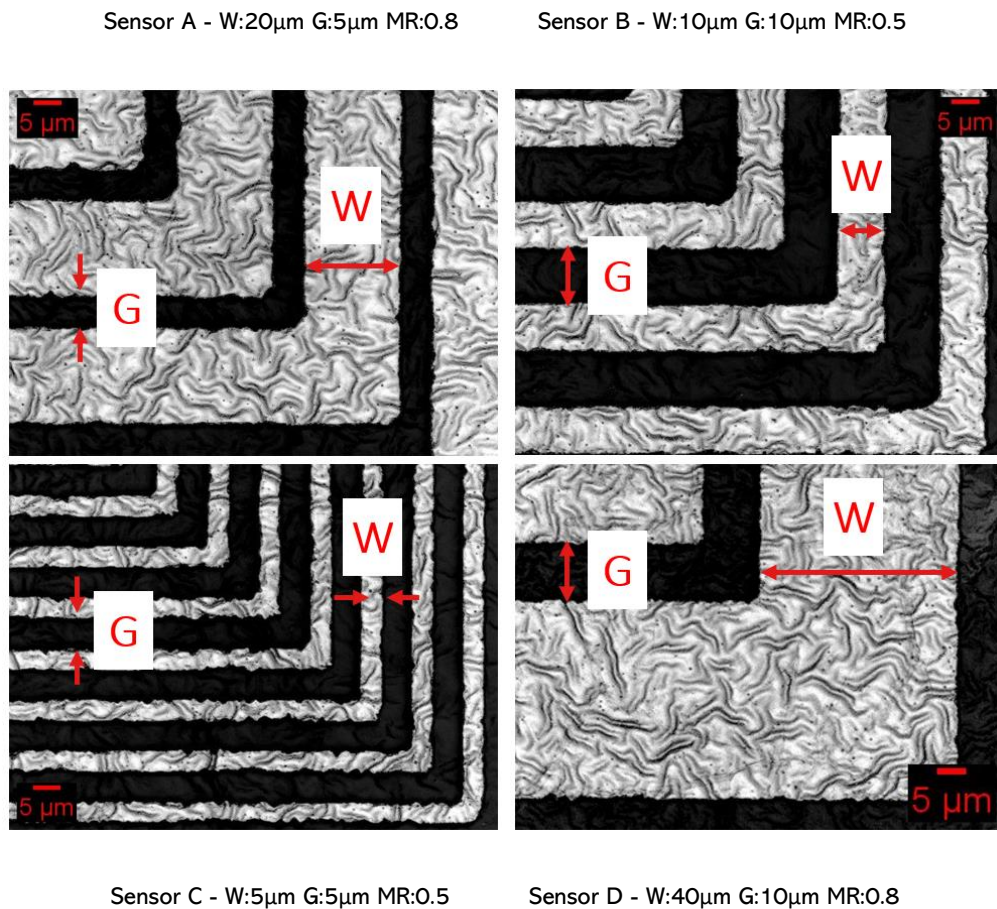


Figure 2.11: Sensor inspection for each type.

Before diving into the challenges related to the readout, an optical inspection of the quality of the fabricated devices was performed to identify possible criticalities. This inspection was performed on the wafer using the laser microscope Keyence VK-X250 available in EKL Cleanroom at TU Delft. All the sensors on the wafer were inspected to identify defects, and measurements of trace width and gap were performed for each sensor type, providing the results shown in Figure 2.11. All the measurements proved to be in agreement with the expected results, with only smaller deviations from the expected width and gap between the traces, confirming the quality of the process and the suitability of the etching. The only unexpected result was related to wrinkles that appeared on most of the sensors' aluminium surface, caused by the wrinkling of PDMS substrate originated by thermal-induced stress during the process [12], but these were proven to be non-critical and to only cause possible deviation in sensor behaviour of less than 10% [9].

Capacitive Readout

The specifications deriving from the sensors were presented at the end of last chapter, to allow to focus on the real aim of this thesis: the investigation, identification, and development of a high-precision and portable readout circuit. This circuit will be used to read out the sensors and therefore to succeed in the project goal, which is the characterization of the sensor behaviour (possibly verifying the simulations and calculations performed in the previous chapter). To be successful in this challenging task, a deep review of capacitive readout was performed. This review was performed as a preparatory phase for this Master Thesis and was used to identify suitable readout techniques: the results of this study are shown in this chapter.

3.1. Introduction to capacitive sensing

Capacitive sensors are devices that can be used in different applications, and that allow the measurement of several physical effects, such as displacement, chemical concentration, and acceleration [13]. These types of sensors are generally constituted by variable capacitors, whose value might be affected by multiple phenomena such as movements, deformations, and chemical changes [14]. The capacitance C of a parallel plate capacitor is given by

$$C = \varepsilon_0 \varepsilon_r \frac{A}{d} \quad (3.1)$$

where ε_0 is a constant associated with the permittivity of vacuum, and the other three parameters are variables depending on the geometry and on the material of which the capacitor is made. Since all three parameters might vary, three possible types of sensors can be identified [15]: D-type capacitive sensors, in which the variable parameter is the distance d between the two capacitor plates; A-type capacitors, in which the change in capacitance is due to changes in the effective area of the electrodes A ; and ε -type capacitors in which the measurand modifies the specific dielectric properties ε_r . Capacitive sensors can be implemented using parallel plate capacitors, but also using co-planar structures [16], which can be seen as an evolution of parallel-plate capacitors, and that are the sensors used for the application related to this project (Figure 3.1).

An alternative way to categorize capacitive sensors is to consider floating and grounded capacitive sensors. Floating sensors have one terminal driven by an excitation signal while charge or current is measured at the other terminal, while grounded sensors have one of the two terminals connected to ground. Floating capacitors are generally preferred in cases in which high accuracy is required, because they can be measured with interface circuits that are intrinsically immune to parasitic capacitances to ground, and because grounded sensors present a trade-off between accuracy and

stability [17]. For this reason, the sensors for the final application of this thesis will be used in a floating configuration.

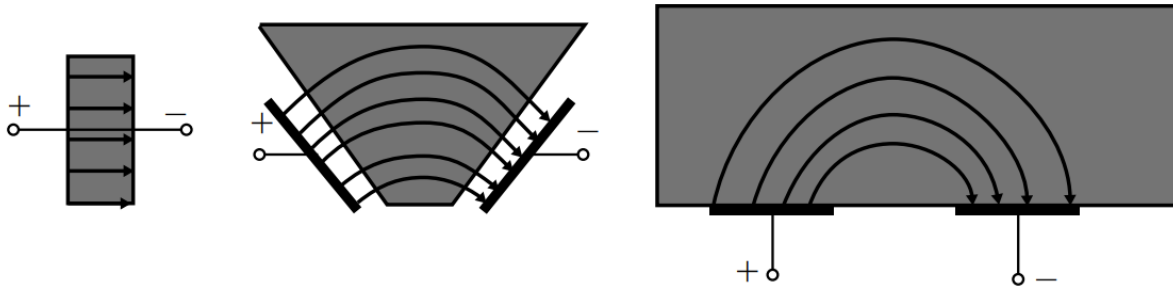


Figure 3.1: Transition from parallel-plate capacitors to co-planar capacitors. (Derived from [16]).

Capacitive sensors are widely used in multiple applications in the last decades for their specific advantages [18]. The main ones relate to the fact that they are simple to manufacture and therefore cheap to produce, they can provide high resolution, they are suitable for contactless sensing, they can have a very low power consumption and very low temperature dependency [19, 20]. Despite these advantages, which make capacitive sensors convenient for many applications, these types of sensors also suffer from drawbacks. These problems are mainly related to high sensitivity to disturbances coming from physical effects, such as Electro Magnetic Interference (EMI) or the disturbances created by the presence of other conductors in the sensing environment [21, 22]. The challenges arising from these physical problems require careful control and protection of the measurement environment, which is generally related to the shielding of the system. In certain situations, shielding is not sufficient to obtain a proper resolution. In those cases, differential configuration of the sensors and of the readout can help to increase resolution [23, 24]. When differential readout does still not provide the needed specifications in terms of resolution, specific circuit techniques can be used. Some of these techniques will be highlighted in the next section, and allow suppression of noise and interferences and control of parasitic capacitance that derive from the interconnects of the system.

3.2. Specific techniques for accurate readout

Multiple techniques to suppress undesired disturbances of the measured signal were developed in the last decades and can be found in the literature. The most effective and most widely used are chopping, four-point measurement, and autocalibration.

3.2.1 Chopping

Chopping is a circuit technique that dynamically attempts to cancel the effect of system nonidealities [25]. It reduces the effect of offsets, flicker noise, and in general of all low-frequency interferences [26]. The schematic of a circuit implementing chopping, and its behaviour in the time domain and in the frequency domain is shown in Figure 3.2.

The input low-frequency signal V_{in} is upmodulated by the effect of a chopper, which multiplies the signal by a square wave signal of amplitude ± 1 and frequency f_{chop} . The signal is therefore

converted in a square wave of amplitude $\pm V_{in}$ and frequency f_{chop} . In the frequency domain, V_{in} is upmodulated to f_{chop} and to its multiple harmonics. The disturbance and noise caused by the amplifier can be modelled as a low DC signal located at the input of the amplifier (V_{os}). Both this DC signal and the chopped signal are amplified by the amplifier gain and are then passed through a second chopper with the same frequency and phase as the first one. The effect of this second chopper is to demodulate the amplified input signal back to DC, and to modulate the disturbance at frequencies of f_{chop} or higher. As a final stage, in general, a Low Pass Filter (LPF) is implemented to filter out the upmodulated disturbance.

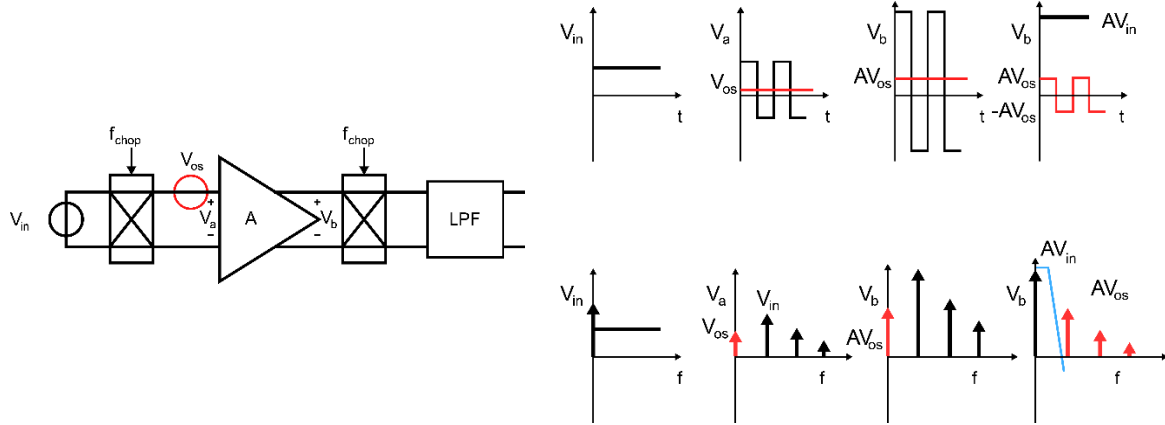


Figure 3.2: Chopping principle and effect in time domain and frequency domain (Derived from [27]).

This is the working principle of standard chopping, in which the chopper multiplies the signals for a square wave in a +1 -1 +1 -1 fashion. Advanced chopping techniques have been investigated, and +1 -1 -1 +1 multipliers were proved to reduce the disturbances even further, because of the subtraction of residual errors [28].

3.2.2 Autocalibration

Autocalibration of offset and gain, also known as three-signal technique, is a technique that can be used to reduce the effect of low-frequency noise and to limit the negative effects coming from systematic errors [29].

This technique is used in relation to linear systems when parameters are not precisely defined. Assuming a Time-Capacitance linear relation of the type $T = aC + b$, autocalibration takes advantage of the consecutive measurement of two known reference signals (related to reference capacitors C_{ref1} and C_{ref2}). These two extra measurements allow obtaining the unknown signal C_x independently from the parameters a and b , which are affected by drifts and variations. With post-processing techniques, the uncertainty of these parameters can be eliminated in the calculations to obtain the value of C_x .

$$C_x = \left(\frac{T_x - T_{ref1}}{T_{ref2} - T_{ref1}} \right) (C_{ref2} - C_{ref1}) + C_{ref1} \quad (3.2)$$

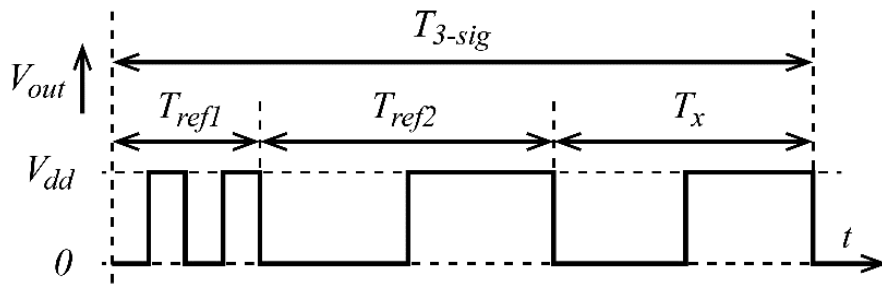


Figure 3.3: Period-modulated three signal technique related to capacitance measurement (Derived from [17]).

In Figure 3.3, an example of a three-signal approach is shown, in which the period associated with each signal is linearly dependent on the capacitance connected to the readout (respectively C_{ref1} , C_{ref2} , and C_x).

This approach requires a microcontroller [30] and is expensive in terms of measurement time and energy consumption, but increases the accuracy of the readout [31].

3.2.3 Four-point measurement

Another technique that is often used is four-point measurement, or two-port measurement. This technique allows for addressing the problems resulting from the accuracy decrease caused by the parasitic behaviour of interconnects [32]. This measuring principle relies on the application of a voltage V at the input of the sensing capacitance C_x (Figure 3.4), and on the measurement of the short circuit current i at its output. In this way, it is possible to have a sensing signal that is only dependent on the sensing capacitance and not on the parasitic capacitance value, since the current through $Cp2$ is negligible, and the current through $Cp1$ does not affect the measurement. This technique requires low impedance both at the input and at the output, and allows for the elimination of the contribution of the parasitic capacitance to the ground.

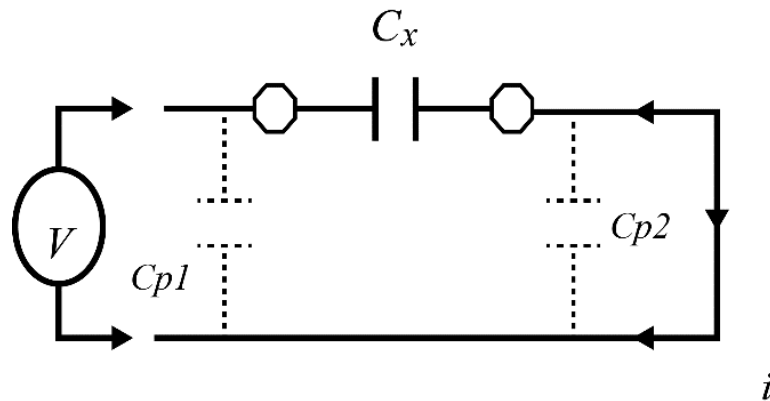


Figure 3.4: Four-point measurement principle for capacitive measurements (Derived from [30]).

3.3. Architectures for capacitive readout

The explained circuit techniques can be used to increase the performances of certain architectures that are designed especially for capacitive readout [33]. In the literature, a wide variety of electronic circuitry can be found, with several types of output signals to which input capacitive signals can be converted. The five main strategies translate the input capacitance variation into an output signal in

the voltage domain (C2V), in the current domain (C2I), in the time domain (C2T), in the frequency domain (C2F), or directly in the digital domain (C2D) [34]. For each of these conversion types, different circuitry can be found and will be highlighted in the next subsections. As will be explained in Section 4.4, noise is the main factor limiting the resolution of a readout circuit [35], and therefore noise specifications of each structure need to be investigated [36]. Where possible, noise figures relative to the Signal to Noise Ratio (SNR) of each structure will be derived, and improvement points will be highlighted.

3.3.1 Capacitance to Current

Capacitance-to-Current converters translate the input capacitance change to an output current using the principle illustrated in Figure 3.5. A constant current I_a flows through a common node where both a sensing capacitance C_x and a reference capacitor C_{ref} are connected. The value of C_{ref} is selected to be equal to the value of the capacitive sensors when it is not stimulated. The second electrode of these capacitances serves as input for a current differencing block. The measurement is done in two phases: a discharge in which switches S_1 and S_2 are closed having I_{out} equal to zero, and a measurement phase in which

$$I_{out} = I_a \frac{C_x - C_{ref}}{C_x + C_{ref} + C_{stray}} = I_a \frac{\Delta C}{C_x + C_{ref} + C_{stray}} \quad (3.3)$$

where ΔC denotes the change in the sensing capacitance and C_{stray} is the parasitic capacitance to ground.

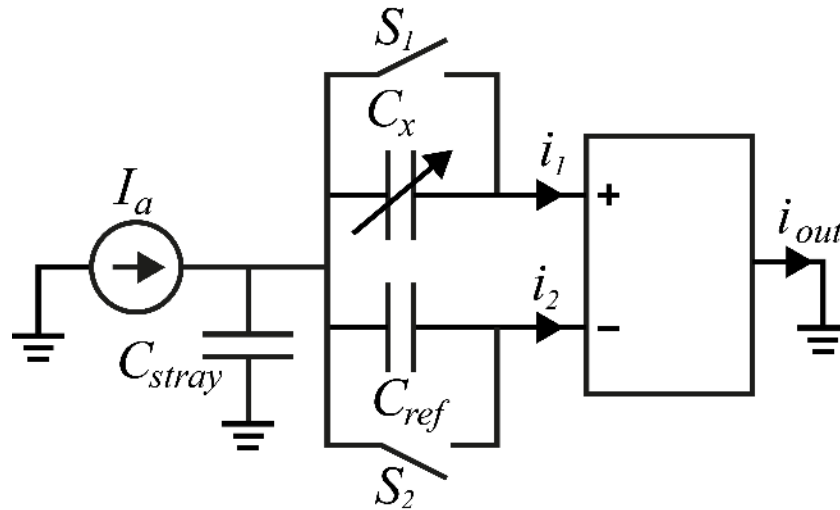


Figure 3.5: Capacitance to current circuit (Derived from [34]).

The noise figure for this circuit was derived in [34] as

$$SNR = \frac{\left(\frac{i_{out}}{\sqrt{2}}\right)^2}{i_{noise,rms}^2} \quad (3.4)$$

where i_{noise} depends on the current differencing block and I_a can be increased (up to certain levels) to reduce the SNR.

This circuit implementation is simple and provides fast measurements and low power consumption, but has the drawback to be extremely sensitive to parasitic capacitances (C_{stray}).

3.3.2 Capacitance to Frequency

Capacitance-to-Frequency topology is often implemented using structures called ring oscillators [37]. Those are implemented with N inverters in series, where N is an odd number (Figure 3.6). The sensing capacitor is the load of one of these inverting stages. In [38] the output period is derived as per Eq. 3.5, and in [39] SNR is derived as per Eq. 3.6.

$$T_{out} = \frac{2V_{DD}}{I_{avg}} (C_x + (N-1)C_{load}) \quad (3.5)$$

$$SNR = \frac{(\Delta C_x V_{DD})^2}{3.67kT (C_x + (N-1)C_{load})} \quad (3.6)$$

Accordingly, SNR can be quadratically increased by increasing V_{DD} , or by reducing the capacitance of C_x and C_{load} .

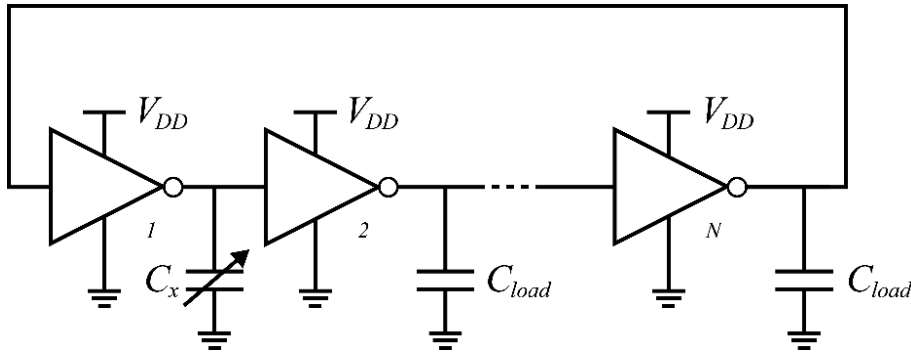


Figure 3.6: Capacitance to frequency circuit (Derived from [34]).

The advantages of these structures are the low power consumption and the easy translation to digital [40], while the sensitivity to the environment configures the main drawback.

3.3.3 Capacitance to Time

Capacitance-to-Time structures are also known as relaxation oscillators, and their working principle is shown in Figure 3.7. A reference current I_b charges the capacitive sensor C_x . A comparator checks when the voltage across the capacitor is higher than a reference V_{ref} , and in that case its output lowers the capacitor voltage back to zero through the switch M_s . The output, therefore, stays high for a time that is proportional to the capacitance charge and that is expressed by

$$T_{out} = \frac{C_x V_{ref}}{I_b} + \tau_d \quad (3.7)$$

with τ_d indicating the delay of the comparator.

The noise figure was derived as

$$SNR = \frac{(\Delta C_x V_{ref})^2}{I_b (\sigma_{comp}^2 + \sigma_{V_{ref}}^2)} \quad (3.8)$$

SNR can therefore be increased by increasing the reference voltage, or by reducing the reference current.

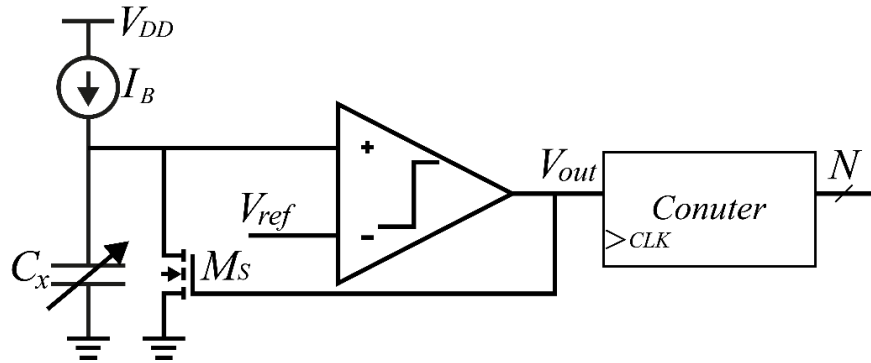


Figure 3.7: Capacitance to time circuit (Derived from [34]).

These structures produce period-modulated signals at the output that can be easily converted to a digital signal using a counter. They do not provide the best performance in terms of resolution, but they provide extremely low power consumption and simplicity, therefore they are often used as a second stage after capacitive to voltage structures (as will be seen in the next subsection) [33].

The main drawbacks of this type of structures are the challenges related to the design of an accurate comparator, which is needed for the proper functioning of the readout.

3.3.4 Capacitance to Voltage

Multiple structures allow the translation of capacitance change into an analog voltage [41]. These solutions are among the most used because the output voltage level can be digitized easily with a second stage. Three main solutions will be analysed, each configurable both as differential and as single-ended.

Charge-sensitive amplifiers (CSA) exploit a principle that is similar to the one used by simple capacitive dividers, using an architecture like the one shown in Figure 3.8.

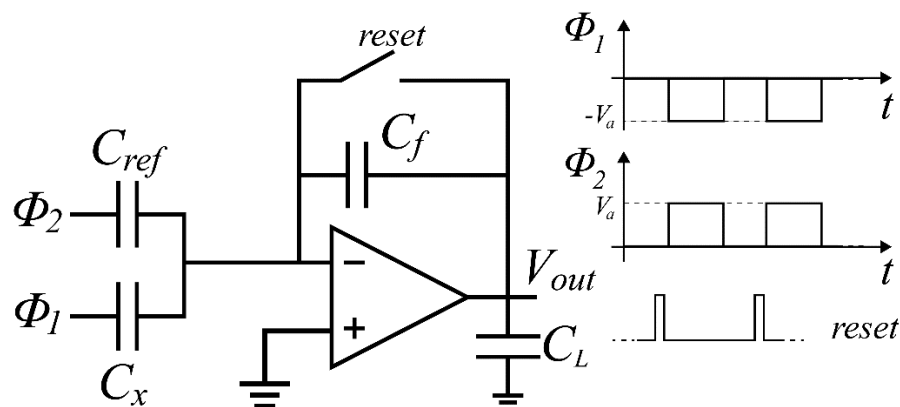


Figure 3.8: Capacitance to voltage CSA circuit (Derived from [34]).

Two opposite voltage pulses Φ_1 and Φ_2 are applied respectively to the sensing capacitor C_x and to a reference capacitor C_{ref} . Via the charge-sensitive amplifier, a charge proportional to $C_x - C_{ref}$ and so proportional to the change in capacitance ΔC of the sensing element is integrated into the feedback capacitor [34]. The output voltage V_{out} will therefore be

$$V_{out} = \frac{\Delta C}{C_f} V_a \quad (3.9)$$

SNR of this structure when the amplifier is a single-stage Operational Transconductance Amplifier (OTA) was derived in [42] and is

$$SNR = \frac{\beta(C_L + (1-\beta)C_f)}{4kTC_f(C_L + (1-\beta + \alpha\gamma)C_f)} (\Delta C_x V_a)^2 \quad (3.10)$$

Where α is the excess noise factor of the amplifier, the feedback factor $\beta \approx C_f / (C_x + C_{ref} + C_f)$ and γ is the noise coefficient of the MOS transistor. As it is clear from the formula, actions can be taken to increase the SNR: the use of a higher excitation voltage V_a , of a smaller feedback capacitor C_f , or of a bigger load capacitor C_L . With this structure and these cares, high resolution can be obtained, even if research shows that this structure has high power consumption, generally because of the power-hungry digitizers that need to be used at the following stage, as in [43]. A simple and low-power solution is to use a circuit that provides period-modulated signals as a second stage [17] such as a relaxation oscillator, obtaining a structure similar to the one developed in [44, 45] and suggested by Shojaei Baghini for the readout of her sensors [9]. This period-modulated signal can then be digitized by a microcontroller using a counter.

Lock-In Detection (LID) is another capacitive-to-voltage structure, based on the principle of coherent detection. It is especially efficient in reducing the effect of parasitic capacitance and minimizing electrical noise [46]. Because of its excellent performance in terms of resolution, it is often used in applications where noise and signal levels are similar [47, 48]. The working principle of such structures is shown in Figure 3.9: a sinusoidal excitation signal of amplitude V_{AC} and frequency f_{AC} drives the sensing impedance Z_x . A transimpedance amplifier (TIA) converts the signal into a voltage that is then processed by a Lock-In Demodulator (LID), which multiplies the signal by the excitation and by its 90° shifted version to shift the signal from f_{AC} to DC and to separate its Real and Imaginary parts. Filters are then used to remove the higher harmonics of the signal. In [49] noise figure was extracted for this architecture providing

$$SNR \propto \frac{g_m (\Delta C_x V_{AC})^2}{4kT (C_x + C_{par})^2 ENBW} \quad (3.11)$$

where ENBW indicates the Equivalent Noise Bandwidth of the circuit, defined as the bandwidth of a brick wall filter that produces the same integrated noise power as the actual filter. SNR can be increased with a higher excitation amplitude V_{AC} , or by reducing the value of $C_x + C_{par}$. The virtual ground provided by the TIA helps to reduce the effect of C_{par} .

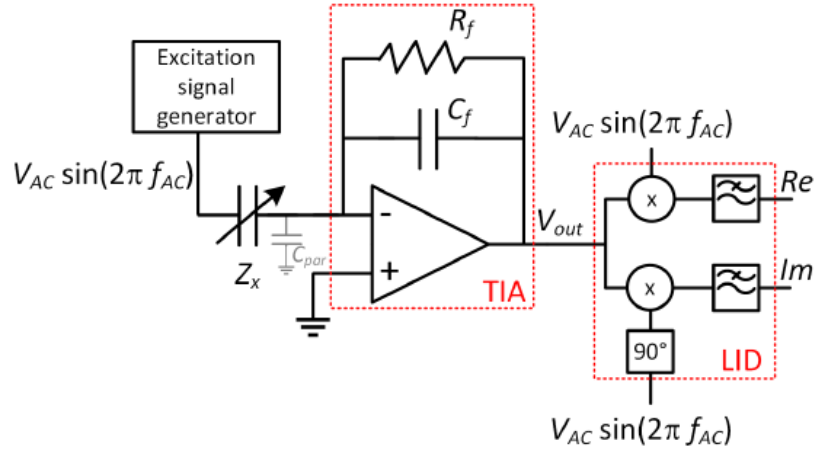


Figure 3.9: Capacitance to voltage LID circuit (Derived from [34]).

The main drawbacks of these extremely high-resolution structures are related to the challenges in the implementation of an accurate signal generator, which causes complex, expensive, and bulky designs, and the fact that these structures are affected by a resolution/measurement time trade-off [34].

Charge-Based Capacitance Measurement (CBCM) structures are based on the architecture of Figure 3.10.

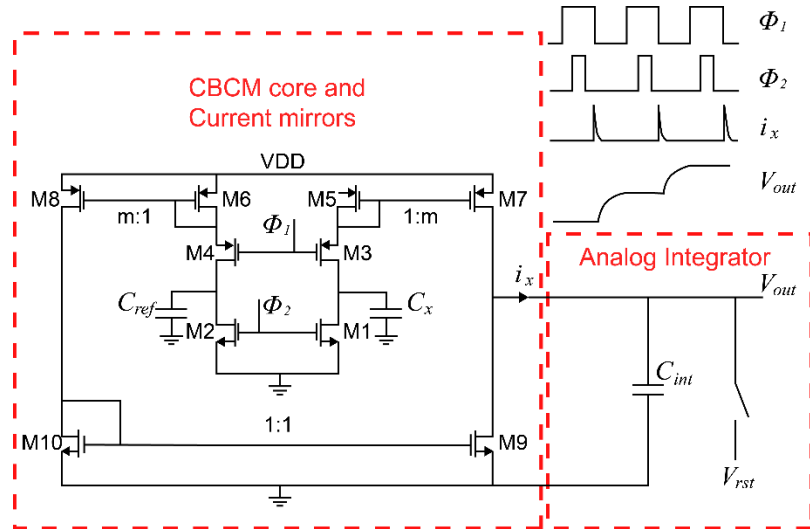


Figure 3.10: Capacitance to voltage CBCM circuit (Derived from [34]).

Transistors M1-M4 function as switches for driving the sensing and reference capacitors C_x and C_{ref} . The current mirror implemented by M5-M10 allows the subtraction of the currents flowing through the two capacitors, and this current is then directed through an analog integrator. The final output voltage across the integrating capacitor is

$$V_{out} \approx m(V_{DD} - V_{TH}) \frac{\Delta C_x}{C_{int}} \quad (3.12)$$

as derived in [34]. In the same study, the SNR value is calculated, providing

$$SNR \propto \frac{m^2 \Delta C_x^2 (V_{DD} - V_{TH})^2}{4kTC_{int}} \left(\frac{C_x}{C_{int}} \right) \quad (3.13)$$

SNR can be improved by increasing the current mirror gain m , the overdrive voltage $V_{DD} - V_{TH}$ or by reducing the value of the integrating capacitor. This architecture provides good resolution, but has the drawback typical of every symmetrical circuit design: it is limited by mismatches in the behaviour of the transistors and requires therefore careful compensation [34].

3.3.5 Capacitance to Digital

Capacitance-to-digital converters avoid the extra step required to translate each of the previously illustrated signal domains into the digital domain, and because of that, despite their complexity, they provide very low power consumption compared to the other analysed architectures [15]. The main circuits reviewed in relation to this type of readout, which are implemented in many integrated circuits for capacitive readout, are sigma-delta converters and SAR circuits.

Sigma-Delta (Σ - Δ) converters are converters based on the architecture shown in Figure 3.11. The working principle of the structure is based on the idea that the ratio between ones and zeros at node D is proportional to the ratio between the capacitance of the sensing element C_x and the capacitance of the reference element C_{ref} . Assuming that at $t=0$ the output of the integrator is negative, node D is at 0. During the clock cycle, C_x is charged to V_{ref} and the charge is then transferred to C_{int} increasing the integrator output value with a step of $\frac{C_x V_{ref}}{C_{int}}$. This process is repeated for multiple clock cycles until the integrator output becomes positive. In that case, D becomes 1, and from the first clock cycle after this moment the charge transferred to C_{int} is equal to $(C_x - C_{ref})V_{ref}$. Since these two amounts of charge transferred should compensate each other, in a long stream of zeros and ones, the number of ones is proportional to $\frac{C_x}{C_{ref}}$. This ratio is obtained using a decimation filter, which is the last stage of the structure [17].

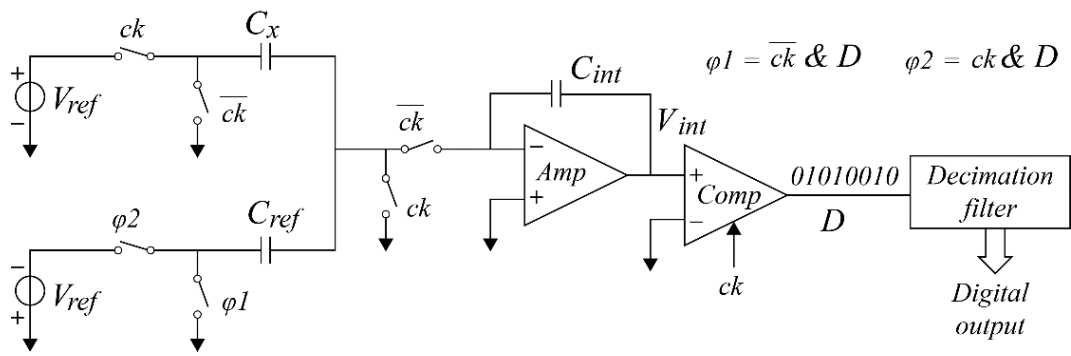


Figure 3.11: Capacitance to digital Σ - Δ circuit (Derived from [17]).

Despite the complexity of the structure, the resolution of these types of circuits is among the highest found in the literature, due to the oversampling ratio that lowers noise effects [50, 51].

Successive Approximation Register (SAR) structures are based on SAR logic blocks. Figure 3.12 shows a possible implementation. The working principle of this structure relies on two phases. In the precharge phase, Φ_1 is high, the integrator acts as a buffer setting V_x equal to V_{ref} and C_x has a

charge of $Q = C_x V_{ref}$ stored in it. In the evaluation phase, Φ_1 is low while Φ_2 is high, providing 0V across the sensing capacitor. The charge, therefore, redistributes between C_{ref} (implemented using a Programmable Capacitor Array, PCA) and C_F , providing a total charge of $Q = C_{ref} V_{ref} + (V_{ref} - V_0) C_F$. Charge conservation between the two phases allows for the calculation of

$$V_0 = V_{ref} + V_{ref} \frac{C_{ref} - C_x}{C_F} \quad (3.14)$$

The comparator output is therefore 0 when $C_{ref} - C_x$ is positive, and 1 when $C_{ref} - C_x$ is negative. This output affects the PCA value through SAR logic, which uses a binary search successive approximation algorithm [34].

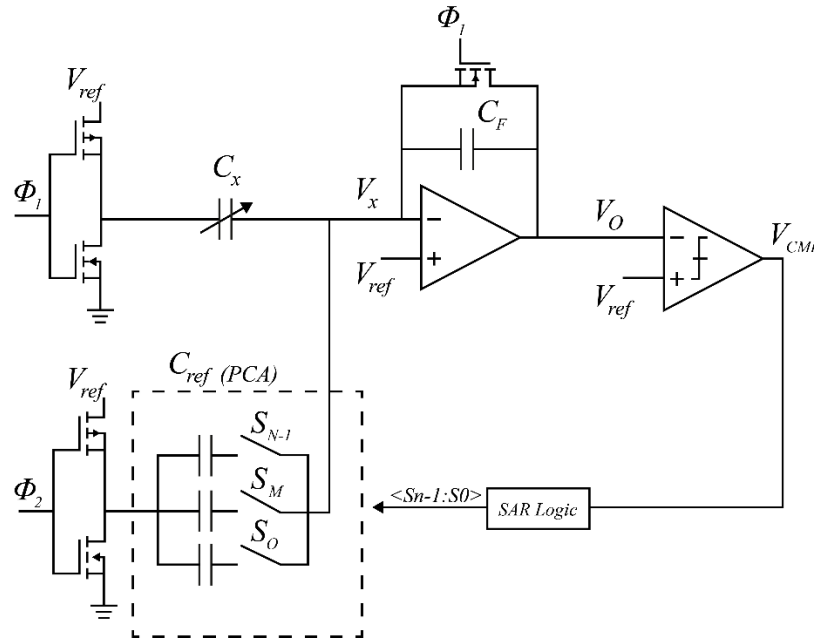


Figure 3.12: Capacitance to digital SAR circuit (Derived from [34]).

These types of structures allow the cancellation of parasitic capacitances, providing low-impedance nodes and thus allowing to reach high specifications in terms of resolution [52].

3.4. Comparison and conclusions

The analysis and explanation of the possible structures to perform capacitive readout and of their advantages, disadvantages, and improvement points helps to understand what structures are suitable for certain applications. After this qualitative investigation, a quantitative analysis related to the reachable specifications needs to be performed to draw conclusions. Multiple reviews on capacitive readout can be found in the literature, many of which focus their attention on three main specifications: resolution, measuring time, and energy consumption [34]. In this project, power consumption is not a constraint, and measurement time, at least in an initial stage, is not critical. Therefore, a comparison between the highlighted structures was conducted in terms of obtainable resolution. The highest resolutions related to each structure were identified in the literature, when possible, and are reported in decreasing order in Table 3.1.

Table 3.1: Best resolution specification for each type of topology.

Reference	Year	Author	Topology	Resolution (aF)
[53]	2016	P. Ciccarella	Capacitive to Voltage: Lock-in	0.065
[54]	2017	J. Perez Sanjurjo	Capacitive to Digital: Σ - Δ	5.4
[20]	2018	L. Zhong	Capacitive to Voltage	54
[55]	2015	Y. He	Capacitance to Time	255
[56]	2016	N. Courniot	Capacitive to Voltage: CBCM	450
[57]	2014	G. Scotti	Capacitive to Current	800

This table highlights how the best solutions in terms of resolution are to be researched in capacitive-to-digital and capacitive-to-voltage structures, which are the only ones that allow a readout with a resolution in the order of tens of aF (above the red line in the table). This finding is confirmed in multiple studies: according to [19] capacitive-to-voltage readouts provide the best resolution, while capacitive-to-digital (in particular Σ - Δ) are better when considering a compromise between resolution and power consumption [34].

Many of the reviews performed on the literature also consider a fourth specification: area occupancy. This fact highlights how the greatest part of the studies focuses on the development of integrated solutions, almost completely neglecting discrete component implementations. For the state in which this project is, an integrated solution would not be suitable, and therefore a translation of the investigated structures in the discrete component domain is required.

Lock-in amplifiers are complex and bulky structures that are particularly challenging to translate in the discrete domain. Attempts have been performed [58], but the translation causes a dramatic reduction in the resolution specification. The remaining solutions (capacitive-to-voltage architectures and Σ - Δ converters) can instead be implemented in discrete, and constitute therefore the best solutions for the continuation of this Master Thesis.

Commercial solutions: UTI and AD7746

*After investigating architectures and techniques that might prove suitable for the readout of capacitive changes in the aF range, a practical solution to be implemented and tested was researched. In the approach of such research, a key role was played by the aim of this project: to develop a **portable** and **discrete** readout. These two specifications restricted the design choices, ruling out the possibility to use very sensitive but bulky laboratory instrumentation (that will still be used for characterization and benchmark), and excluding the possibility to investigate and develop an Application Specific Integrated Circuit (ASIC), even if it would be the best solution in terms of electronics performance [34]. The possibility to reproduce one or more of the architectures seen in Chapter 3 on a Printed Circuit Board (PCB) using discrete components was considered, but the extremely strict performance requirements would have become an even bigger obstacle to overcome using a discrete component approach[59].*

Since several commercially available integrated circuits were developed specifically for challenging capacitive readout, a survey of the market was performed. This led to the identification of two components that claim to have similar or better resolution compared to the ICs identified in the literature, and whose behaviour was therefore to be further tested and investigated: Smartec's Universal Transducer Interface (UTI) [30] and Analog Devices AD7746 [60]. These two components are implementations of two of the architectures that were shown to have better performances in relation to capacitive readout, respectively a CSA followed by a voltage-to-period converter for UTI, and $\Sigma\text{-}\Delta$ capacitive-to-digital converter for AD7746. This fact contributed to the decision to investigate these two components for the required readout.

4.1. Smartec UTI

This integrated circuit was developed by Frank van Der Goes in 1996 as a result of his Ph.D. at TU Delft [32], and successively was commercialized by Smartec, which still produces it. The component is a multipurpose front-end interface for the readout of passive sensors such as resistors, thermistors, potentiometers, and capacitors. Sensing elements can be immediately connected to the component, together with two reference elements.

The component has sixteen readout modes, five of which are related to capacitance measurements. The interest for this thesis will be focused on mode 0 (C25) and mode 1 (C23), which allow the measurement respectively of five elements (three unknown capacitors and two known references)

and of three elements (one unknown capacitor and two known references) in the range of 0-2pF with high resolution (up to 14 bits) and high linearity.

The component is based on a period-modulated oscillator: its output is a periodic signal whose period length is proportional to the measured quantity. This output signal is microcontroller-compatible and can be therefore measured and quantized using a microcontroller. The same microcontroller can also be used for all the operations related to UTI, for example setting the operational mode, or communicating with a computer. The component is provided with an evaluation board [61], on which an 8 MHz microcontroller is mounted (PIC16F73I), together with multiple other components such as FT232RL (chip for interface and communication with a computer), TPS60110 (regulated charge pump to provide DC supply of 5V) and a 20 MHz crystal. In the board, also multiple solder pads array for connectors are present, on which sensors and references must be connected. In the case of modes 0 and 1 for accurate capacitive measurements, the measurement system is extremely sensitive to signals that are coupled with the input of UTI, such as capacitive-coupled interference signals. If the signal needs to be accurately measured, it is needed to route it using a shielded or coaxial cable rather than an unshielded wire, therefore a special solder pad for a coaxial connector is placed on the board.

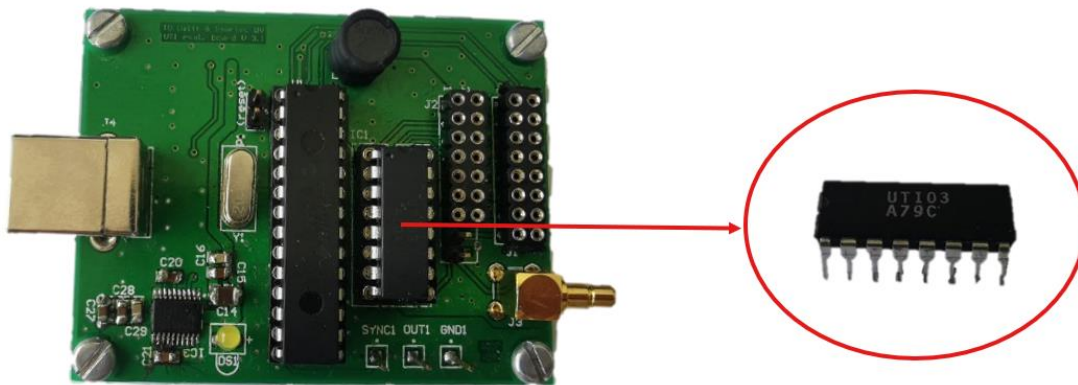


Figure 4.1: UTI evaluation board (packaging highlighted).

The component provides high accuracy thanks to some of the circuit techniques implemented, such as continuous autocalibration of offset and gain using the three-signal technique (Section 3.2.2) and suppression of interference at 50 Hz and 60 Hz.

4.1.1 Architecture and functionalities

The block diagram of the component is shown in Figure 4.2. Power supply is provided via V_{dd} and V_{ss} , while operational mode selection is performed by setting the value of four digital inputs SL1-SL4. Other digital inputs (CML, PD, SF) determine other aspects of UTI functionalities, such as the selection between a fast mode (≈ 10 ms measurement time) and a slow mode (≈ 100 ms measurement time), which is eight times slower but 3 bits more accurate. OUT pin is the output of the component where the period-modulated signal is provided, and needs to be connected to the microcontroller for quantization. The remaining pins, A, B, C, D, E, and F are used for the connection of the sensors. Pin A is an always-active input of the Capacitive-to-Voltage converter, which is therefore used as an input and to which all the sensors and references to be measured need to be connected. Pins B, C,

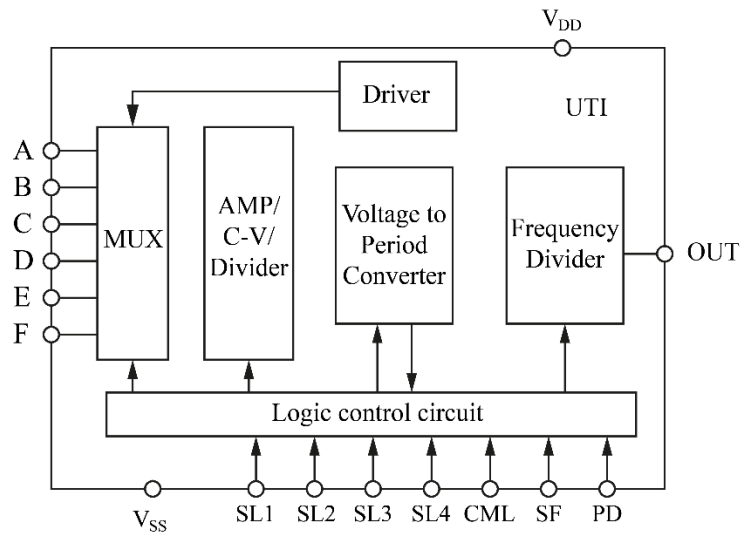


Figure 4.2: Block diagram of UTI.

D, E, and F are output pins that are used to provide the excitation signals needed to drive the passive devices to be measured. This output excitation signal is a square wave signal that is switched cyclically between the needed outputs by an internal multiplexer, so that in every moment only one device is measured at the same time. The connection of sensors and reference is shown in Figure 4.3, where it can be seen that all the elements need to have one terminal connected to input A and the other terminal connected to one of the different excitation pins available.

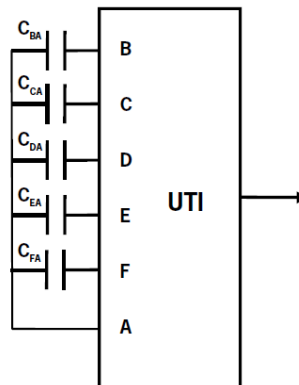


Figure 4.3: UTI required connection schematic.

In general, for better functioning of the device, reference capacitors must be set to certain values. The first one, associated with excitation B, is often not connected in order for the system to take into account possible offsets. The second reference, connected to excitation C, needs to be set to a value equal to or slightly higher than the maximum unknown capacitance to be measured. This approach guarantees that autocalibration removes any non-linearity effect [32]. In Mode 0, which measures five capacitors, the multiplexer switches the excitation sequentially and cyclically to output B (offset-reference 1), C (reference 2), D (unknown capacitance 1), E (unknown capacitance 2), F (unknown capacitance 3). In Mode 1, which only measures three capacitors, the two last excitations are skipped by the multiplexer.

An overview of how the output signal will appear for mode 1 was provided in Figure 3.3. The first period-modulated signal, with its period proportional to the offset capacitance, will be seen at the output (T_{ref1}). If pin B is not connected, this signal will have the shortest period. Second, the

multiplexer switches the excitation to pin C and the output period will now be associated with the second reference capacitor value. If this capacitor is the biggest, the period of this signal will be the longest (T_{ref2}). Finally, excitation is switched to output D, to which the unknown capacitor is connected. The period T_x is therefore a function of the unknown capacitor connected to excitation D, and the value of this capacitor can be obtained from Formula 3.2 using the values of the known reference capacitors.

The total period time of the three signals (T_{3-sig}) is the time that can be partially controlled with SF digital input, to decide between faster and more accurate measurements. As can be seen from Figure 3.3, anyway, smaller changes in measurement time are also determined by the value of the measured capacitances: small capacitors will lead to slightly faster measurement time, and big capacitors will cause longer time.

4.1.2 Interfacing

As explained, the output of the UTI is the period-modulated signal, and all the shown measurements and calculations need to be performed by the microcontroller.

The first task of the microcontroller is to digitalize the periods associated with the different capacitors to be measured. First, the number of clock cycles related to T_{ref1} (offset) is measured, then the same is done for T_{ref2} (reference), and for the remaining periods (one or three depending on the mode).

The hexadecimal value of this quantization can be communicated to a computer via USB, and accessed in the computer terminal using serial communication. All the previously explained calculations can be performed manually to obtain the final value of the measured capacitance.

The process was automatized with the development of a LabVIEW project, of which source code was provided and that was modified to better suit the needs of this project and to automatically export the measured data to MATLAB. Appendix H provides the related files, together with some explanations. From the LabVIEW script, it is possible to fully control the microcontroller behaviour, thus also controlling the UTI component. The user interface of the program is shown in Figure 4.4.

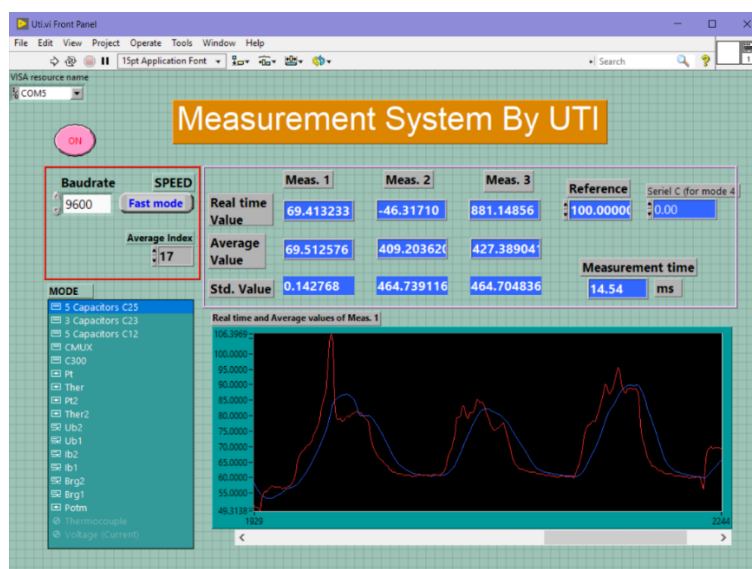


Figure 4.4: UTI user interface implemented in LabVIEW.

From the interface, the selection of UTI mode or of measurement speed can be performed. The program then automatically retrieves the data from the serial interface and performs the calculation, using the reference value that is provided by the user as input. This process is done in real time, and a graph of the measured capacitance as a function of time is plotted.

4.1.3 Improvements

Despite its extremely good specifications, UTI was developed as an interface for different types of sensors and was not specifically designed for capacitive sensing. Moreover, fast developments in technology make it hard for a component to remain in the high-quality range of the market for 26 years. As it was seen indeed, the specifications of UTI could reach 14 bits of resolution in the capacitive mode, ideally not suitable for the worst-case change in capacitance expected for the sensors developed by Shojaei Baghini. The reason why this component was taken into consideration and presented in relation to the readout of such sensors, is that in 2010 Heidary, a Ph.D. student at TU Delft developed an improved version of the component especially aimed at challenging capacitive readout [17]. In this improved design, the general block diagram and the working principle explained in Section 4.1.1 were left unaltered. The redesign of specific parts of the circuit to lower their noise contribution allowed Heidary to reach specifications up to four times better than UTI in terms of resolution, bringing the resolution down to 30aF.

The designed chip was manufactured and packaged, but never became a commercial product because of the niche application for which it was designed. Some samples were retrieved, and the device could be used for investigation in relation to this Master Thesis.

Even if most of the input and output of this innovative design corresponded to the ones of UTI, and even if the package used was the same (16DIL) the wiring diagram was not corresponding, and the new component could not be plugged in the UTI evaluation board. The first attempt towards the connection between the new component and a UTI evaluation board with a faster microcontroller (70 MHz) was performed using a breadboard and some jumpers, to verify the functioning of the connections (Figure 4.5).

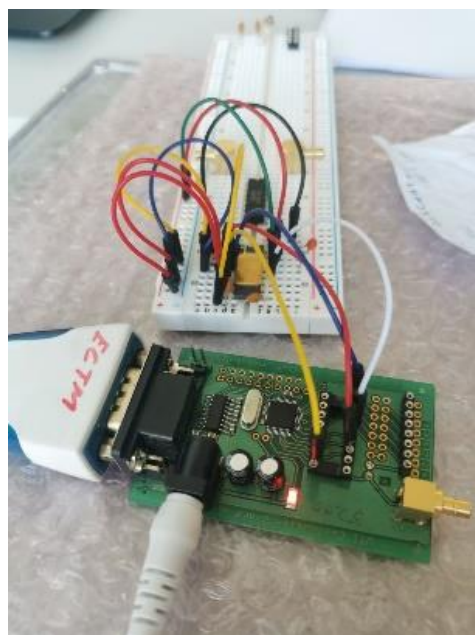


Figure 4.5: Setup for test of evaluation board compatibility.

Once the connections and the correspondence between the UTI pinout and the new component pinout were established, a PCB was designed to be used as an adapter, simply routing the traces from the evaluation board to the required pin of the new component. For the digital inputs of the new components, different from the ones used by UTI, a manual approach has been used for simplicity, and they have been routed to V_{dd} or to V_{ss} using manual switches. The designed and tested board, placed on top of the UTI evaluation board, is shown in Figure 4.6.

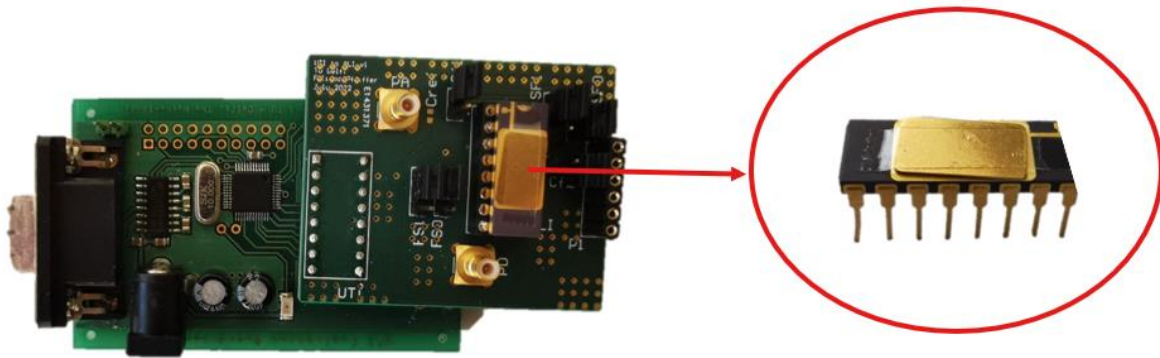


Figure 4.6: UTI evaluation board with new board on top, to use Heidary's component (packaging highlighted).

4.2. Analog Devices AD7746

Analog Devices AD7746 is an integrated circuit implementing a capacitance-to-digital converter. It was specifically designed for challenging capacitive readout, and capacitors to be measured can be directly connected to the input of the component, without the need to provide any external references. The component has two capacitive channels: each of them can be configured as single-ended or as differential, for a total of four capacitive elements connected to the component (two differential pairs). All the connected capacitances need to be in the range of $\pm 4.096\text{pF}$ and the readout provides up to 21 Effective Number of Bits (ENOB), translating to best case resolution of 4aF .

AD7746 allows flexibility in the measurements, with the possibility to select between eight different measurement times from 11ms to 110ms . The highest resolution is associated with the longest measurement time, but for a measurement time of 62ms (correspondent to 16.1Hz) simultaneous rejection of 50Hz and 60Hz interference is provided. The component also provides the possibility to enable or disable chopping, providing a slight increase in performance with the drawback of longer measurement time.

The component is based on a $\Sigma\text{-}\Delta$ capacitive to digital converter; therefore, the measurement is already digitalized and can be immediately used by a microcontroller for further processing. This microcontroller also manages all the other aspects related to the board, such as the selection of operations and communication to a computer.

An evaluation board is provided [62], on which AD7746 is mounted together with all the needed coaxial connectors, a CY7C68013A-56LFXC microcontroller with an integrated USB controller to allow communication with a host system such as a computer, and an ADP3303 3.3V voltage regulator.

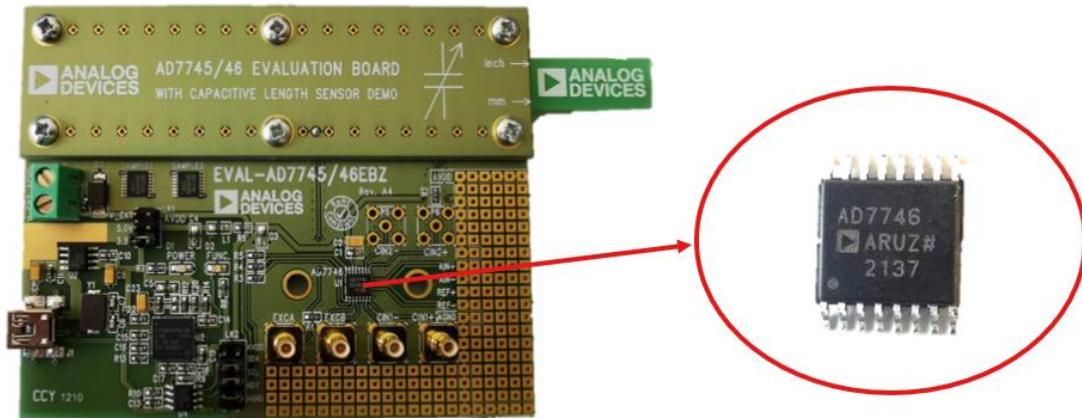


Figure 4.7: AD7746 evaluation board (packaging highlighted).

4.2.1 Architecture and functionalities

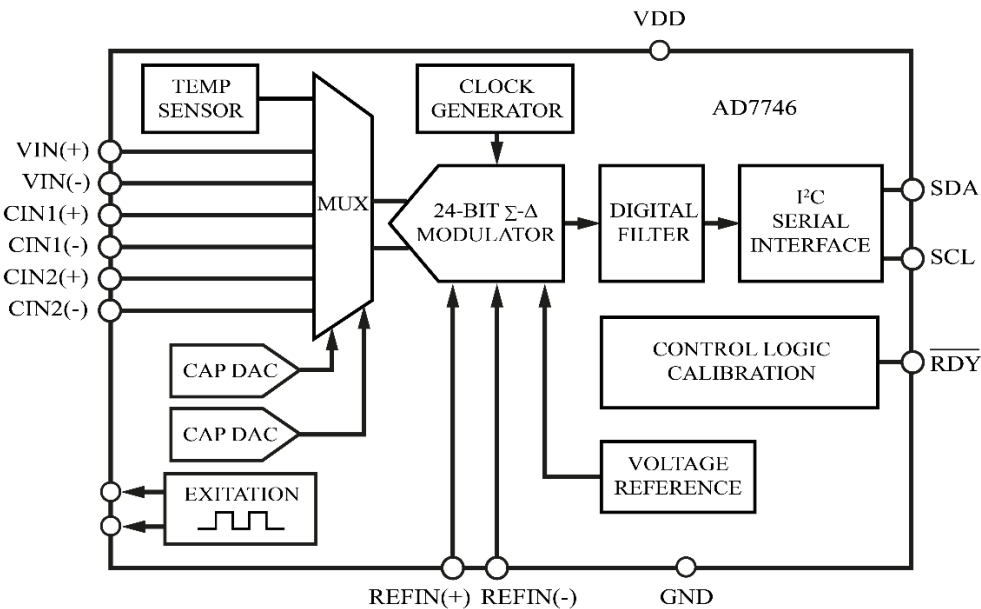


Figure 4.8: Block diagram of AD7746.

The component is based on a 24-bit second order Σ - Δ modulator taking care of the translation from an analog capacitance to a digital signal, followed by a third-order digital filter. It also has an on-chip I^2C serial interface that allows robust and easy communication with a microcontroller. SDA and SCL pins are used for communication. The address of the device is fixed and cannot be changed.

The on-chip voltage reference is powered by VDD and GND pins. The component also provides two different excitation outputs (EXC1 and EXC2), to be used for driving the two different capacitive channels, which can be active at the same time and provide 32 kHz square wave signals.

Sensing capacitances must have one terminal connected to one of the excitations, and the other connected to CIN1+ or CIN2+ depending on the channel that wants to be measured. For differential readout, one capacitance needs to be connected to CIN1+ (or CIN2+) and the other to CIN1- (or CIN2-). Differential devices need to be driven by the same excitation signal. An on-chip analog

multiplexer connects the two capacitive inputs to the input of the Σ - Δ , but since the input of this CDC is single, only one channel can be converted at a single time. Therefore, it is not possible to have the simultaneous conversion of both channels.

4.2.2 Interfacing

The AD7746 evaluation board is provided with software that can be used for interfacing with the microcontroller mounted on the board. Via this software, all the operating modes of the AD7746 can be selected and activated. The microcontroller gets information from the software and translates this information, writing them in AD7746 registers that control the mode of operation. Moreover, the microcontroller can also read the information that is stored in registers and that contains the data that are read out by the component. These data are transmitted by the microcontroller to the software, which provides real-time data in the user interface, also plotting them as a function of time.

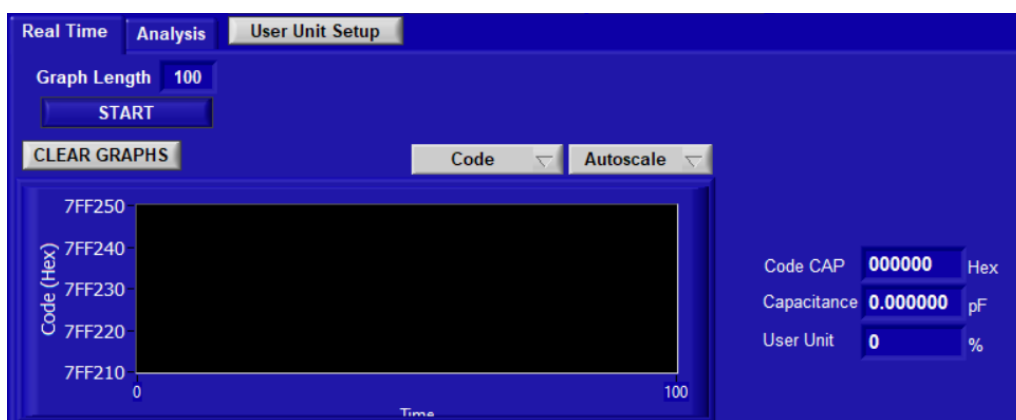


Figure 4.9: AD7746 software's user interface.

4.3. Preliminary tests: accuracy

The suitability of the identified platforms in relation to the needs of this application has to be checked. To do so, some preliminary tests regarding their behaviour were performed. The first test relates to the accuracy of the values read out by the components: it is interesting to check both the behaviour of the boards in terms of static readout, but also in terms of readout of variable capacitors (such as in the final application), therefore both these tests were performed.

4.3.1 Static benchmarking

During the tests related to measurements of capacitance with a fixed value, standard 1.8pF single-layer ceramic capacitors with 10% tolerance were used as Device Under Test (DUT). Benchmarking with accurate readout instruments, which provided reliable results, was performed. Agilent U1732A handheld LCR meter was chosen as an instrument for the benchmark, because of the possibility to perform measurements of through-hole capacitors, resistance, and inductors directly inserting their leads into the instrument, thus reducing the effects of parasitic capacitances and inductances coming from interconnections and from the leads themselves. The instrument provides a resolution of

0.01pF, not as high as the resolution offered by UTI and AD7746 but still suitable in relation to the capacitance range of the DUT.

The procedure for the measurements with the AD7746 board is very straightforward: the cables are connected, the residual offset is removed via calibration, the DUT is plugged, and the measurement is performed.

For UTI, the procedure is slightly more complicated since there is the need to also provide a reference capacitance to be measured, and whose value needs to be precisely known and provided as an input to the measurement system for the calculations, as explained in Section 3.1.1. The measurement of the reference capacitor was performed with U1732A, and the value was provided as input in the software. The connections for excitation and input signal of the UTI were made (Figure 4.10a), offsets were removed for calibration and finally, the DUT and the reference capacitors were plugged for the measurement to be performed (Figure 4.10b).

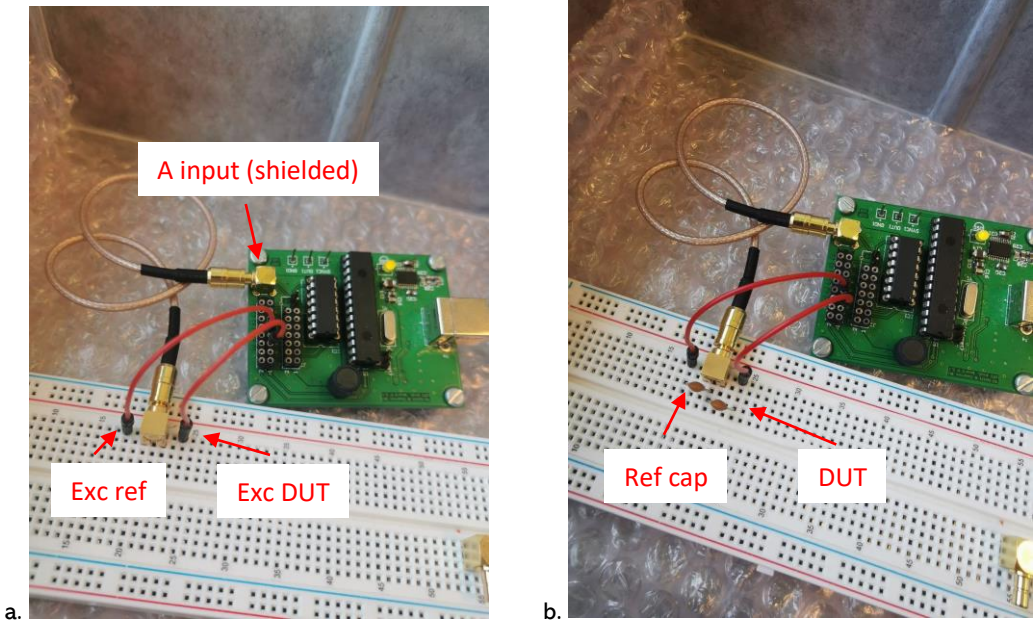


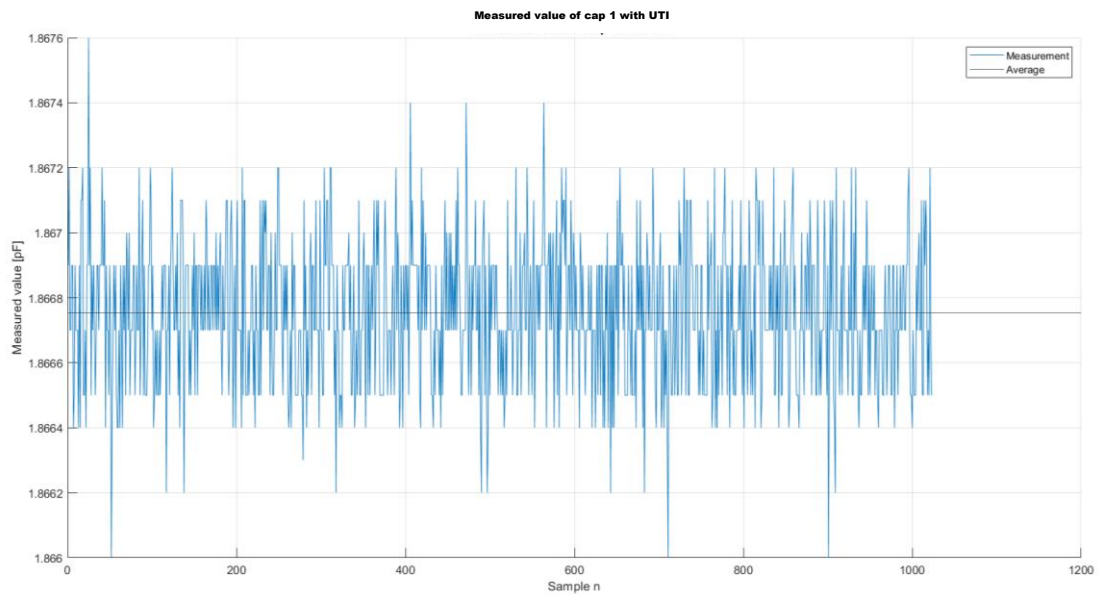
Figure 4.10: Connection setup and offset removal (a) and measurement (b) with UTI.

The results of one of the measurements for AD7746 and UTI are plotted respectively in Figure 4.11a and 4.11b, and the comparison is shown in Table 4.1.

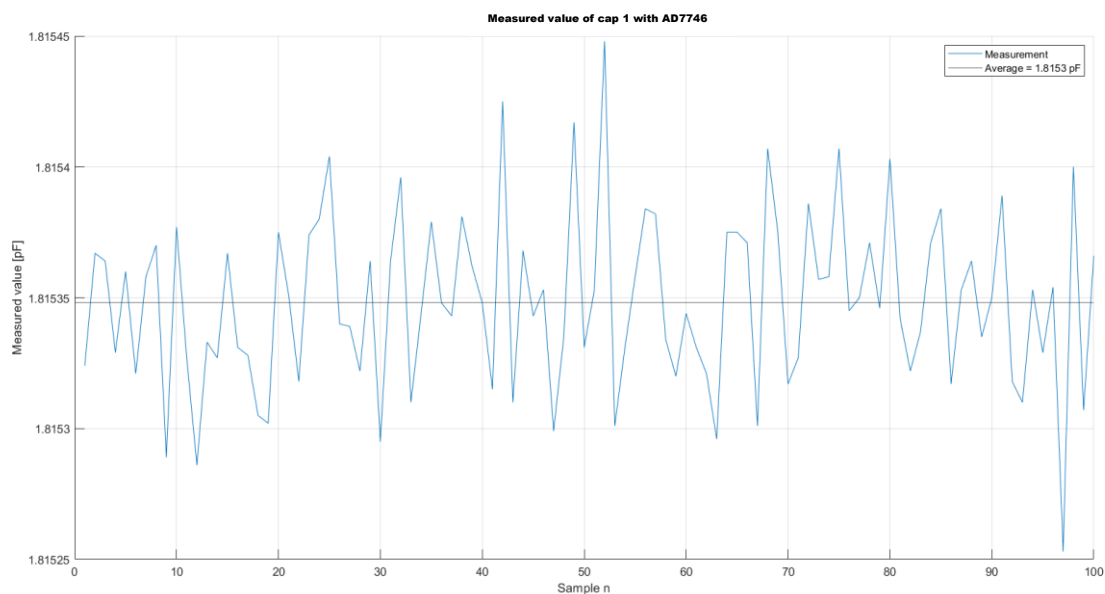
Table 4.1: Results of measurement of the same capacitor with different readout instrumentations.

DUT	Agilent U1732A	Smartec UTI	Analog Devices AD7746
1.8pF capacitor with 10% tolerance	Average of 10 measurements: 1.8663pF	Average of 1024 measurements: 1.8667pF	Average of 100 measurements: 1.8153 pF

The measurements have been performed for different DUTs of the same batch, and always provided comparable results, showing good behaviour in terms of accuracy for both components when the measurements were related to capacitors with a constant value.



a.



b.

Figure 4.11: Plots of measurements for UTI (a.) and AD7746 (b.).

4.3.2 Investigation of variable capacitors and dynamic benchmarking

The first test provided a good indication, but to prove the suitability of the selected components information about their dynamic behaviour was needed, and even more, the evaluation of a capacitive range closer to the one of the final application was requested.

Variable capacitors (or trimmer capacitors) were researched in the market, but the smallest available had a variable range of 1.5pF-3pF for SMD components and 1.5pF-5pF for through-hole components.

The question then shifted to how to implement variable capacitance, while the sensors for the final application were still in manufacturing. The solution was found in the design of a PCB, on which different capacitors were soldered and switches were used to select which capacitor to measure, thus mimicking the behaviour of a variable capacitor whose value changes in discrete levels. These

boards were developed (Figure 4.12), and their schematic and working principle are presented in Appendix B.1.



Figure 4.12: Designed PCB to implement variable capacitance.

The capacitances soldered on these boards were the smallest capacitance available in the market. Three equally spaced levels were chosen for the measurements, respectively 0.1 pF, 0.2 pF, and 0.3 pF. These values are in line with the expected base capacitance of the sensors, but the difference between one value and the other is orders of magnitude bigger than the change expected in the sensors. Nonetheless, these were the most suitable choices that the market offered for such a test.

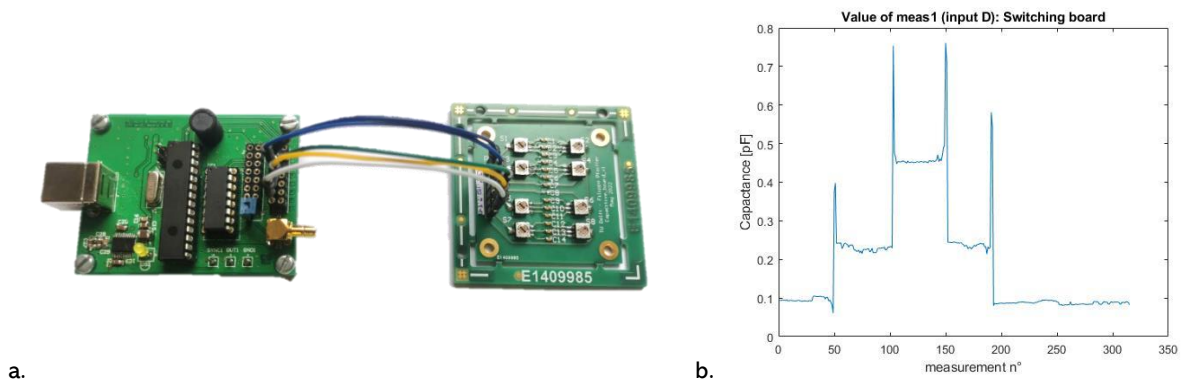


Figure 4.13: Connection between capacitor PCB and UTI evaluation board (a.) and measurements plot (b.).

The boards were connected for measurements (Figure 4.13a) and results were obtained as shown in Figure 4.13b. The result showed compliance with the expected result in terms of behaviour (neglecting the spikes caused by the switching), showing the three clear and reproducible levels detected by the measurements. The approach described in the previous subchapter for benchmarking the measurements with precise instrumentation was used, and all the measurements for all three levels were confirmed. Despite this, the test showed the first problems in relation to such small capacitance detection: the levels were not in agreement with their expected values (0.1 pF-0.2 pF-0.3 pF) as can be extracted from the figure. The discrepancy between the expected value and the measured value is to be explained by the physical phenomena that affect capacitive measurements and that are difficult to predict and quantify, such as parasitic couplings between the

connection cables or between the PCB traces. These two aspects were identified as weak links in the measuring process, and to reduce their effect a second PCB was designed with some improvements: all the connections of these new boards were designed to be routed via coaxial cables to provide shielding for the signals, and for the same reasons grounded planes were placed around the traces on the PCB, to reduce the effect of couplings between one trace and the other.

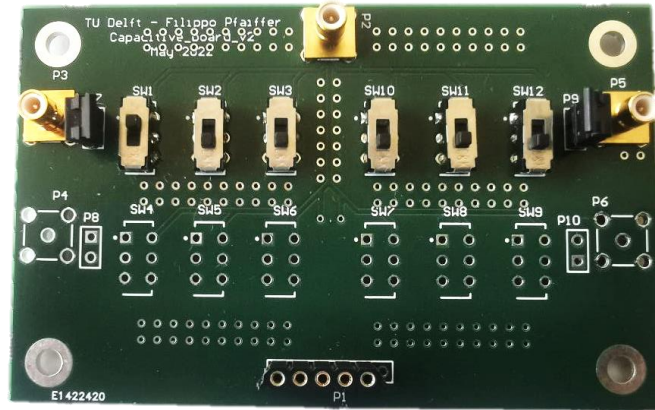


Figure 4.14: Re-design of PCB to implement variable capacitance.

This second board provided results that were slightly better than the previous version, but the results were still higher than expected. This led to the conclusion that the parasitic capacitances of the switches themselves were playing a role in the measurements, and crosstalk between different switches was also documented. The development of a board to mimic the behaviour of a changing capacitance was an approach that proved to be not adequate for such a small capacitance range and was therefore discarded. A different method to quantify the quality of the identified readout was therefore investigated.

4.4. Preliminary tests: Noise behaviour

In the last sections the focus was on the accuracy of the measurement, which is the proximity of the measured value to the real value. It was investigated by analysing the average of the signal, and how close this average was to the benchmark measurement. Another interesting aspect that can be evaluated from a set of measurements, which relates to the dispersion of the measurement set and to the measurement's repeatability, is how precise these measurements are (Figure 4.15).

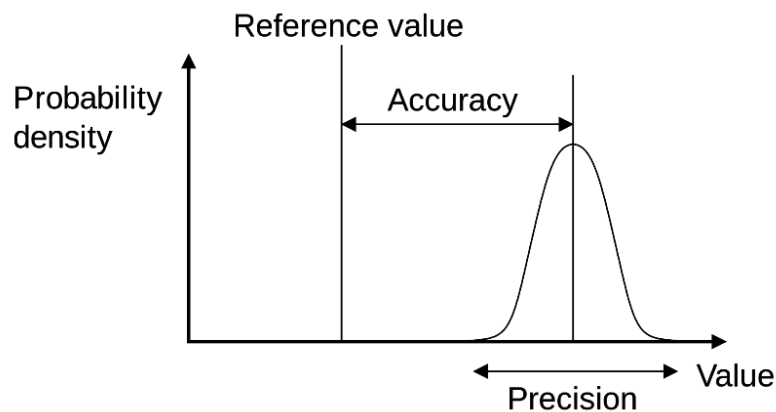


Figure 4.15: Graphic illustration of definitions of accuracy and precision.

Measurements might be non-precise because of the influence of multiple effects: all the effects that stochastically cause a variation in the results of measurements are commonly grouped by the definition of noise and interference. Therefore, the effect of these phenomena is to influence the standard deviation of a set of measurements. The increase in the standard deviation of a set of measurements, caused by noise or interferences, translates in practice into a reduction in the resolution of the instrument itself, which is defined as the smallest change that can be detected by that instrument.

It is therefore clear that noise plays a fundamental role in the analysis of the behaviour of a readout circuit, being the first and most important limiting factor for its performance in terms of resolution [36]. Some of the main effects contributing to noise are briefly explained in the next subchapters.

4.4.1 White noise

White noise, also known as Gaussian noise, is a type of noise that happens regardless of the frequency of the signal that is being investigated, and because of that it is constant in the frequency spectrum (white). It is a random noise, but obeys a Gaussian distribution (Figure 4.16) which also explains its name. The two main contributions to this type of noise are given by Johnson-Nyquist noise (or thermal noise), which is the electronic noise that is intrinsically coupled to temperature, being the effect of the thermal agitation of electrons, and by shot noise, which is a random fluctuation in flowing currents caused by the discrete nature of electric charge [27].

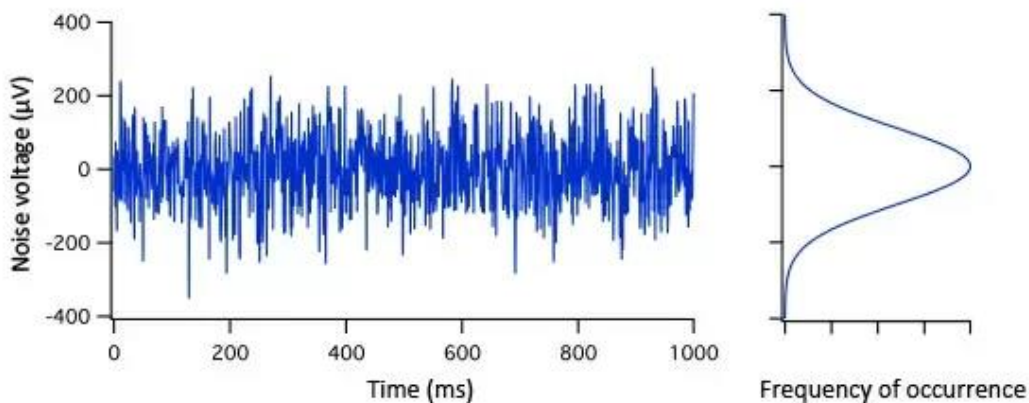


Figure 4.16: Example of signal affected by white noise (Derived from [63]).

White noise is the main limiting factor in measurement systems, and it cannot be eliminated, but only reduced. To reduce it, it is possible to use signal processing techniques such as averaging, which collects more samples and averages them to provide a more precise result. This approach is expensive in terms of time (measurement time is proportional to the number of samples that are averaged), but is better in terms of Root Mean Square (RMS) noise, being

$$RMS_{noise} \propto \frac{1}{\sqrt{n^{\circ} \text{ of } _ \text{ samples}}} \propto \frac{1}{\sqrt{T}} \quad (4.1)$$

Another possibility to reduce noise is to use a different circuit design approach: every element in the design of an IC affects its final noise behaviour, and more noise-efficient designs can be investigated. This was what happened in the design of the improved version of the UTI component that was discussed in Section 4.1.3.

4.4.2 Flicker noise

A second contribution to noise is given by flicker noise, also called $1/f$ noise or pink noise. The reasons for this noise are multiple, but it is mainly caused by the effect of generation and recombination currents in semiconductor devices [27]. This noise is pink, meaning that its power spectral density in the frequency spectrum is proportional to $1/f$. It is characterised by a corner frequency f_c , that is the frequency at which the power spectral densities of flicker noise and of white noise are the same (Figure 4.17). The design of the circuit influences this corner frequency, which should be set as low as possible for flicker noise to have a smaller effect. Since its contribution is mainly visible at low frequencies, this type of noise can be almost completely removed by chopping, as explained in Section 3.2.1.

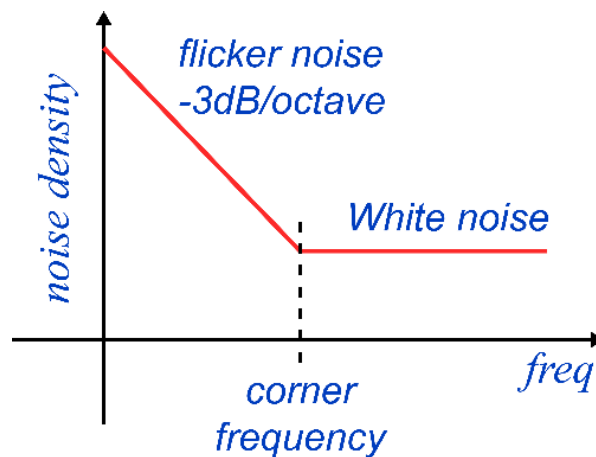


Figure 4.17: Frequency spectrum of flicker noise and white noise.

4.4.3 Quantization noise

Quantization noise is the name that is given to the error that is generated by the process of quantization of an analog signal, and this specific noise is introduced by analog-to-digital conversions. The general idea of the conversion is shown in Figure 4.18, where an AND operation is performed between a signal with period T to be quantized and the clock signal of period t_s .

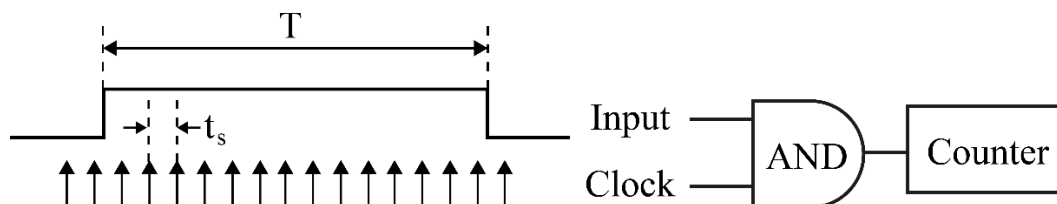


Figure 4.18: Graphic illustration of quantization process (Derived from [17]).

In general, T might not be a multiple of t_s and therefore the result of the AND operation might introduce an error, which is the difference between the continuous analog value and the discrete digital value. This error has a mean of $\frac{t_s}{2}$ and a uniform distribution in the interval from 0 to t_s . The

standard deviation of this noise is given by $\sigma = \frac{1}{\sqrt{6}} \frac{t_s}{T}$. As it is clear from this relation, a possibility

to reduce quantization error without interfering with measurement time is to reduce the clock period t_s increasing the clock frequency (and therefore the power consumption), thus using a faster microcontroller for the quantization. This approach was also used by Heidary in his work to improve the UTI component through the development of the evaluation board with a faster microcontroller shown in Figure 4.6.

4.4.4 Noise analysis

Because of the huge importance of noise in a readout circuit, the analysis of the noise behaviour for UTI and AD7746 has been performed. It was conducted for both devices in the same conditions (at the same time, in the same environment, and with the same connections). Measurements of a fixed capacitance were taken, and an analysis of the data acquired was performed. Out of the obtained data, the average could be calculated. The difference between every single datum and the average value provides the error for each data point. These errors might be positive or negative, so to take both contributions into account they need to be squared. The mean of the errors squared is called variance, and the square root of this value is the RMS value for the measurement, which corresponds to the standard deviation of a set of data.

From the data, also the peak-to-peak error could be extracted, by simply calculating the difference between the maximum measured value and the minimum measured value.

To evaluate the number of bits needed to encode this noise, the \log_2 of the RMS noise can be calculated, which translates to the bit loss caused by the noise. Subtracting this value from the maximum number of bits that a readout circuit provides, the Effective Number of Bits (ENOB) of the readout circuit is provided. Dividing the maximum readout range by 2^{ENOB} , it is possible to extract the effective resolution of the readout circuit in a way that takes into account the presence and the effect of noise in the readout. In the same way, the resolution considering the Peak-to-Peak (p-p) noise can be investigated. Both values were extracted for both platforms, and the results are reported in Table 4.2.

Table 4.2: Comparison of noise figures for AD7746 and UTI.

Device	AD7746	UTI
Resolution (RMS)	12.2 aF	30.5 aF
Resolution (p-p)	101 aF	122 aF

Since the magnitude of the signal generated by the application of force is not precisely known (at this stage the force itself could only be estimated), it was impossible to conduct an analysis involving SNR data. Despite that, since the signal to be read out is the same for both platforms, a comparison in terms of noise figures can be performed without compromising the conclusions.

A final interesting evaluation was conducted to identify the frequency spectrum of the noise that was measured in the data acquired. To perform this analysis, a Fourier transform of the dataset was performed (Figure 4.19). The results obtained showed the average value of the measurements in correspondence to 0Hz frequency (DC), and a lower constant baseline for all the higher frequencies, thus indicating white noise as the main contributor to the measured disturbance.

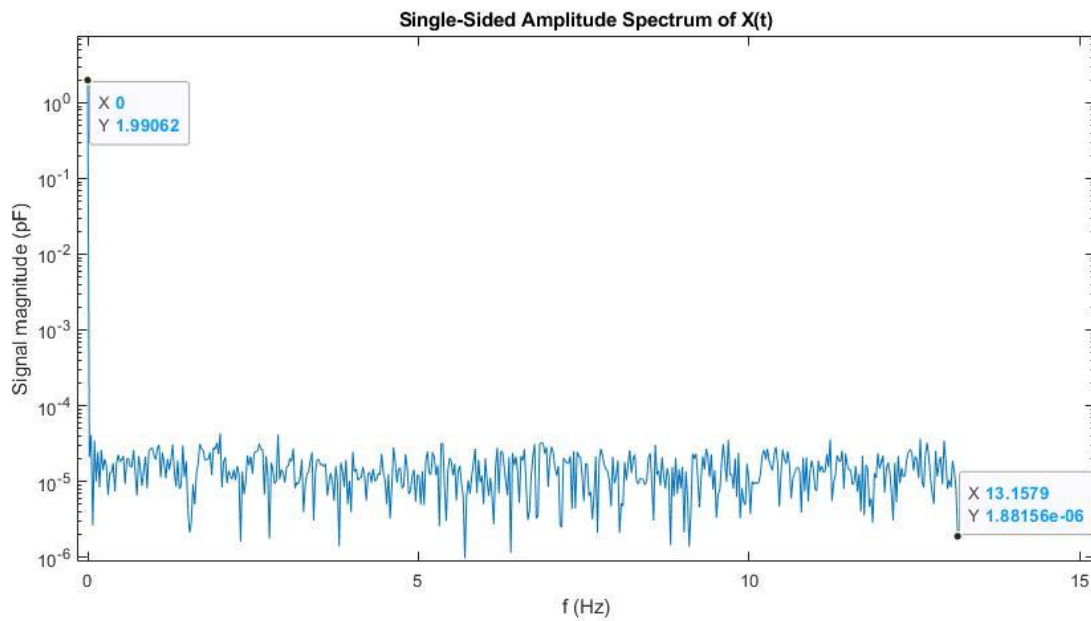


Figure 4.19: Fourier transform of noisy signal acquired using UTI.

The main drawback of this approach is that the Fourier transform only can evaluate frequencies up to $\frac{f_{\text{sampling}}}{2}$, which in this case corresponds to 13.1579 Hz, but this strategy already provides a good indication of the expected behaviour of noise.

4.5. Conclusion and final choice

The results, both in terms of accuracy and in terms of resolution, showed similar behaviour for the two components investigated, with slightly better behaviour in terms of resolution for the AD7746. This advantage in the Analog Devices component could in principle be compensated using the improved version of UTI, which should perform better than UTI itself. Since in any case performance figures of the two platforms were very similar, the final role in the decision of the main component to be used for trying to readout the developed sensors was played by two qualitative aspects: in first place, AD7746 signal routing is entirely done via coaxial shielded cable, ensuring a higher rejection of external disturbances; secondly, AD7746 does not need to provide any external reference, thus showing a bigger flexibility for the use of the device. Because of this, AD7746 is used for all the measurements performed in the next chapters of this Master Thesis. Despite this choice, UTI proved to have similar performance and could in principle be further investigated as well.

5

System Fabrication and Assembly

The design and fabrication of the EHT platform with the integrated sensors were discussed in Chapter 2. The investigation of a possible readout circuit was conducted in Chapter 3, followed by the identification of a suitable solution and a first set of tests to prove this suitability (Chapter 4).

The focus of the project now moves towards the research of an effective way to connect the sensors to the readout interface, and therefore to the research of a methodology to properly connect the entire system - made up of sensors and readout.

A viable way to connect the sensors to the readout is to place them on an appropriate PCB that simply routes the signal needed for the correct functioning of the sensors. The transfer from the wafer on which sensors are fabricated, and the connection of the sensors to the PCB on which they should be measured will be shown in this chapter. This process proved to be very delicate and gave origin to multiple failure modes, which were analysed and reported. Alternative assembly processes were investigated to obtain higher reliability and yield.

5.1. PCB Design

A PCB was specifically designed and produced to transfer sensors on its top and to ensure the correct signal routing between the sensors and the readout. At first, a footprint for the sensors was designed with the dimension indicated in Figure 5.1.

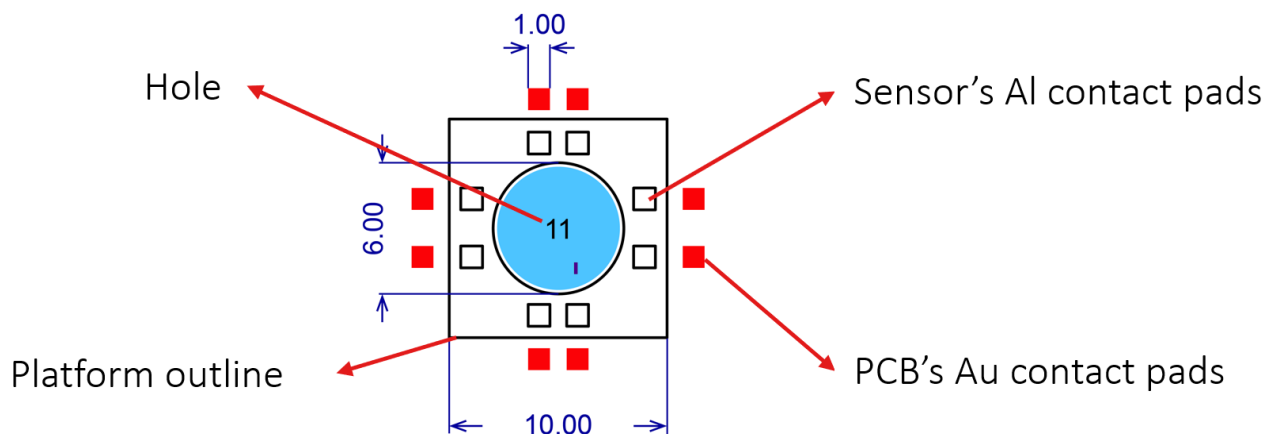


Figure 5.1: Footprint design and dimensions in mm for the ETH platform.

A short connection between the sensor's contact pad and the respective PCB's contact pad is established. In the center of the footprint, a 6 mm-diameter hole is placed. This hole is placed in correspondence with the well with pillars and sensors, and the reason for its presence is to maintain the transparency of the system in case pillar motion needs to be measured with standard optical displacement measures. The result is that the platform is attached to the PCBs on its sides and corners, while the central part of the platform (where the well is located) is configured as a suspended PDMS membrane.

From the PCB's contact pads, traces are routed towards connectors, and cables are used for the connection of these traces to the readout board. Since every sensor in the platform has two contact pads, (one for excitation and one for the output signal) the routing of the traces must be done accordingly: traces routing excitation signal will run from input connectors to the inputs of the sensors, traces routing the signal to be read out will run from outputs of the sensors to output connectors.

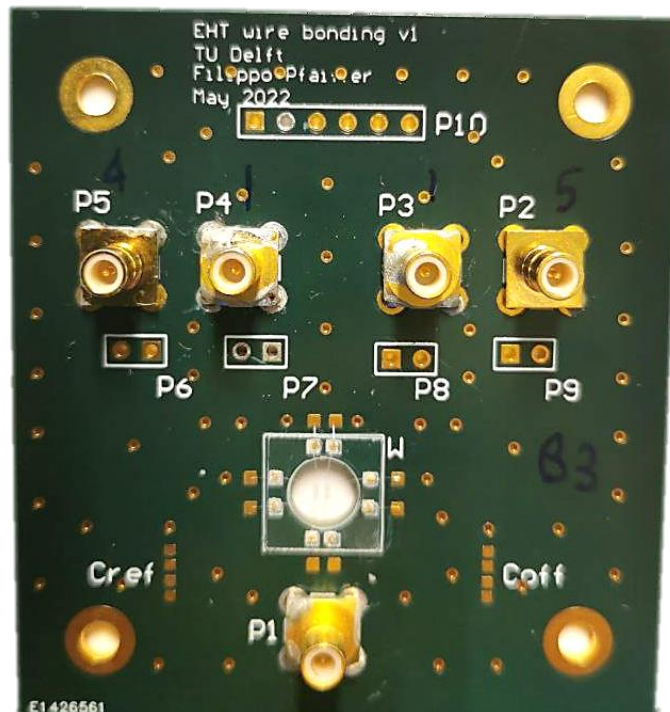


Figure 5.2: Developed PCB for EHT assembly process.

The board was designed to be used in connection to the AD7746 component, and the connections were designed to match the inputs and outputs of such a device. Despite that, on the same board, some features were placed for it to be compatible with the UTI connection diagram and working principle. To perform a readout with AD7746 the excitation should be connected to P1, which is connected to four of the eight contact pads (one for each sensor) thus providing the excitation to every sensor. The remaining four contact pads are connected respectively to P2, P3, P4, and P5. One of these connectors (depending on which sensor will be measured) need to be connected to CIN1+ or CIN2+ in the AD7746 evaluation board, as explained in Section 4.2.1.

If UTI readout wants to be performed, the single readout (pin A) needs to be connected to P1, and the multiple excitations (D, E, or F) need to be connected to one of the remaining pads using connector P10 and shorting pin headers P6, P7, P8, P9 with a board jumper. For the readout with UTI, solder pads for the two reference capacitances are provided as well.

On the board, for the reasons explained earlier, both coaxial connectors for shielded wires and headers for normal wires are mounted. To keep the coupling with the measurement environment as low as possible, the coaxial readout is preferred.

For the same principle, traces on the PCBs should be shielded as well from couplings between them and with the external environment. Techniques for reducing parasitic coupling of the traces were used in the design phase: the traces have been routed on both sides of the PCBs, and on each side, ground planes were designed to surround and shield the traces.

The effect of these ground planes could be investigated by performing capacitance measurements on the board when no capacitors are connected and when the planes are not connected to the ground, therefore not providing the shielding. Performing this type of measurement allows the decoupling of the effect of PCB parasitic capacitances from the effect of the measured capacitance, thus providing the offset that would be caused by the PCB design if traces were not shielded. For these measurements, Agilent 4294A Precision Impedance Analyzer was used together with a probe station, in which probes are placed on the contact pads of the PCBs. Multiple data points were measured for each parasitic capacitance measurement, and the contribution for all four different traces of each PCB was measured. Each horizontal line in Figure 5.3a shows the measured values for one trace. It can be seen that the parasitic capacitance in all the traces is between 200fF and 300fF. The differences between each measurement are given by dispersion in the measurements themselves, but also by the fact that each trace has a different length and routing as shown in Figure 5.3b, therefore the parasitic capacitance is expected to be slightly different.

Repeating the same measurement with the planes connected to the ground provides signals that are all aligned in the order of a few fF, thus proving that the grounded planes have a major influence in reducing the offset generated by the parasitic capacitance in the traces, which was just shown to be in the 200-300fF range.

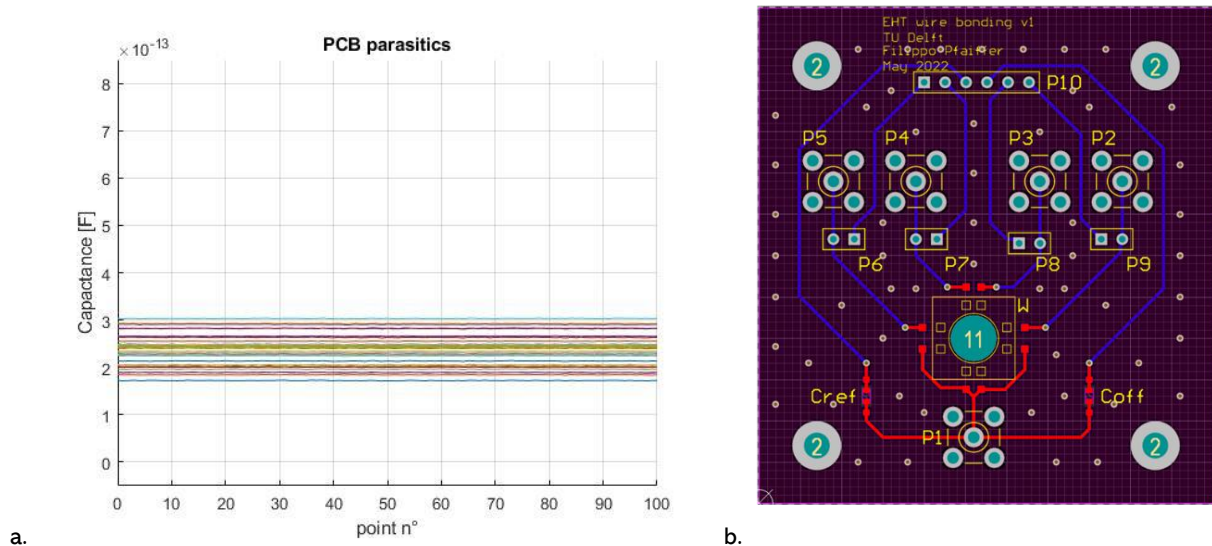


Figure 5.3: PCB parasitic capacitances measurements when planes are not grounded (a.) and PCB traces routing (b.).

5.2. The assembly procedure

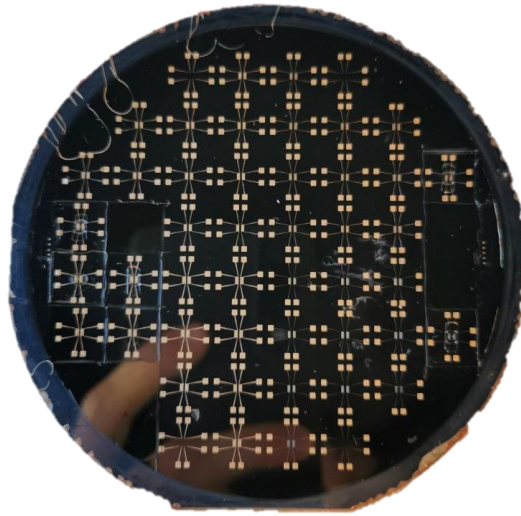


Figure 5.4: Sensors at the end of fabrication process on a 4-inch Silicon wafer (some platforms are missing because of the detachment required for the assembly process).

After the microfabrication process explained in Section 2.2.2, 48 platforms with integrated sensors (four per platform) lie on a thin PDMS layer spin-coated on top of a silicon wafer (Figure 5.4). A previously experimented process for the assembly of similar structures will be explained in this Section. A simplified cross-section of the process in the different steps is shown in Figure 5.5.

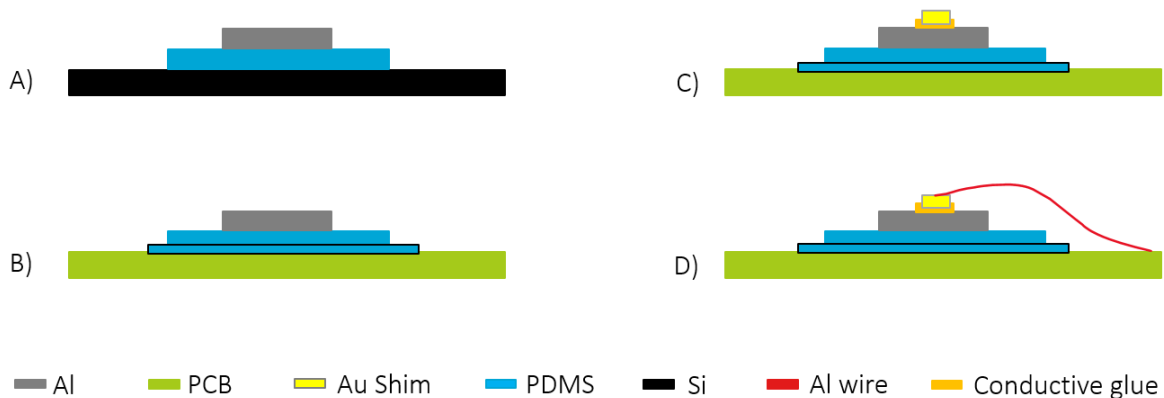


Figure 5.5: Cross-section of assembly procedure step by step. Platforms made of PDMS and aluminium are transferred from Silicon wafer (A) to the PCB (B). Conductive glue and shims are placed on top of the Al contact pads (C) and wire bonding to the PCB is performed (D).

The first stage is to manually cut the thin PDMS layer to allow the individual transfer of single platforms on the PCB. This provides diced PDMS platforms of around 10mm x 10mm with aluminium on top, which are still placed on the Silicon wafer (Figure 5.5A).

These platforms are manually detached from the Silicon wafer on which they lie using a thin blade, and carefully aligned to the footprint that was shown in Figure 5.1. On the PCB, in correspondence with the footprint, a small droplet of uncured PDMS is placed. The platform is placed on top of this droplet and can slide to be precisely aligned. The whole PCB is then placed in the oven at 60 °C for slow curing of the PDMS droplet, which will function as a glue between the PCB and the transferred

platform (Figure 5.5B). The next stage is wire bonding of aluminium pads of the sensors to the golden pads of the PCB. An intermediate step needs to be performed before this stage if wire bonding wants to be used for the connection. Classical wire bonding is a process that uses pressure and ultrasonic force to connect the wire to the substrate, and therefore a flexible substrate like the thin aluminium pad (in turn positioned on top of the flexible PDMS substrate) is not suitable for this process. This can be solved using specific gold shims: small rigid gold dices that can be placed on top of the contact. Each shim is glued using specific conductive glue dispensed on top of the aluminium pad. Then, using a pick-and-place tool, the shim is placed on top of the layer of glue to ensure electrical contact between the aluminium pad and the gold shim. After this, the glue needs to be cured at 125°C for 2 h (Figure 5.5C).

When the glue is cured, aluminium wire bonding can be performed between the top of the gold shim and the top of the gold contact pad placed on the, providing electrical connection between the PCB and the sensors. A picture that clearly shows the principle of the last passages is shown in Figure 5.6.

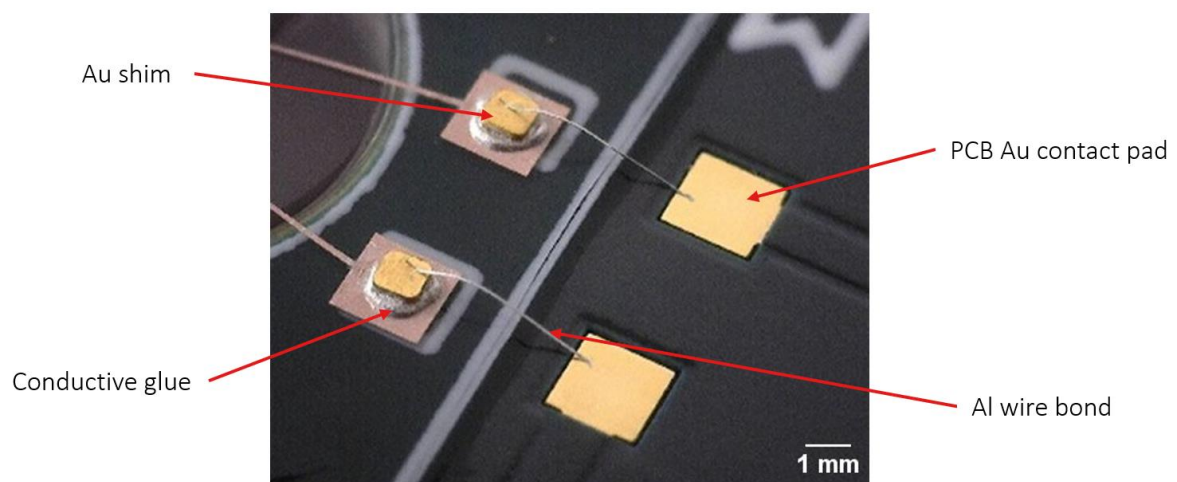


Figure 5.6: Wire bonding performed between gold shims and PCB contact pad. Conductive glue is visible below the shims.

This assembly procedure is not standard and involves many passages that need to be performed manually. The need for the development of such a process derives from all the constraints that originated from a complex and multidisciplinary project like this: above all, flexible substrate which is needed for the correct mechanical behaviour of the platform, is rarely used in relation to standard assembly procedures and often requires the implementation of additional steps.

5.3. Mechanical failure modes

The assembly process just explained proved to be extremely challenging and highly dependent on the manual skills of the person performing the passages. In many cases, the thin and delicate structure of the sensors was damaged by the manually performed steps, but also by the passages implying the use of machinery (such as wire bonding). All the passages were documented, and visual inspections before and after them (together with measurements shown in Chapter 6) helped to highlight criticalities in each of them, that often generated physical failures in the aluminium traces.

The main failure mode that was reported was related to the cracking of the long aluminium traces connecting the spiral sensors to their respective contact pads (Figure 5.7).

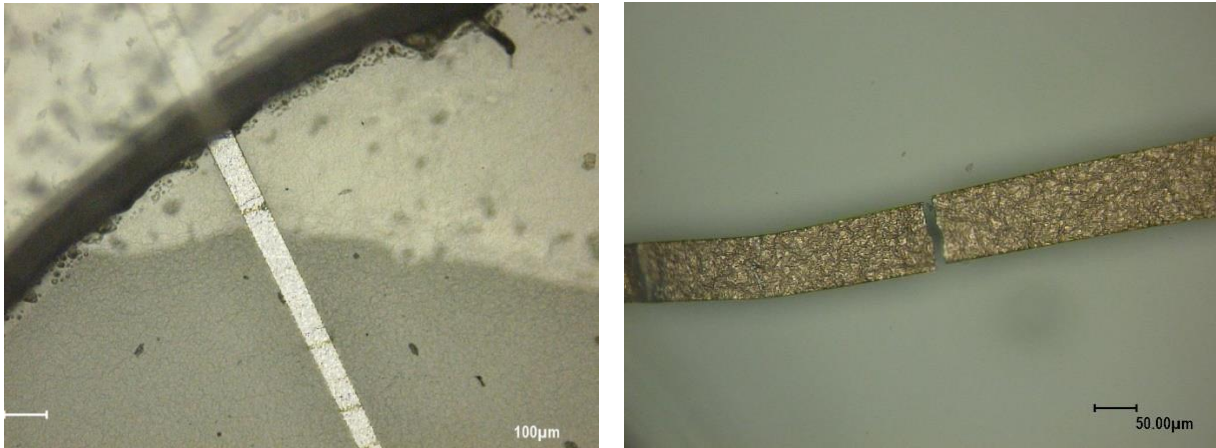


Figure 5.7: Cracks identified on aluminium traces upon optical inspection.

In general, for the principle shown in Figure 5.8, any substrate deformation might cause cracking of the traces. When aluminium traces are deposited on top of PDMS they form a uniform and uninterrupted layer on top of the substrate (Figure 5.8A). Whenever deformation happens in the substrate, for example because of a force applied, the flexible PDMS substrate bends, and the aluminium traces try to match this deformation. Nonetheless, their flexibility and mechanical properties do not match the properties of PDMS, small cracks form (Figure 5.8B), and the electrical connection is interrupted. Because of its elasticity, PDMS then returns to its original configuration: the formed cracks close and are hard to identify with visual inspections, but the trace electrically results as non-connected (Figure 5.8C).

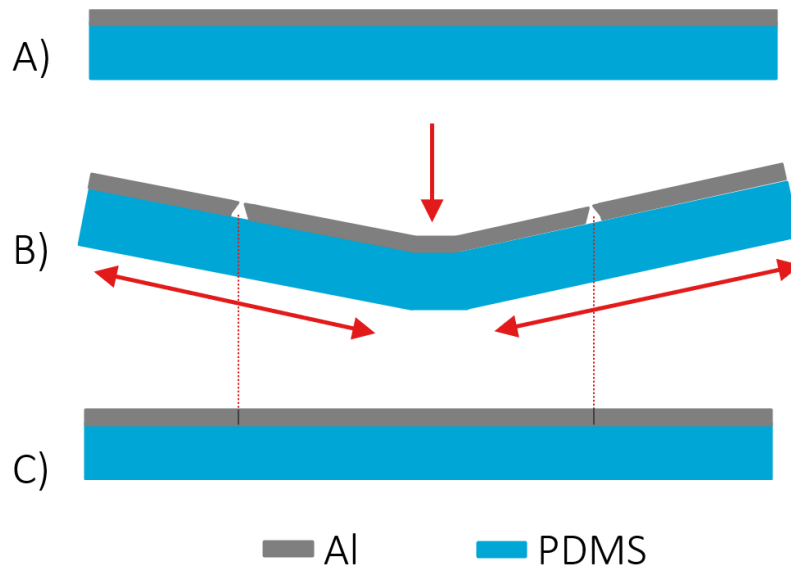


Figure 5.8: Cracking formation principle upon substrate deformation (cross-section).

This is the reason why often cracks were challenging to identify optically, and failures were identified only in the electrical behaviour of the sensors (Section 6.2). Pictures of this principle, and of these cracks only visible upon deformation of the substrate are shown in Figure 5.9.

A deeper explanation of the failures associated with every passage is given in the next paragraphs.

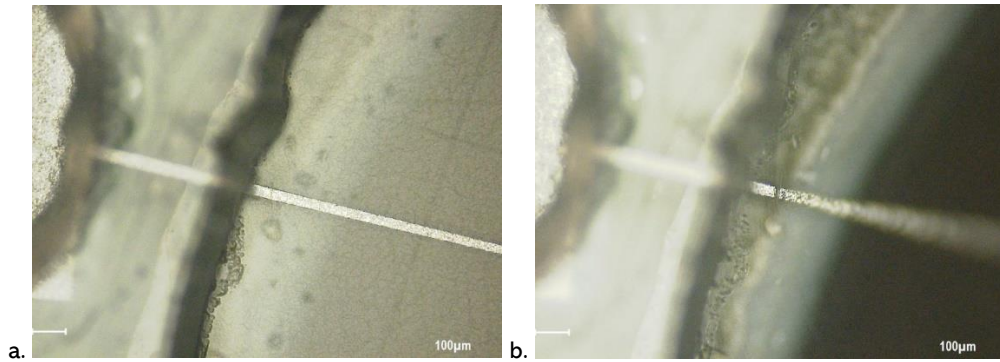


Figure 5.9: Crack formation upon substrate deformation (top view). Substrate is deformed only in (b).

5.3.1 Failures related to wire bonding

The most critical process in relation to failures of the sensors proved to be the wire bonding process. For its intrinsic principle, wire bonding is performed by applying force and ultrasonic power when the wire is in contact with the substrate it should be bonded to. Performing such a process on a flexible and elastic substrate causes variability in the process parameters, which are fundamental for the outcome of the bond. Moreover, when force is applied to the rigid gold shim on top of rigid conductive glue, something similar to the phenomenon explained in Figure 5.8 happens: the substrate is deformed below the rigid glue, but not on its side, and cracking happens at the interface. Another aspect that causes process variability is the manual dispensing of conductive glue, whose height influences the final height of the shim, which is a critical parameter for bond quality.

The main failure mode that was witnessed during this process is the creation of ring-shaped cracks in the aluminium pads, around the rigid glue droplet (Figure 5.10).

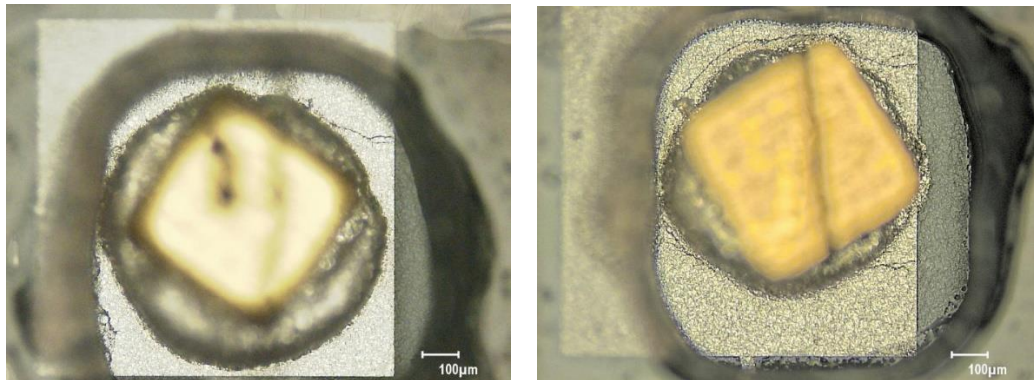


Figure 5.10: Ring-shaped cracking around gold shim after substrate deformation caused by wire bonding.

A solution to avoid this failure mode is to investigate alternative interconnecting processes that avoid the use of force or pressure, which is the critical element causing cracks.

5.3.2 Failures related to detachment from the wafer

Failures were also reported in relation to the first passage of the assembly: the detachment from the Silicon wafer on which the platforms are manufactured.

In this case, cracks formation was reported because of weak geometrical structures in the sensor design: the long and thin traces connecting the sensors to the contact pads, in proximity to these

latter structures, presented sharp corners and small widths compared to the pads themselves. Stress originating from substrate deformation during the detachment is therefore focused on these sharp corners, as highlighted in Figure 5.11.

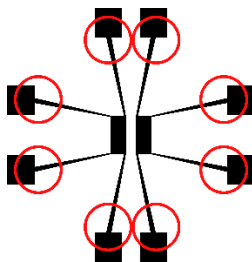


Figure 5.11: Design regions sensitive to cracks formation because of their geometry.

The result of this design is that cracks originate from these corners and propagate for the whole width of the trace, as documented in Figure 5.12.

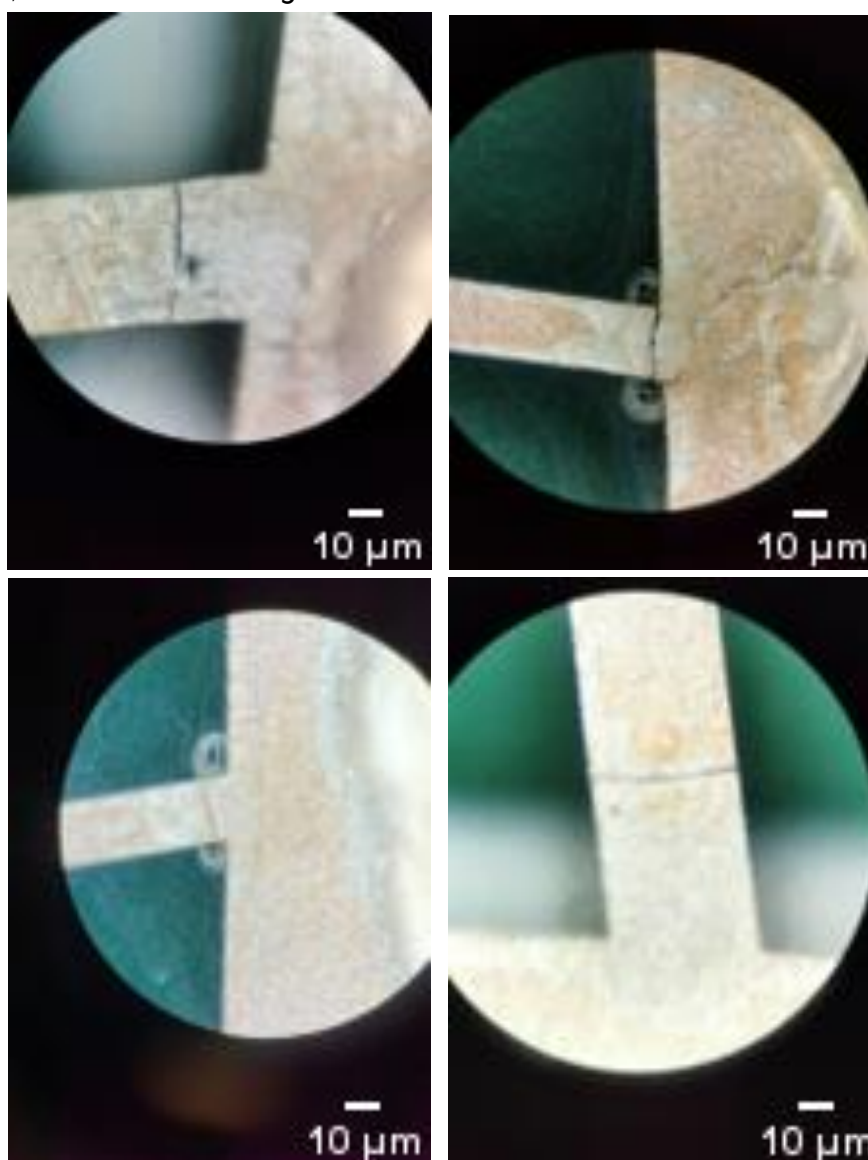


Figure 5.12: Cracking formation after detachment from Silicon wafer in correspondence with sharp corners.

The solution to this problem is to be investigated in a more careful design of the structures in the mask for photolithography, adding some wider tapering and chamfering to the abovementioned sharp corners.

5.4. Improved assembly procedure

For the reasons just shown, alternatives to this critical and unreliable assembly process were investigated. The first possibility to try to increase process reliability was to encapsulate the aluminium traces between two layers. Pressure Sensitive Adhesive (PSA) foils were cut in special shapes and were used in the assembly process. In detail, a first layer was placed on the PCB and served as a substitute for the PDMS droplet used to glue the platforms to the substrate. The function of this layer is to ensure uniform and flat adhesion between the PCB and the PDMS substrate of the platform. After positioning the platform on top of this PSA layer, a second PSA layer with small openings in correspondence with the contact pads and with a bigger opening in correspondence with where the well needs to be placed is attached. The function of this second layer on top of the traces is to encapsulate them, protecting them from excessive stresses and making them less fragile. The assembly process is then continued as described previously, with the placement of gold shims and the performing of the bonds. A cross-section of the new process at its final stage is shown in Figure 5.13. As will be shown in Section 6.3, the protection provided by the second PSA layer to the aluminium traces proved to increase the reliability of the assembly and allowed the fabrication of electrically and mechanically intact sensors.

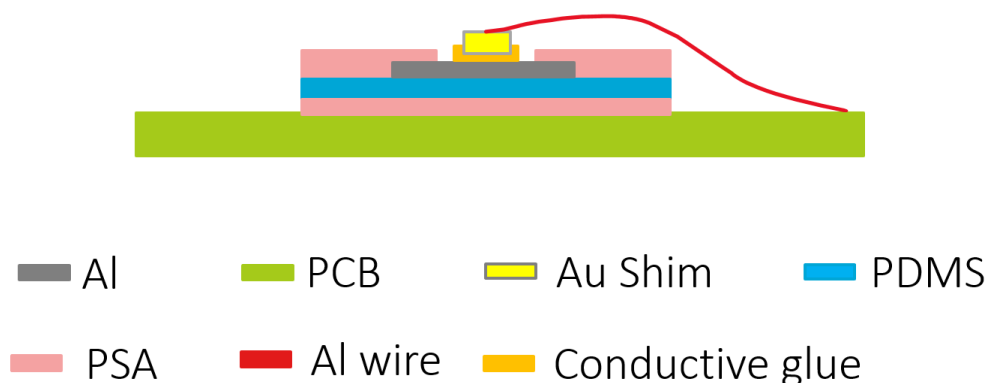


Figure 5.13: Cross section after the final stage of the improved assembly process.

Since the most critical aspect of the assembly shown in Section 5.2 was related to the wire bonding process, a manual connection was performed: one droplet of conductive glue was placed on the aluminium pad of the sensor and one on the gold pad of the PCB. A short and thin aluminium wire was then stuck inside the droplets before curing the glue. A pressureless connection method was thus investigated, whose result can be seen in Figure 5.14. This method did not provide the expected result, and electrical failures were reported. Nonetheless, visual inspection did not highlight cracking in the substrate, so it can be interesting to perform other attempts in the future.



Figure 5.14: Investigated alternative to ultrasonic wire bonding.

5.5. Final assembly steps

When the platform is glued and electrically connected to the PCB, as explained before, it does not have the top PDMS layer with pillars. If dynamic measurements of the sensors need to be performed, the pillars need to be placed on top of the sensors as was explained in Section 2.2.2. This process is done by dispensing a small drop of uncured PDMS on top of the sensors, placing the thin cured PDMS layer with pillars and well on its top, and making it slide on the uncured PDMS to reach a good alignment between sensors and pillars. With this process, therefore, manual alignment is performed: even if good precision can be reached, the alignment will not be perfect and might lead to behaviour slightly different from the simulations.

In Figure 5.15, a picture of the assembly up to this point is shown. In this specific sample, the well was partially cut for reasons that will be explained in Section 6.5.

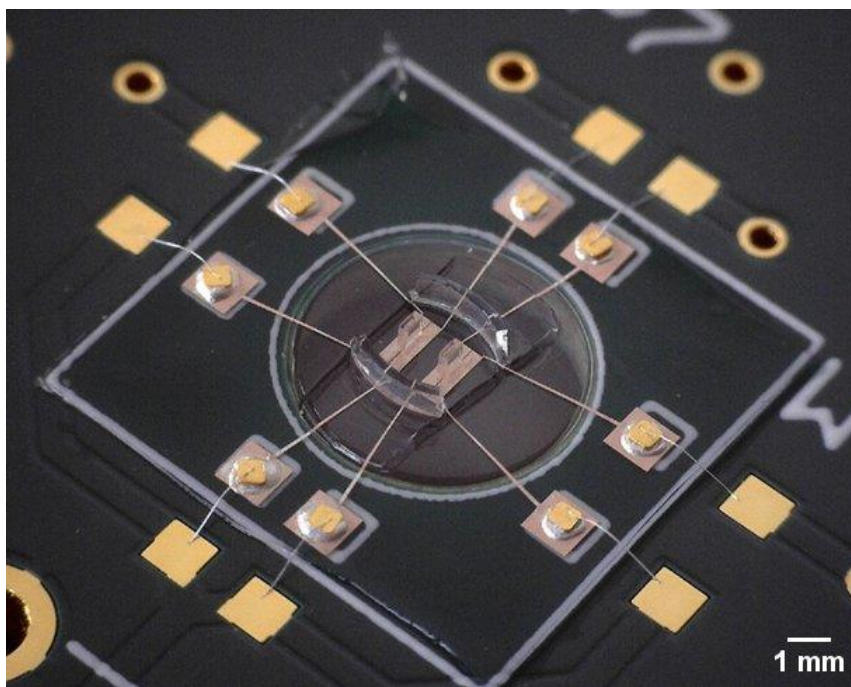


Figure 5.15: Application of thin layer of PDMS with pillars and well on top of aluminium sensors.

After this process, the last step needs to be performed before cell culture: the gluing of a bigger biocompatible acrylic well around the PDMS well, to host cell culture medium. Small quantities of uncured PDMS are poured on the outer walls of this well: this PDMS will slide down toward the base

of the pillars and will be cured to guarantee the sealing of the well. When sliding on the base of the well, uncured PDMS also spreads in the surrounding area covering contact pads, shims, and wire bonds, thus providing mechanical protection and preventing possible damages or detachments. The final assembly is shown in Figure 5.16.

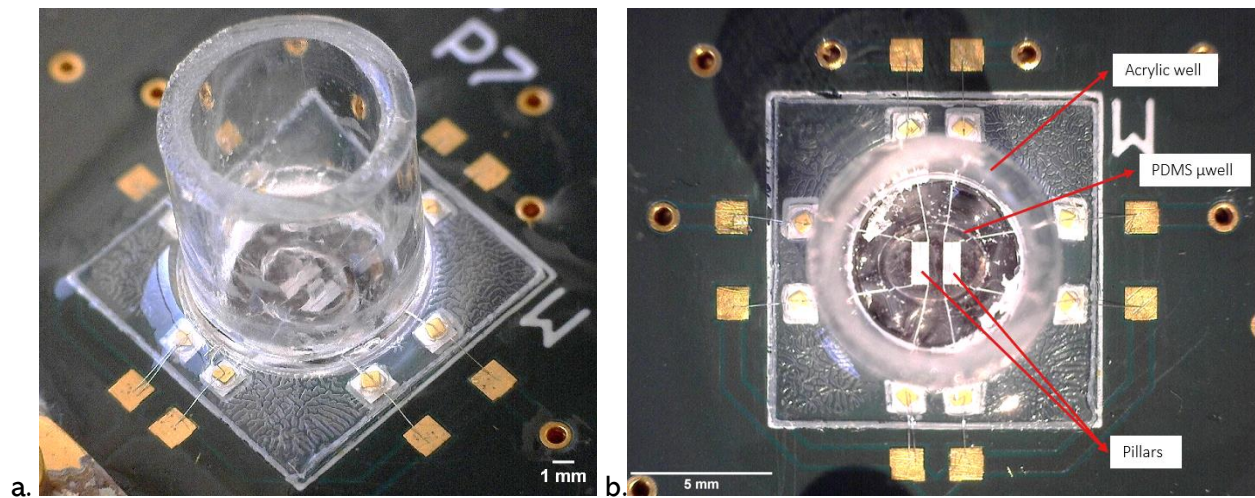


Figure 5.16: Attachment of second acrylic well side view (a.) and top view (b).

5.6. Interconnects and external disturbances

Once the assembly of the platforms on the PCB is performed, electrical connection of the PCB to the readout board needs to be made. As was seen in Section 4.3.2, non-shielded wires are not suitable for the readout of capacitance in the needed range, because of the high coupling with external disturbances and parasitic capacitance coming from the environment. For this reason, two coaxial cables (SMB) were used: one for excitation and one for readout.

Even shielded coaxial cables proved to pick up a small quantity of disturbances from the measurement environment, and measurement showed a decrease in the effective resolution of the measurement system of almost one bit when the coaxial cables were connected to the system. These disturbances coupled to the system likely in the only part where the signal is not shielded, that is on the lead of the through hole connector soldered on the board. For this reason, in a successive redesign of the board, SMD connectors have been chosen (as will be shown in Figure 6.18).

Moreover, as PCB traces proved to generate offsets caused by parasitic capacitance, the same happened to cable connection: it was proved that different cables with different lengths contributed differently to the measurements, adding a different offset. This is the reason why, before every measurement, the system needs to be calibrated to take into account all these offsets generated by the interconnects.

A final attention for the removal of external disturbances and parasitic coupling was to shield not only the interconnects, but also the readout board. This was done by placing the readout in an aluminium box like the one that will be shown in Figure 6.3, which was then connected to the ground. The use of this box proved to improve the noise performance of the board only slightly, but the comparison between readouts performed inside and outside the box showed a small and constant difference in the measurement, to be identified as an offset generated by parasitic couplings when the board is not inside the box. This capacitance coupling is prevented by the shielding action of the metal box.

Measurements and system characterization

Once the readout is chosen, the sensors are assembled on the PCB, and the connections are made, it is possible to perform measurements and characterization of the system and of the sensors. All the measurements and experiments performed in this direction are explained in this chapter.

Static measurements, which means measurements performed when no force is applied to the pillars and the sensors behave as a constant capacitance, were performed immediately after the fabrication and before any assembly passage, when the sensors are still on the silicon wafer.

As shown in Chapter 5.3, the first developed assembly procedure led to failures in the mechanical domain which were identified also in the electrical domain, influencing the measurements. Improved reliability of the process was reached with a new assembly, and new measurements were performed.

Dynamic behaviour of the sensors relates to the response that the sensor has to the displacement of the pillars. At first, manual mechanical stimulation was applied to the pillars to prove the concept of the measurement. Nanoindentation test was then performed by applying controlled force to the pillars. The response of the sensors was documented, and their responsivity was characterized.

The first attempt towards the final test was done by culturing cells around the pillars, to measure sensors' dynamics in a biological environment.

6.1. Base Capacitance

The first test to be performed concerning the static behaviour of the sensors is the measurement of their base capacitance. To ensure the quality of the fabrication process and to create statistics about the base capacitance value, measurements were performed immediately after fabrication on all the sensors fabricated on the wafer.

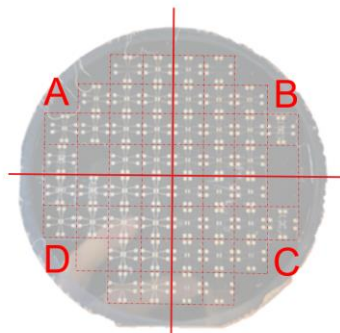


Figure 6.1: Location of each different type of sensor in each quadrant.

Because of the mask design, each quadrant of the wafer contains one specific type of sensor (A, B, C, or D) as shown in Figure 6.1. For each quadrant, twelve platforms are patterned, with four sensors for each platform, for a total of 48 sensors per type. In total, therefore, 192 measurements were performed: since those were done before the assembly steps, a suitable method was found in the use of an Agilent 4294A Precision Impedance Analyzer. This instrument was used in connection to an electromagnetically shielded probe station (Cascade Microtech Summit 12k) and needles were used to create electrical contact between the instrumentation and the contact pads of the sensors.

4294A parameters for measurement are selected using IC-CAP software, which allowed the performance of C-V measurements with a sweep in the voltage from 0V to 5V. Since the base capacitance of the sensors is expected (and proven) to be independent of the excitation voltage in the abovementioned range, those measurements can be regarded as measurements of capacitance vs. time. The frequency of the excitation signal was selected to be 32 kHz to match the excitation frequency of the AD7746 board, but measurements at lower and higher frequencies were performed and provided highly comparable results.

C-V measurements were performed for each of the 192 sensors on the wafer, and the results were grouped for sensor type. Since the sensors measured in this stage do not have PDMS layer on top (see Sections 2.2.2 and 5.5), measurements must be compared to the results obtained from new calculations performed at the end of Section 2.2.3. According to those calculations, the expected base capacitance for each of the sensors is reported in Table 6.1, together with the average measurement and the error between them.

Table 6.1: Expected and measured value for base capacitance when platforms are on the wafer.

Sensor type	A	B	C	D
Expected value in fF	374	279	497	231
Average measured value in fF	300	250	450	180
Relative error in %	19.79	10.39	9.46	22.17

In the case of sensors of type A, out of 48 sensors measured, 39 provided results in agreement between them (and with the expected value), with an average of 300fF of measured base capacitance. Some samples provided a capacitance close to 0fF, and some others showed a higher capacitance compared to the expected value. Deviation of those measurements from the expected result could often be explained with visual inspection of the fabricated wafer, on which sensors with broken traces were identified and/or unexpected aluminium lines survived to the etching process influenced the geometry and therefore the behaviour of the structures.

For sensor B the average result of 42 sensors was 250fF, again in agreement with the expected results.

Sensors of type C were measured, and 30 of them behaved as expected, providing a base capacitance of 450fF. The small number of sensors working as expected for this specific type, and the many samples providing a low capacitance (close to 0fF) can be explained by the extreme geometry of the sensor: thin lines and thin gaps are easily damaged and the fabrication itself proved to be more challenging.

Sensors of type D provided an average of 180fF, again in agreement with calculations and only a few damaged sensors were measured.

Histograms related to the number of measurements in certain intervals are shown for each type of sensor in Figure 6.2 to prove the statistical quality of the measurements.

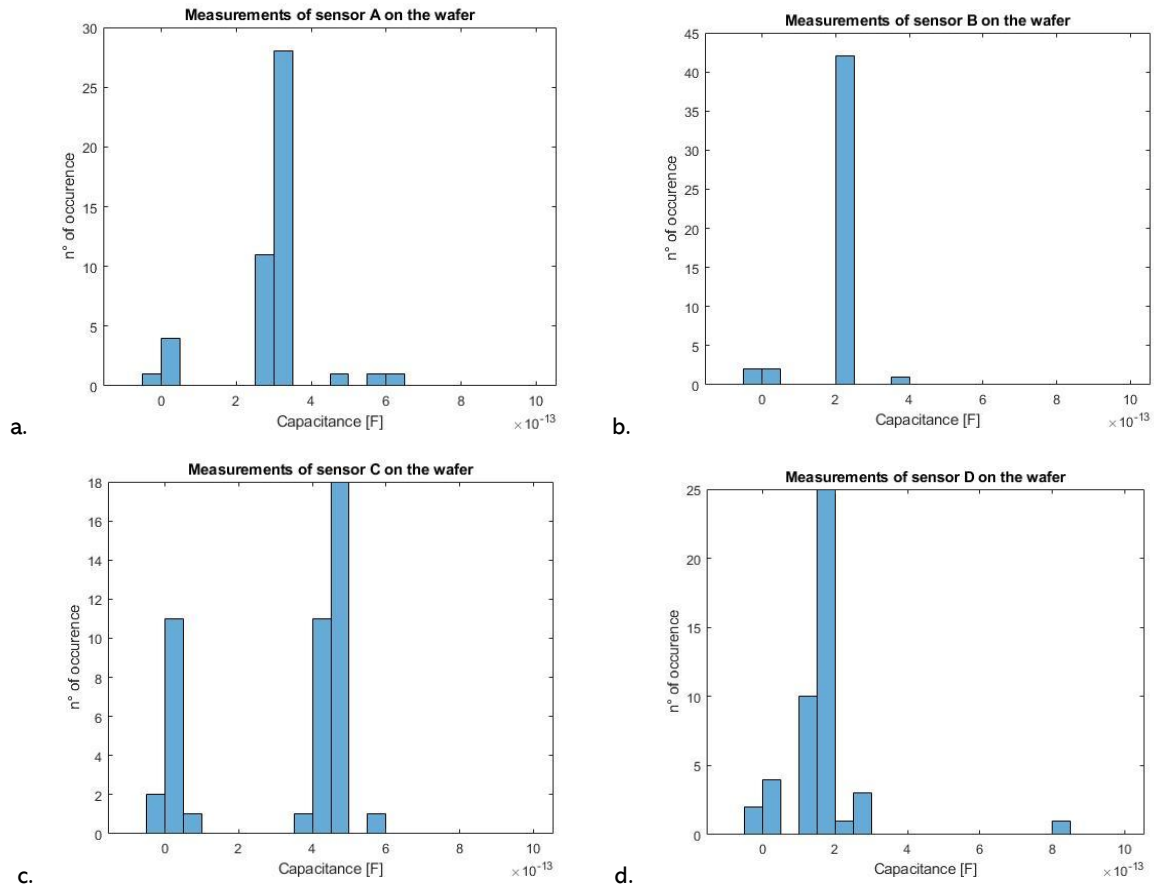


Figure 6.2: Base capacitance measurements when platforms are on the wafer for sensors A (a), B (b), C (c), and D (d).

When analysing the data in comparison to the expected value, a general trend that can be highlighted is that the measurements are in agreement but slightly smaller than the result obtained with calculations. A plausible reason can be found in the fact that the etching process can cause some imprecisions. Even if measurements were performed as shown in Section 2.3, traces might be in general slightly smaller than expected, thus providing bigger gaps between one trace and the other and causing the base capacitance to be slightly smaller.

6.2. Electrical failure modes

In Section 5.3 it was shown how the first developed assembly procedure gave origin to mechanical failures in the form of cracks in the aluminium connections. These failures were identified mainly in relation to the electrical behaviour of the sensors because, as explained, cracks are often hard to identify because of the elasticity of the substrate.

Electrical failures were discovered immediately after the first attempt to assemble one platform on the PCB: measurements were performed to verify the quality of the process after the assembly process using the AD7746 board, simply connected via coaxial cables to the PCB with sensors, as shown in Figure 6.3.



Figure 6.3: Measurement setup and connection for AD7746.

These measurements provided an extremely low base capacitance result, which was around Off. To exclude the possibility of errors in AD7746 readout, the same measurement was performed with the 4294A impedance analyser, and provided a low capacitance value as well, as seen in Figure 6.4.

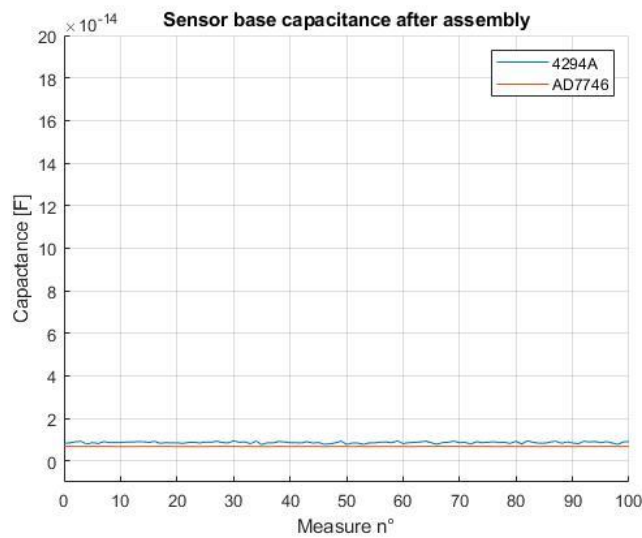


Figure 6.4: Base capacitance measurements after assembly, performed with different instruments.

Visual inspection of the samples was performed, and the failures discussed in Section 5.3 were identified. It was therefore possible to create a correlation between the formation of crack and the lowering in the base capacitance of the sensors to values close to Off.

The same assembly process was performed multiple times, and the same behaviour was identified: base capacitance of the sensors was comparable to the expected value before the assembly, but the base capacitance value lowered dramatically to reach values of a few fF after the assembly. Associated with this lowering, the formation of cracks in the aluminium traces was often identified using visual inspection.

The possibility that these electrical failures were generated during one of the multiple passages of the assembly process was investigated. Measurements were performed after each step of the assembly, to identify if criticalities arose during a specific one.

Before wire bonding, the sensors are not electrically connected to the PCB, therefore probe station connected to 4294A was used for all the measurements before that step, and both AD7746 and 4294A were used to verify the final measurement after wire bonding.

As an example, the base capacitance measurement of one platform (four sensors of type D) after every step of the assembly process is shown in Figure 6.5.

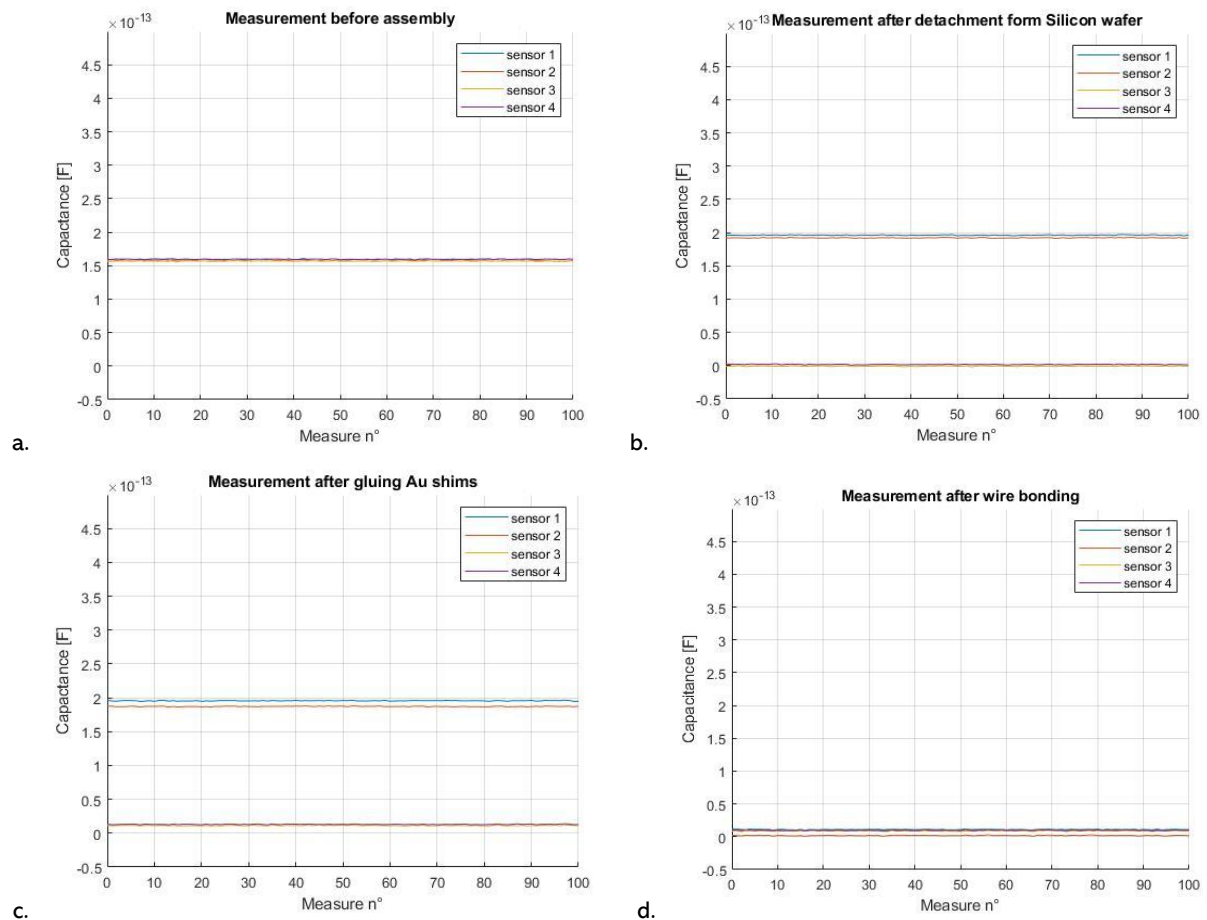


Figure 6.5: Base capacitance measurement of four different sensors at different stages of the assembly process

The measurement shown in Figure 6.5a highlights how all four sensors exhibit the expected behaviour before the assembly passages. After the first assembly step, related to the detachment of the platform from the silicon substrate and its placement on the PCB, already two sensors witnessed a drop in base capacitance (Figure 6.5b), associated with crack formation. The second assembly passage relates to the gluing of gold shims on top of aluminium pads and was not proven to be critical for failures, as shown in Figure 6.5c, in which no differences in the behaviour of the base capacitance are identified in comparison to the previous step. Wire bonding criticalities in terms of cracks formation reflected in the electrical behaviour of the sensors: as shown in Figure 6.5d after the wire bonding passage, two more sensors of the platform witnessed a dramatic decrease in base capacitance, leading to none of the four sensors working as expected after the assembly process.

These measurements are exemplifications of what happened during the attempts to fabricate multiple platforms: most of the failures were identified in relation to the detachment from silicon and to the wire bonding, which were highlighted as the two most critical aspects.

The conclusion that must be derived is that failures happen during the assembly steps, and these failures were documented both in the mechanical domain (visual inspection) and in the electrical domain (base capacitance measurements).

A final remark worth mentioning is related to the importance of ground planes in the PCB which was already explained in Section 5.1. Measured parasitic capacitance when the planes are not grounded can be misinterpreted as the expected base capacitance of the sensors, as both are in the

same range. The ground connection is provided to the PCBs through the coaxial connectors, but if coaxial connectors are not used and the measurement is done using the probe station, the result is that planes are not grounded. If wire bonding is performed and sensors are measured using the probe station, the readout would provide the measurement of the parasitic capacitance of the PCB added to the base capacitance of the sensors. Since we just showed that the base capacitance of the sensors dropped to a value around 0fF, the readout would only provide the value of the parasitic capacitance (200fF-300fF) which is in the same range as the expected value for the base capacitance (Figure 6.6). This might bring to the wrong conclusion that the sensors are behaving as expected, but accurate measurements can be performed only when the planes are grounded so that the effect of parasitic coupling in PCB traces is attenuated.

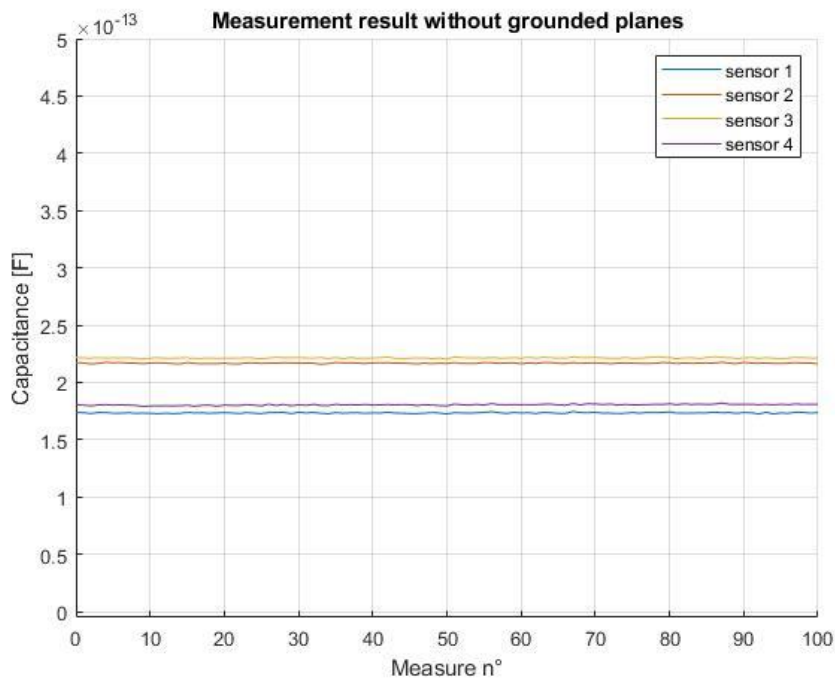


Figure 6.6: When planes are not grounded, measurement reflects parasitic of PCB traces (see Figure 5.3a).

6.3. Results after improved assembly

As explained in Section 5.4, alternatives to the original assembly process were investigated and attempted.

In particular, encapsulation of aluminium traces between two PSA layers allowed the production of some sensors that did not fail during the wire bonding, maintaining the expected base capacitance even after that passage. This never happened with the previous assembly strategy, and measurements performed after this new assembly technique showed that four sensors between the ones that have been assembled maintained a base capacitance in agreement with the calculations performed. This result provided a proof-of-concept for the whole assembly process and showed that, with improvements, wire bonding can still be used.

After the critical step related to wire bonding, two more passages need to be performed as explained in Section 5.5. The next step in the assembly process regards the gluing of this thin top PDMS layer above the sensors. Unexpectedly, this process also gave origin to three failures that could not be identified via visual inspection but that caused the base capacitance of three of the four

sensors to drop down to low values around 0fF . The only sensor that maintained the expected base capacitance was a sensor of type A, which as expected and as explained in Section 2.2.3 registered an increase in capacitance of around 1.5 times, going from a base capacitance of around 380fF (as calculated for the case of sensors without top PDMS layer) to a value of 570fF , that is in agreement with the calculation in the case of sensors completely encapsulated between two PDMS layers. Figure 6.7 shows the result of this measurement.

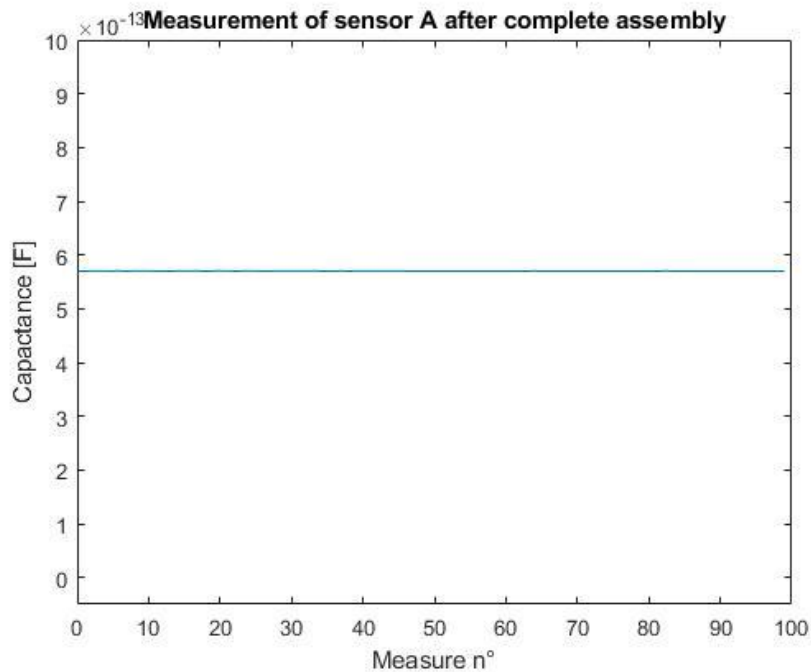


Figure 6.7: Base capacitance measurements of sensor of type A after the assembly procedure. Result is in agreement with simulations reported in Table 2.2.

The last step in the assembly, as explained in Section 5.5, is to glue a bigger acrylic well around the PDMS microwell to better confine the nutrient medium needed for cell culture. This well needs to be glued on top of the substrate and tests to check leakage need to be performed. These two passages are also critical, in that they cause a deflection in the PDMS substrate that might cause cracking. After this ultimate step, even the last sensor that showed compliant behaviour compared to the expectation, electrically failed and witnessed a drop in capacitance.

So, even if the reliability of the process was increased in relation to the wire bonding process (it allowed the fabrication of four sensors that maintained the expected behaviour after that passage), the whole assembly still revealed to be critical and the last two steps caused electrical failures in all the samples that were measured. This shows how the design and the assembly process need to be further improved to guarantee a procedure that provides good yield and few failures to be completed.

Despite this need, with the improved assembly technique, some of the sensors exhibited just a relatively small decrease in the base capacitance, which did not drop to 0fF but remained at higher values around a few tens of fF , up to one hundred fF . These partially satisfactory results need to be better investigated, and the motivation leading to this partial failure needs to be more precisely assessed before some conclusion can be drawn.

6.4. Manual pillar displacement

Even though none of the assembled sensors maintained the expected base capacitance value until the end of the assembly process, it is still interesting – if possible – to investigate the dynamic behaviour of the sensors. The first thing to be understood is whether the electrical failure seen until this point influenced the dynamic behaviour of the sensors, such as their responsivity, or if this aspect was maintained regardless of the wrong value in base capacitance, and sensors could still be used in the application they were developed for.

With this objective, manual displacement was induced in the pillars using a small plastic tip, while capacitance recording was performed. This preliminary test was done with one of the sensors which, during the assembly process, registered a drop in the base capacitance to a value close to Off, so to verify the responsivity of the sensor separating it from its base capacitance behaviour.

The test aimed to apply a manual (and consequently uncontrolled) mechanical stimulation to one of the pillars. Similarly to the expected behaviour in the final application, this movement of the pillar is expected to cause a deformation in the substrate, which in turn causes a change in the capacitance of the sensor integrated into the PDMS substrate.

In Figure 6.8 a screenshot of the control screen during the experiment shows on the left a microscope image of the platform to help manual displacement of the pillar and on the right the AD7746 software interface which serves as a control screen for the electrical behaviour of the sensor measured.

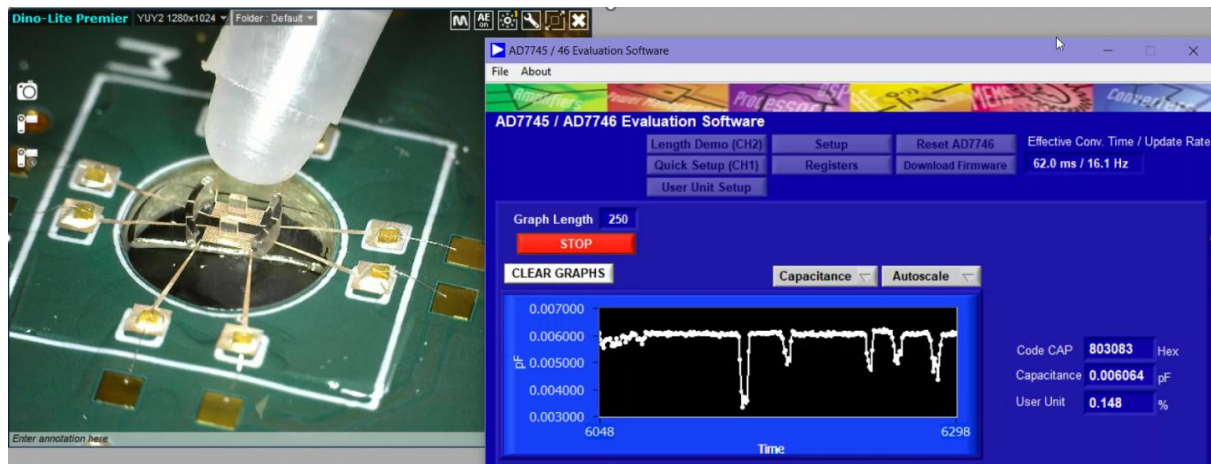


Figure 6.8: User interface for dynamic measurements of the sensors (recording available at https://drive.google.com/drive/folders/1UK4rp9EZsp_MRE_byC55ighvRSxATEwC?usp=sharing).

A non-conductive plastic tip was used to perform this pillar displacement, in order for it to not interfere with the electric field generated by the co-planar traces of the sensors, and therefore with their capacitance. As can be seen from the graph on the right a reaction can be highlighted in the capacitance behaviour. This change in capacitance was reproducible and happened every time that the pillar was stimulated, thus meaning that the sensors integrated into the substrate, despite the failures reported in their static behaviour, were still sensitive to some physical stimulation.

Obviously, this first rough test served just as a proof-of-concept for the sensor working principle: since the force applied to the pillar and consequently its displacement could not be properly controlled, it was impossible to characterize the sensor and to create a relation between the force applied and the capacitance change. Nonetheless, this test verified that sensors were still responsive

despite the failures highlighted in the previous Sections, and that further and more precise tests to create a capacitance-force relation could be performed as next steps.

6.5. Nanoindentation

A more precise test to characterise the sensors' dynamic behaviour can be conducted using the FemtoTools Nanomechanical Testing System FT-NMT03. This is a nanorobotic system for direct and accurate measurement of the mechanical properties of nanostructures [64]. This instrument uses a silicon microtip featured with a micro-force sensor which can measure the force applied by the tip on different structures. Moreover, the stage motion is controlled, so that the displacement of the tip can be set as well. Cyclic movements can be programmed to apply precise force patterns to the structures such as compression, tension, and displacements. Figure 6.9 shows the appearance of the instrument: the silicon tip is clamped in a moving holder, which can be positioned and controlled to apply force to the sample, which needs to be placed on top of a small cylindrical chuck. The holder and the tip are bent to form an angle of 15° with the horizontal plane, to better access the structures of the samples.



Figure 6.9: FT-NMT03 (Derived from [64]).

Since this instrument allows the control of the force applied to the sample and the tracking of the associated displacement, it is optimal to create an applied force-displacement curve: in other terms, the instrument allows precise calculation of the stiffness of the microstructure. In our application, applying a certain force to the pillars when the sensors are connected to the readout allows the creation of a capacitance change vs. applied force curve, which relates to the responsivity of the sensor and allows its final characterization.

The setup for this experiment is shown in Figure 6.10: the sample (PCB with platform assembled) is placed on the chuck of the FT-NMT03 (red rectangle). The device is controlled and monitored using a PC that allows the programming of force and displacement applied by the microtip. Sensors are electrically connected to the AD7746 readout contained in the metal box, which is in turn connected to a laptop running the AD7746 software for real-time monitoring of the sensor behaviour. A zoomed-in picture of the area contained in the red rectangle is provided in Figure 6.11.

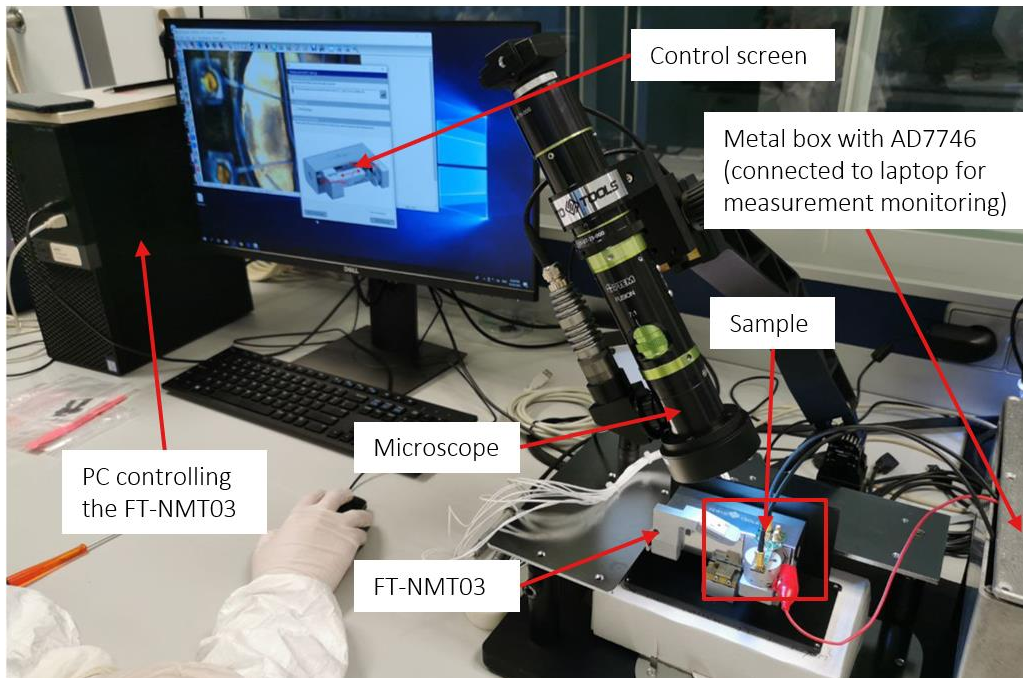


Figure 6.10: Setup for dynamic measurements of sensors using FT-NMT03 and AD7746.

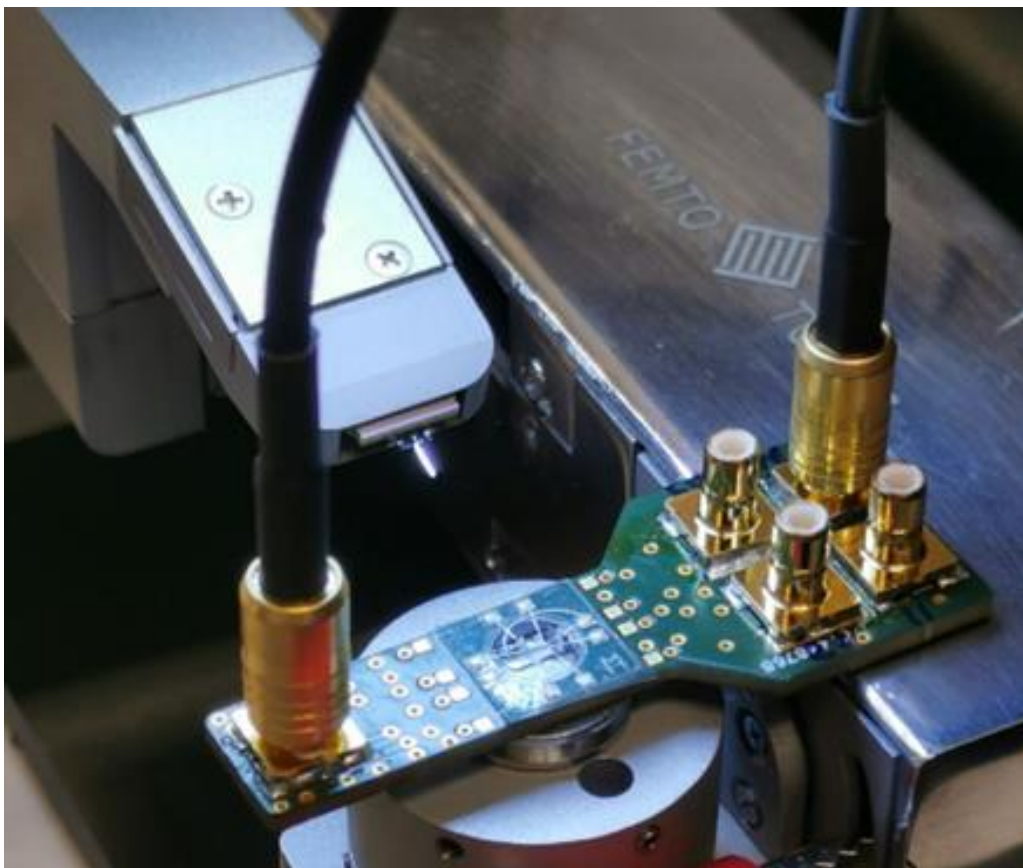


Figure 6.11: Magnification of the red square of Figure 6.10, showing PCB placement in the setup and tip for nanoindentation.

For this specific experiment, special platforms with openings in the well were produced (Figure 6.12) to allow pillars to be reachable by the tip to perform mechanical indentation.

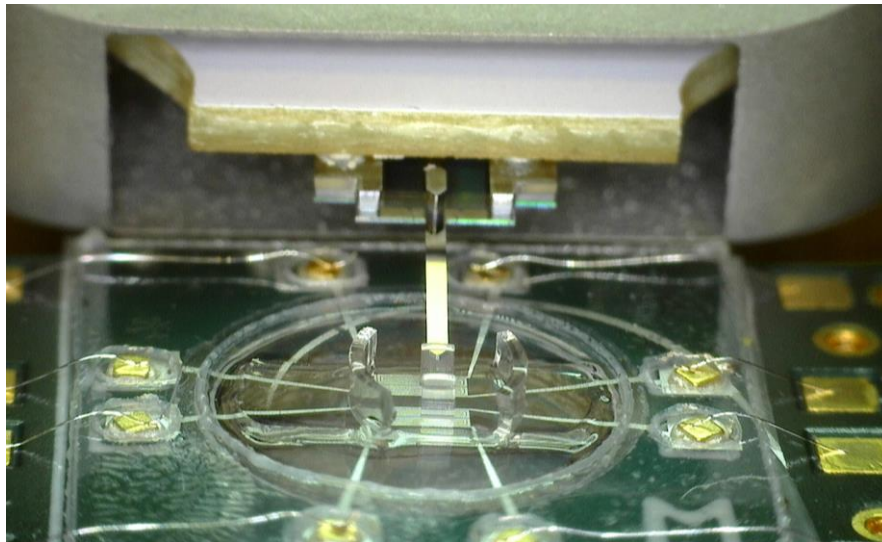


Figure 6.12: Magnified image of silicon tip in contact with EHT pillar to apply controlled force on it (wells are cut).

The decision taken, as in the case of the manual stimulation of the pillar in the previous section, was to perform the test with the only available sensors, so with those who did not maintain the expected value of base capacitance throughout the entire assembly process. In detail, the sensor that was measured was a sensor of type D and showed a base capacitance of around 95fF.

Measurements were performed by applying controlled force on the pillars, to induce pillar deflection, substrate deformation, and consequently capacitance change in the sensor. This change could be monitored in real-time using the AD7746 evaluation software. A screenshot of the control screen is shown in Figure 6.13.

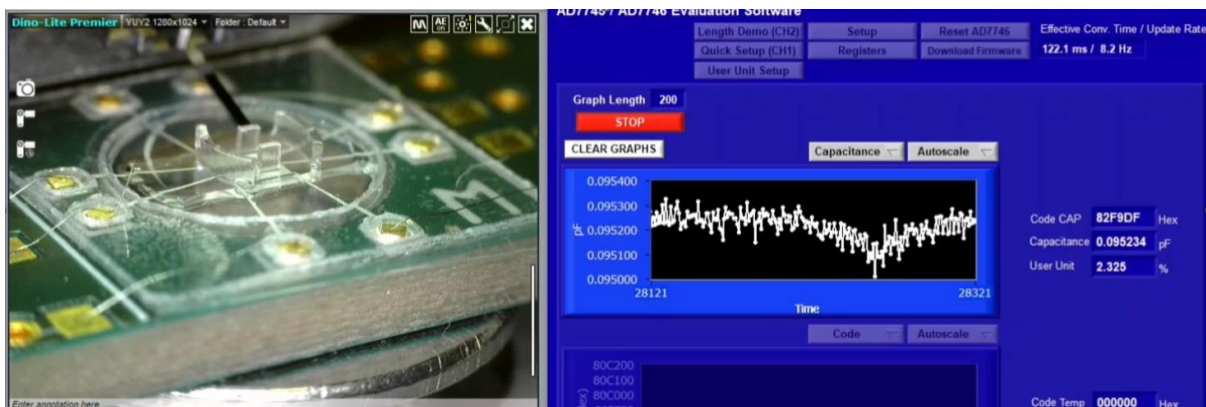


Figure 6.13: User interface during nanoindentation experiment showing change in capacitance as a result of pillar displacement (recording available at https://drive.google.com/drive/folders/1UK4rp9EZsp_MRE_byC55ighvRSxATEwC?usp=sharing).

As can be seen from the plot on the right, there is a reaction in sensor capacitance when the pillar is displaced by the silicon tip of the nanoindenter. The plot has been saved, exported, and analysed with MATLAB to allow signal processing and evaluations of the signal. An example of the obtained curve is shown in Figure 6.14. From this figure, it can be seen how the noise level is remarkably high compared to the signal level, but this extremely low SNR does not prevent the identification of some underlying signal. Signal processing needs to be used to obtain a smooth signal out of the noisy recording, and to do that MATLAB function `smoothdata` was used.

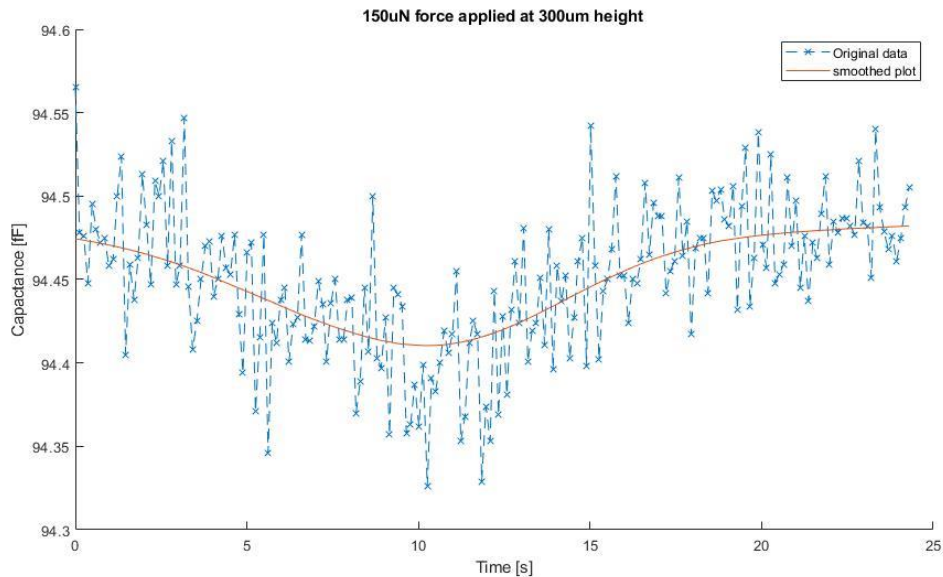


Figure 6.14: Noisy signal and smoothed curve using MATLAB smoothdata function.

Multiple parameters for this smoothdata function were investigated, and a short evaluation of that aspect and of how the smoothing influences the result of the measurement is provided in Appendix F.

After this smoothing process, from the smoothed signal it is possible to extract the change in capacitance between the moment on which no force is applied to the pillars and the moment on which the determined force is used for pillar displacement. Multiple measurements have been performed changing two variables: the force applied to the pillar and the height at which this force is applied with respect to the base of the pillar. Five distinct levels of force in the interval between 100 μN and 300 μN (comparable to the expected force applied by the cultured cardiac tissues) were investigated. Because of the 15° angle formed by the tip with the horizontal plane, the force applied perpendicularly to the pillar resulted to be $\cos(15^\circ) = 0.9659$ times the one set in the instrument, going from 96.59 μN to 289.77 μN . Seven different application points from 250 μm from the substrate to 550 μm from the substrate were studied as well. Differences in capacitance (ΔC) in these cases were extracted, and the results obtained are plotted three-dimensionally in Figure 6.15.

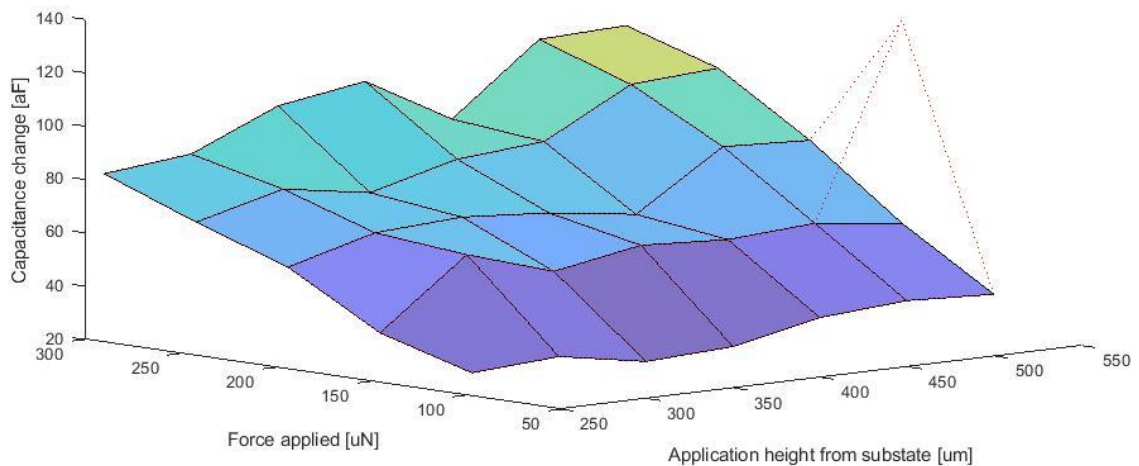


Figure 6.15: Change in sensor capacitance as a function of force applied and application height.

One outlier (dotted line in Figure 6.15-6.16-6.17), possibly originating from errors in the measurement procedure or in the force control of the system, was removed from the graphs. All the other points show trends that might be better investigated by analysing the two axes individually.

If we consider the ΔC as a function of the application height of the force (Figure 6.16) we obtain five curves, each corresponding to a certain force applied. In all of them, we can find a very slight dependency of the ΔC on the application point of the force: the deformation of the substrate is slightly higher for higher application points, probably because of the bigger torque applied to the substrate.

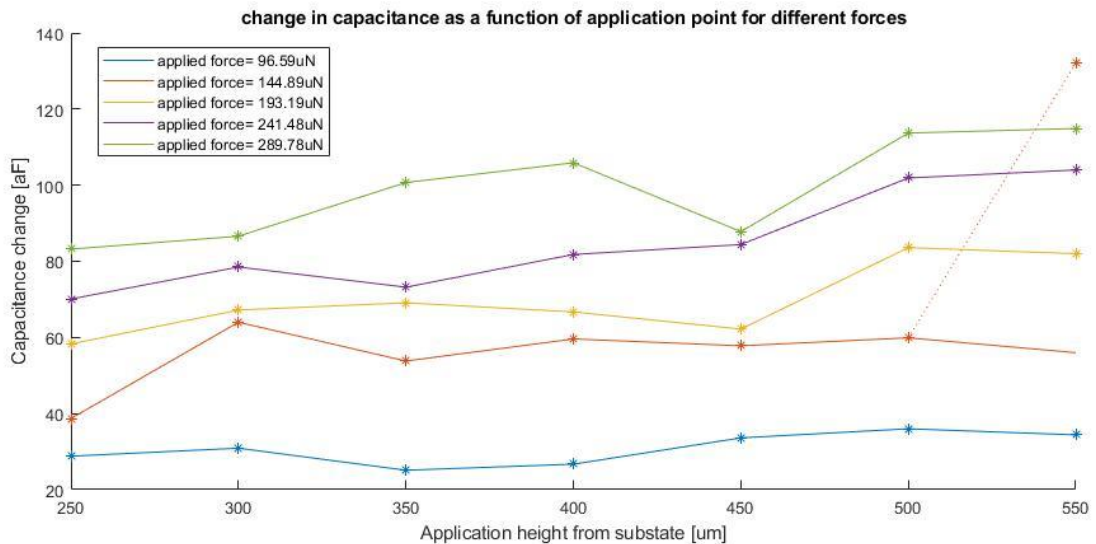


Figure 6.16: Change in sensor capacitance as a function of application height

The most interesting result is anyway obtained by plotting ΔC as a function of the force magnitude (Figure 6.17), which is the plot that relates to the responsivity of the sensor. As can be seen, disregarding the already mentioned outlier, all the measurement points show a clear dependency of the change in capacitance on the force applied, in all the seven curves obtained (each corresponding to a specific application point).

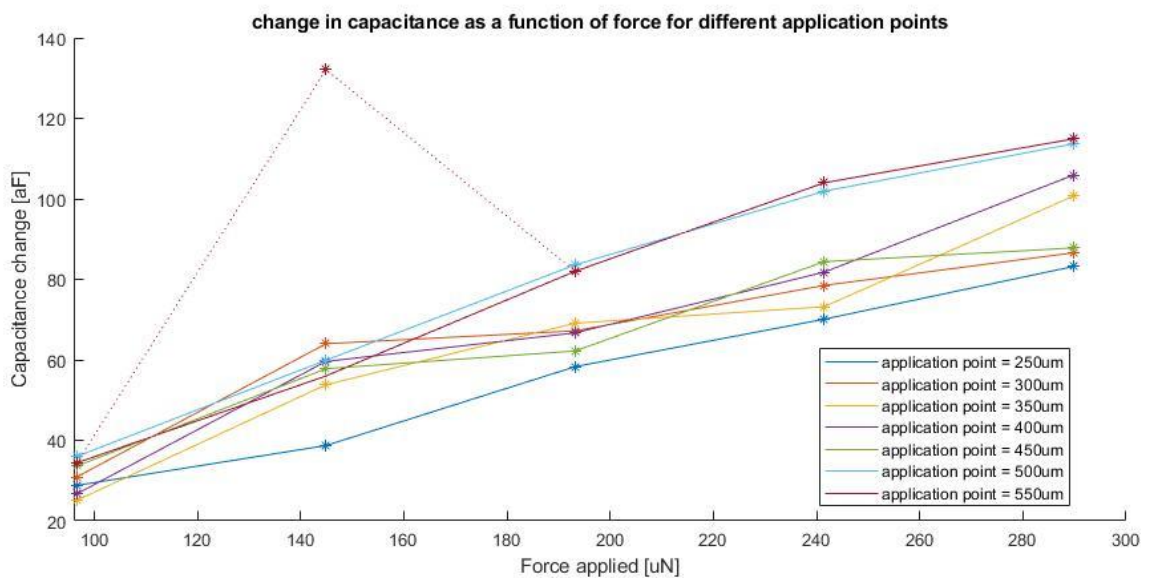


Figure 6.17: Change in capacitance as a function of force applied

ΔC is therefore proved to be proportional to the force applied. The magnitude of this dependency (responsivity) is obtained by calculating the slope of the obtained curves: these calculations for the seven samples provide values that are between 0.42 fF/ μN and 0.28 fF/ μN (assuming linear dependency). Comparing those values to the simulations of Table 2.2, it can be seen that the results are in good agreement with the expectations. Slightly smaller values can be explained with the manual alignment of the pillars, which does not provide precise positioning of sensors in the location where substrate deformation is maximal.

6.5.1 Discussion of the results

The positive result just shown is not and shall not be regarded as flawless. Precautions need to be taken when drawing conclusions, and those are motivated by five main criticalities highlighted:

- The results shown relate to the analysis of a single sensor. To verify those results and to create statistics multiple sensors must be characterised and measured.
- The single sensor on which these experiments were conducted, moreover, was one of the sensors that faced a drop in the base capacitance during the assembly process. Measurements must be repeated using sensors that maintain the expected behaviour throughout the whole assembly process, and a comparison with sensors that faced base capacitance failures should be performed to investigate the possible correlation between static and dynamic behaviour of the sensor.
- Measurements performed proved to be extremely noisy and SNR was extremely low. This was related to the fact that the setup proved to have problematic aspects, especially in relation to noise in the measurement environment. First experiments were attempted using the PCB design of Figure 5.2, which is also reported in Figure 6.18a. When the board was placed on the chuck and the tip was moved closer to the pillar to perform indentation, the noise level on the board increased significantly, to a level that did not allow measurement of slight changes in capacitance. The assumption was that the holder of the tip, which contains the electronics associated with the force sensors of the tip, moving on top of the board caused disturbances that were absorbed by the PCB itself. Therefore, a second version of the PCB was designed to prevent the holder from moving on top of the PCB: the platform was cut in half and positioned on the edge of the PCB so that the holder of the tip does not need to move on top of the PCB (Figure 6.18b). This solution did not solve the noise problem, since it was later discovered that the whole measurement environment was noisy, and just placing the PCB on top of the chuck increased the noise detected by the readout. A final redesign was performed, using SMD connectors to reduce couplings with the unshielded parts of the system (leads of through-hole components) and to add two grounded copper layers on the top and on the bottom of the PCB to provide even better shielding to the signal traces (Figure 6.18c). Not even this third design solved the problem. The last attempt was therefore to ground the frame of the FT-NMT03 using the same ground of the AD7746 board. This connection was performed with the crocodile cable seen in red in Figure 6.10 and proved to resolve the noise problem, which was immediately reduced and dropped to a value that allowed precise capacitance measurements.

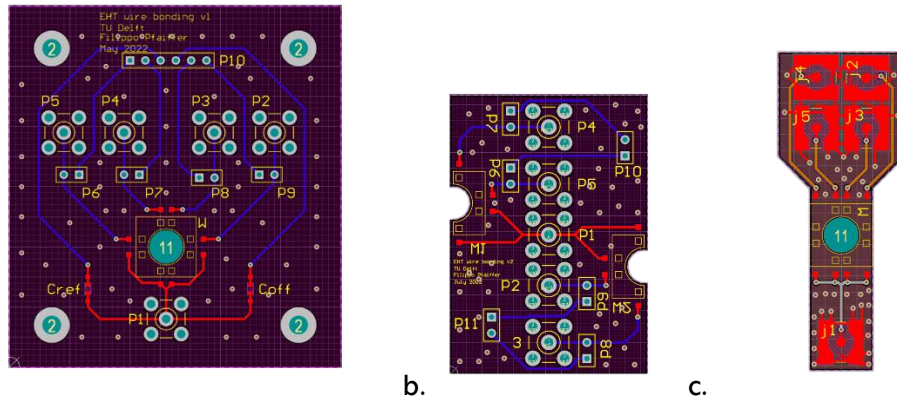


Figure 6.18: Evolution of the PCB for assembling the platforms as a result of problems identified: V1 (a.), V2 (b.), V3(c.).

- Despite this effective reduction in the noise level, signal was still extremely low compared to disturbances, and results related to ΔC in the measurements had to be obtained using MATLAB function `smoothdata`. The parameters used for the smoothing influence the magnitude of the measured ΔC , but in general the trends in the ΔC -force and ΔC -application point curves were maintained regardless of the parameters used (Appendix F).
- During the measurements, the sensors were noticed to be sensitive not only to the pillar movement but also to the nanoindenter silicon tip movement. This conductive tip influences the fringe electric field lines and therefore the capacitance of the sensors (Figure 6.19). Unfortunately, with this setup pillar displacement and tip displacement are coupled and cannot be investigated separately, therefore the measured effect can be a superposition of the two contributions.

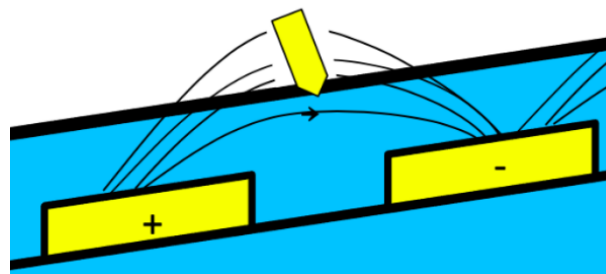


Figure 6.19: Effect of Silicon tip presence on the field lines between the spiral's planes

In any case, the measured ΔC was in the most extreme cases in the order of 30aF (or even less), thus providing the ultimate proof in relation to the readout suitability of the AD7746 component for extreme readouts associated with such low capacitance levels.

6.6. Cell culture and biological measurements

The final test that brings together all the evaluations conducted in relation to this Master Thesis is the test performed with cardiac cells cultured around the pillars. This test constitutes the ultimate validation of the results obtained with nanoindentation experiments, since in this case there is no conductive tip moving on top of the sensors and therefore the only sensed mechanism is the deformation in the substrate.

Because of the good dynamic behaviour of the sensors despite their base capacitance, it was chosen to perform two cell cultures on two platforms that were fully assembled and prepared for this delicate passage.

HiSPC-derived cardiomyocytes, endothelial cells and fibroblasts were seeded in the wells of the two platforms and mixed with a collagen ECM gel by Milica Dostanic at Leiden University Medical Center (LUMC). This mixture was stirred to obtain a uniform distribution inside the wells. The mixture, together with the PCB and relative EHT platform, was then placed in a controlled environment allowing the growth of tissues: an incubator with air environment kept at 95% humidity, 37 °C temperature, and 5% CO₂ concentration.

After one day in the incubator, self-assembly of the cells around the pillars happened as expected, as shown in Figure 6.20, in which respectively four sensors of type A and four of type D can be seen.

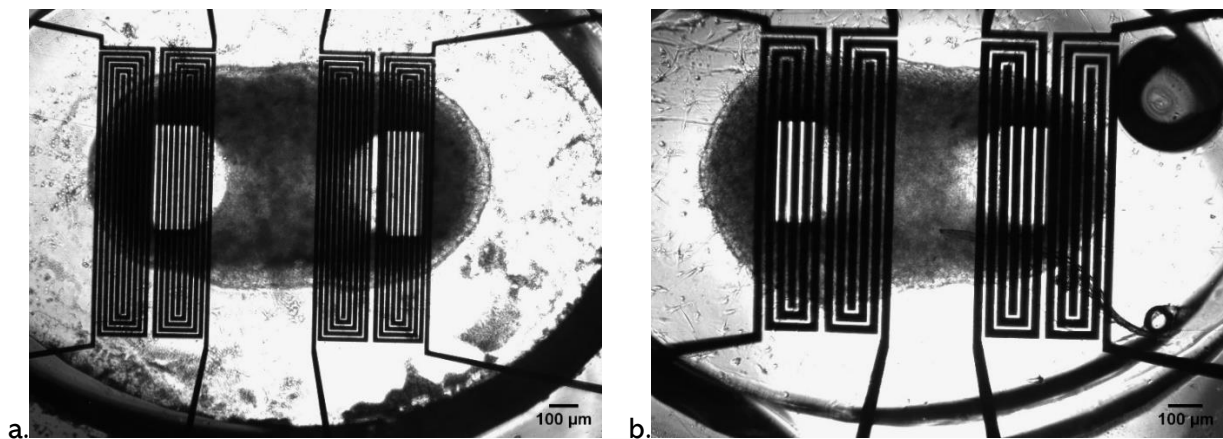


Figure 6.20: Cardiac tissue formation on EHT platforms with integrated sensors of type A (a.) and type D (b.).

Unfortunately, spontaneous contractions of the formed tissues were not observed, therefore electrical measurements of the contraction force were not possible. The reason for the low contractile response of the tissues was related to the cells involved and their culturing procedure. Biocompatibility of the EHT platform remains proven, as the tissues were maintained alive for 14 days. Further experiments with optimized cell cultures will allow more in-depth analysis of the sensor performances.

This obtained result highlights the good biocompatibility of the platform with integrated sensors, since the spontaneous formation of cardiac tissue was not prevented by the materials used in the platform. Moreover, it constitutes one of the first examples of electronic displacement sensors integrated into an EHT device, thus establishing a ground-breaking milestone.

Conclusions and outlook

In this chapter, a brief discussion about the whole project is conducted, to highlight conclusions, to identify possible improvements, and to provide suggestions for future works.

7.1. Conclusions

This thesis was developed as a follow-up to a previous project, during which a spiral capacitive displacement sensor was successfully integrated into the substrate of an EHT device. The extremely low force applied by cardiac tissue, together with the specifications of the sensors (in particular their responsivity) highlighted the need to identify an extremely sensitive and highly precise readout strategy allowing the detection of changes in capacitance in the range of 10aF.

Such a solution was investigated during a literature survey aimed to identify the most suitable readout architectures. Two main solutions were identified in Capacitive-to-Voltage converters (Charge Sensitive Amplifier) and in Capacitive-to-Digital converters ($\Sigma-\Delta$ amplifiers). The specifications of some components available on the market were investigated, two components implementing the two architectures were selected and, as a confirmation of the sensitivity of the architectures, they were revealed to be the most sensitive in the market. These two components are Smartec's UTI (implementing a CSA followed by a Voltage-to-Period converter) and Analog Devices AD7746 (implementing a $\Sigma-\Delta$ converter). The devices were tested and characterized, benchmarking the obtained results with precise laboratory instrumentation measurements, and performing noise analysis and comparisons between the results. The benchmarking provided results in agreement between each other and with the ones obtained with lab instruments, and noise figures of the two components were comparable and in the order of 10aF for RMS noise and 100aF for peak-to-peak noise, in line with the estimated capacitance change in the sensors. Their performance and versatility make those readouts suitable for further experiments and measurements in this or in other biological applications that often involve challenging capacitive readouts.

Beyond this, since fabricated platforms with integrated sensors need to be transferred on a PCB to allow completion of the measurements, the project also focused on the investigation of a suitable assembly procedure for the EHT platform. The developed process was investigated thoroughly, platforms were assembled on the PCBs, and measurements of their static behaviour (base capacitance) provided results in good agreement with the previous simulation, providing an important proof-of-concept for the entire process. Moreover, a preliminary biological test was

performed and cardiac cells self-assembled around the pillars showing good biocompatibility. The culture of cells in an EHT platform with integrated displacement sensors is a breakthrough result empowered by OoC technology, even if to date it was not possible to perform the measurement and to characterize sensors in what is to all extents the final application of this project.

Dynamic testing conducted using nanoindentation provided promising results that need to be confirmed with further experiments. A clear relation between the force applied to the pillars and the change in the capacitance of the sensors was identified, providing a measured responsivity of the sensor slightly smaller compared to the simulated value but still in a reasonable confidence interval.

Despite this, the multiple constraints deriving from such a complex project required the development of a peculiar assembly procedure, far from every standard, above all the use of flexible PDMS substrate for the whole platforms (contact pads included). This process was revealed to be critical and very delicate, originating multiple failure modes that did not allow full dynamic characterization of the platform. These failure modes were analysed and documented, and possible reasons and solutions were provided for each of them to highlight the weaknesses of the process and to leave suggestions for further improvements or changes. Some of these changes were implemented developing slightly different processes, but these only provided slight improvements in the yield, still not allowing to fabricate sensors that consistently and reproducibly maintained the expected base capacitance value throughout the whole assembly process.

In conclusion, through all the evaluation and the experiments performed, this thesis proved the general viability of the whole project, and provided insight into the next steps to take. At the beginning of this study, the expectations about the biggest challenges were all focused on the electronics readout, and the trade-off choice was to produce slightly less robust sensors in order to have greater responsivity. A process addressing mechanical problems, producing sensors that could be transferred reliably, was known but was initially discarded because this would have lowered the responsivity of the sensors. Such a process is reported in Appendix K.

Since in such complex and multidisciplinary projects it is often hard to understand what the biggest challenges and limitations can be, at the end of this project this expectation was not confirmed: so far, the electronics performed well, and it is possible to use it for further experiments and characterization that need to confirm (or reject) the goodness of the results. The biggest problems were instead highlighted in relation to the assembly process. All these problems derive from the mechanical aspects of the platform, which were brought to a point that did not allow the reliable fabrication of devices. A step back needs to be performed, and the reliability of the design and of the process needs to be increased, to allow the investigation of the dynamic behaviour of the developed capacitive sensor and their final characterization with future cell experiments.

7.2. Suggestions for future works

The results of this thesis helped to produce a set of suggestions and of potential future steps to be taken in the completion of this far-from-conclusion project, which will be listed and explained in this Section.

Since the biggest challenges of the project were found to be related to its mechanical reliability, some steps that could be performed in order to improve it are highlighted.

Reintroduce a polyimide buffer layer in the structure, as shown in Appendix K. This first need was identified to increase the stiffness of the substrate since its softness was shown to be one of the main reasons for crack formation, especially in relation to the wire bonding process. In alternative to that, different microfabrication procedures can be investigated to allow the use of more standard assembly procedures. Above all, the attention should be focused on avoiding soft substrate below bonding pads.

Re-design the mask used for the photolithographic development of the sensors. The long and thin aluminium traces were revealed to be very fragile and often not able to match the displacement of the substrate, causing cracking. Even more, the connection of such traces with the contact pads was done via sharp angles and geometries, which revealed prone to originate cracks during the assembly process, highlighting the need for different geometries. At least these two aspects need to be redesigned: viable solutions are sketched in the following figure. Figure 7.1a shows the state of the art, Figure 7.1b presents a more tapered solution for the traces, while Figure 7.1c shows how chamfering can be used. Figure 7.1d follows the approach often used for stretchable interconnects.

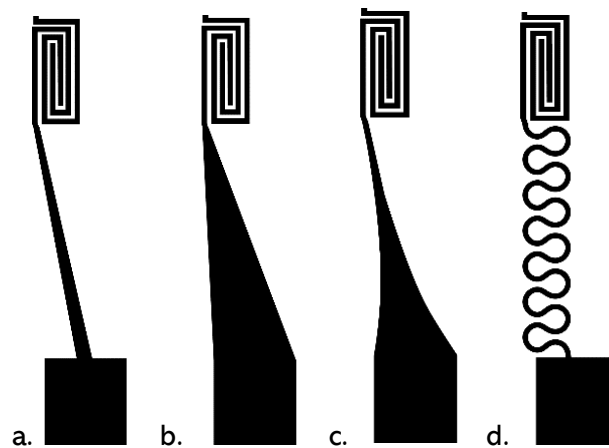


Figure 7.1: Possible solutions to the criticalities related to state-of-the-art geometry (a.). Tapering (b.) or chamfering (c.) can be used for straight traces, or stretchable interconnects (d) can be investigated.

Investigate alternative and more flexible materials for the fabrication of the sensors. Aluminium was initially chosen for its flexibility, but it was revealed to be not enough for this complex application. As an example, in applications where flexible electronics is needed often Carbon Nanotubes (CNTs) are used. After identifying more suitable materials, the whole microfabrication process needs to be optimized again.

Change the assembly process. This can be modified to avoid or to increase the yield of the most critical passages that were highlighted in this thesis. In particular, alternatives to classical wire bonding can be investigated, such as the printing of conductive nanoparticles or equivalent techniques that create an electrical connection without the application of force or pressure.

Always related to fabrication, but not as critical as the previous points is a discussion that becomes evident when looking at Figure 6.20. From the pictures it is possible to notice how the manual placement of the pillars on top of the sensors does not provide perfect alignment, and might therefore influence the dynamic properties of the sensors lowering their responsivity. For next and more precise tests it is therefore necessary to investigate a process that allows more precise alignment of the pillars on top of the sensors.

Once all the problems related to the assembly and to the mechanics of the platform are addressed, there are still some aspects that need to be improved in the electronics as well.

In the first place, part of the tests to perform sensor characterisation from a dynamic point of view still needs to be performed. Further nanoindentation tests need to be performed first to create some statistics related to the results shown in Section 6.5, and to address the problems identified and explained in Section 6.5.1. Moreover, biological measurements and characterizations need to be performed and the results need to be benchmarked with classical optical sensing to draw conclusions on the quality of this alternative measurement technique. If the results of the tests show that the sensitivity of the component is enough to read out the sensors and the changes in capacitance associated with the contraction of the cardiac tissue, then the need to read out multiple sensors needs to be faced.

After the final verifications related to the readout suitability, the first need is to develop the possibility to implement differential readout, which might also help the readout specifications themselves. AD7746 is already designed to have the possibility to read out two differential sensors. Concerning UTI, during this project a board to invert and to buffer the excitation signal was developed (schematic and brief explanation are presented in Appendix B.4), but never properly evaluated because the focus was moved to other problems. This board can be a starting point for the development of a circuit that also allows UTI to perform differential readout.

If the analysis of one single pillar involves the readout of two sensors, the readout of a whole platform requires the readout of four sensors, and the readout of multiple platforms requires even more sensors to be monitored at the same time. This need must be faced as well in the future: a possible starting point for this analysis can be the use of multiplexers together with the selected component. Concerning the UTI component, a multiplexer was developed by Smartec, whose connection is shown in Figure 7.2. This component (MUX03) multiplexes the excitation signal of the sensor, thus allowing the readout of multiple sensors instead of a single one.

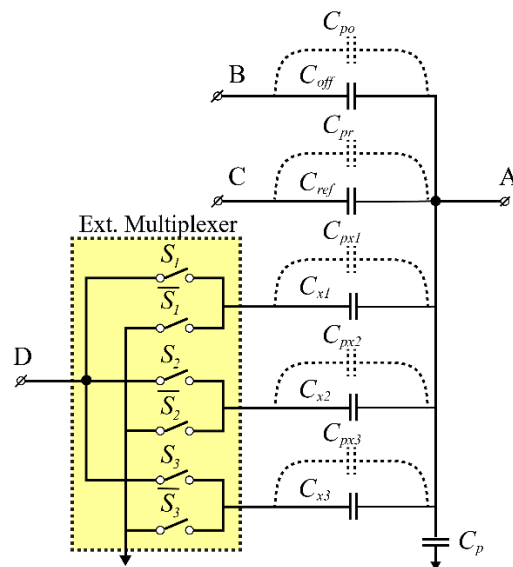


Figure 7.2: MUX03 working principle in relation to UTI pinout.

In the case of AD7746, an I^2C multiplexer can in principle be used, such as the TCA9548A component. This component can be connected to a microcontroller board (such as Arduino or Raspberry) and multiple AD7746 can be connected to it to solve the conflict generated by the fixed I^2C address of AD7746 components.

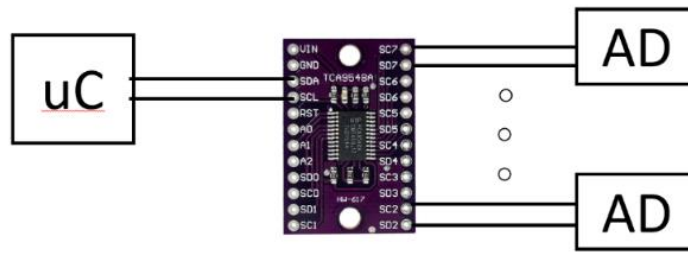


Figure 7.3: TCA9548A connections.

In both cases, the suitability of the approach in terms of measurement time, noise introduced by the switches, and the final portability of the system must be investigated.

After all the evaluation related to the performance of the sensors and of the platform, as a final suggestion, it might also be interesting to evaluate the long-term reliability and behaviour of the devices, to identify any possible problem or change in the behaviour of the sensors. An example of a question that can be answered is related to the molecule absorption of PDMS, which might affect its relative permittivity, changing therefore the specifications of the sensors.

References

- [1] M. Mastrangeli, S. Millet, T. Orchid Partners, and J. Van den Eijnden-van Raaij, "Organ-on-chip in development: Towards a roadmap for organs-on-chip," (in eng), *Altex*, vol. 36, no. 4, pp. 650-668, 2019, doi: 10.14573/altex.1908271.
- [2] L. A. Low, C. Mummery, B. R. Berridge, C. P. Austin, and D. A. Tagle, "Organs-on-chips: into the next decade," *Nature Reviews Drug Discovery*, vol. 20, no. 5, pp. 345-361, 2021/05/01 2021, doi: 10.1038/s41573-020-0079-3.
- [3] Dutch-Foundation-for-Biosciences-and-Society, "Mini Organs-on-Chips: Towards new research models for studying disease and finding treatments," 2020. [Online]. Available: <https://www.biomaatschappij.nl/wp-content/uploads/2020/11/BWM-Mini-Organs-on-Chips.pdf>.
- [4] hDMT, "Organ-on-chip Technology and hDMT," 2016.
- [5] B. Zhang, A. Korolj, B. F. L. Lai, and M. Radisic, "Advances in organ-on-a-chip engineering," *Nature Reviews Materials*, vol. 3, no. 8, pp. 257-278, 2018/08/01 2018, doi: 10.1038/s41578-018-0034-7.
- [6] A. van de Stolpe and J. den Toonder, "Workshop meeting report Organs-on-Chips: human disease models," *Lab on a Chip*, 10.1039/C3LC50248A vol. 13, no. 18, pp. 3449-3470, 2013, doi: 10.1039/C3LC50248A.
- [7] M. Dostanić *et al.*, "A Miniaturized EHT Platform for Accurate Measurements of Tissue Contractile Properties," *Journal of Microelectromechanical Systems*, vol. 29, no. 5, pp. 881-887, 2020, doi: 10.1109/JMEMS.2020.3011196.
- [8] Mauriac, "Organs on chip review." [Online]. Available: <https://www.elflow.com/microfluidic-reviews/organs-on-chip-3d-cell-culture/organs-chip-review/>.
- [9] M. Shojaei-Baghini, "Design and Development of Integrated Displacement Sensors for Engineered Heart Tissue Platforms," *TU Delft*, Master Thesis 2020.
- [10] R. J. Mills *et al.*, "Functional screening in human cardiac organoids reveals a metabolic mechanism for cardiomyocyte cell cycle arrest," *Proceedings of the National Academy of Sciences*, vol. 114, no. 40, p. E8372, 2017, doi: 10.1073/pnas.1707316114.
- [11] D. Silva and S. Pichorim, "Modeling of Open Square Bifilar Planar Spiral Coils," *Journal of Microwaves, Optoelectronics and Electromagnetic Applications*, vol. 17, pp. 319-339, 09/01 2018, doi: 10.1590/2179-10742018v17i31254.
- [12] A. Cutolo, V. Pagliarulo, F. Merola, S. Coppola, P. Ferraro, and M. Fraldi, "Wrinkling prediction, formation and evolution in thin films adhering on polymeric substrata," *Materials & Design*, vol. 187, p. 108314, 11/01 2019, doi: 10.1016/j.matdes.2019.108314.
- [13] G. W. de Jong, "Smart Capacitive Sensors - Physical, Geometrical and electronic aspects," *TU Delft*, Ph.D. Thesis 1994.
- [14] W. Heerens, "Application of capacitance techniques in sensor design," *Journal of Physics E: Scientific Instruments*, vol. 19, p. 897, 11/29 2000, doi: 10.1088/0022-3735/19/11/002.
- [15] X. Li and G. C. M. Meijer, "Capacitive Sensors," in *Smart Sensor Systems*, 2008, pp. 225-248.
- [16] X. Hu and W. Yang, "Planar capacitive sensors – designs and applications," *Sensor Review*, vol. 30, no. 1, pp. 24-39, 2010, doi: 10.1108/02602281011010772.
- [17] A. Heidary, "A Low-Cost Universal Integrated Interface for Capacitive Sensors," 01/01 2010.
- [18] A. Oja, "Capacitive sensors and their readout electronics," 12/09 2010.
- [19] M. A. P. Pertijs and Z. Tan, "Energy-efficient capacitive sensor interfaces," *Nyquist AD Converters, Sensor Interfaces, and Robustness - Advances in Analog Circuit Design, AACD 2012*, pp. 129-147, 01/01 2013, doi: 10.1007/978-1-4614-4587-6-8.
- [20] L. Zhong, X. Lai, and D. Xu, "Oversampling Successive Approximation Technique for MEMS Differential Capacitive Sensor," *IEEE Journal of Solid-State Circuits*, vol. 53, no. 8, pp. 2240-2251, 2018, doi: 10.1109/JSSC.2018.2827922.
- [21] L. Xiujun and G. C. M. Meijer, "An accurate interface for capacitive sensors," *IEEE Transactions on Instrumentation and Measurement*, vol. 51, no. 5, pp. 935-939, 2002, doi: 10.1109/TIM.2002.807793.
- [22] N. Yazdi, H. Kulah, and K. Najafi, "Precision readout circuits for capacitive microaccelerometers," in *SENSORS, 2004 IEEE*, 24-27 Oct. 2004 2004, pp. 28-31 vol.1, doi: 10.1109/ICSENS.2004.1426091.
- [23] F. Polo, "Differential read-out circuit for capacitive sensors," *Università degli Suddi di Padova*, Master Thesis 2012.
- [24] C. Rogi, C. Buffa, N. De Milleri, R. Gaggl, and E. Prefasi, "A Fully-Differential Switched-Capacitor Dual-Slope Capacitance-To-Digital Converter (CDC) for a Capacitive Pressure Sensor," *Sensors*, vol. 19, no. 17, doi: 10.3390/s19173673.
- [25] Y. Yoo and B.-D. Choi, "Readout Circuits for Capacitive Sensors," *Micromachines*, vol. 12, no. 8, doi: 10.3390/mi12080960.
- [26] S. Wang *et al.*, "A Power-Efficient Capacitive Read-Out Circuit With Parasitic-Cancellation for MEMS Cochlea Sensors," *IEEE Transactions on Biomedical Circuits and Systems*, vol. 10, no. 1, pp. 25-37, 2016, doi: 10.1109/TBCAS.2015.2403251.

- [27] P. Horowitz, *The art of electronics / Paul Horowitz, Winfield Hill* (no. Accessed from <https://nla.gov.au/nla.cat-vn2587786>). Cambridge [England]: Cambridge University Press, 1989.
- [28] A. Heidary and G. C. M. Meijer, "Features and Design Constraints for an Optimized SC Front-End Circuit for Capacitive Sensors With a Wide Dynamic Range," *IEEE Journal of Solid-State Circuits*, vol. 43, no. 7, pp. 1609-1616, 2008, doi: 10.1109/JSSC.2008.922390.
- [29] X. Lai, Y. Wang, M. Liu, and L. Zhang, "The SI and EMI Analysis of Sub-Femto-Farad readout circuit for capacitive sensor," in *2019 12th International Workshop on the Electromagnetic Compatibility of Integrated Circuits (EMC Compo)*, 21-23 Oct. 2019 2019, pp. 252-256, doi: 10.1109/EMCCompo.2019.8919907.
- [30] Smartec, "UTI Datasheet," Datasheet 2016.
- [31] Z. Tan, "Energy-Efficient Capacitive-Sensor Interfaces," *TU Delft*, Ph.D. Thesis 2013.
- [32] F. van der Goes, "Low-Cost Smart Sensor Interfacing," *TU Delft*, Ph.D. Thesis 1996.
- [33] G. Meijer, M. Pertijs, and K. Makinwa, *Smart Sensor Systems: Emerging Technologies and Applications*. 2014, pp. 1-279.
- [34] U. Ferlito, A. D. Grasso, S. Pennisi, M. Vaiana, and G. Bruno, "Sub-Femto-Farad Resolution Electronic Interfaces for Integrated Capacitive Sensors: A Review," *IEEE Access*, vol. 8, pp. 153969-153980, 2020, doi: 10.1109/ACCESS.2020.3018130.
- [35] M. Gasulla, L. Xiujun, and G. C. M. Meijer, "The noise performance of a high-speed capacitive-sensor interface based on a relaxation oscillator and a fast counter," *IEEE Transactions on Instrumentation and Measurement*, vol. 54, no. 5, pp. 1934-1940, 2005, doi: 10.1109/TIM.2005.853684.
- [36] N. Semiconductor, "Noise specs confusing?," Application Note 1974.
- [37] A. Quintero, F. Cardes, L. Hernandez, C. Buffa, and A. Wiesbauer, "A Capacitance-to-Digital Converter Based on a Ring Oscillator with Flicker Noise Reduction," in *2016 Austrochip Workshop on Microelectronics (Austrochip)*, 19-19 Oct. 2016 2016, pp. 40-44, doi: 10.1109/Austrochip.2016.019.
- [38] J. V. Rethy and G. Gielen, "An energy-efficient capacitance-controlled oscillator-based sensor interface for MEMS sensors," in *2013 IEEE Asian Solid-State Circuits Conference (A-SSCC)*, 11-13 Nov. 2013 2013, pp. 405-408, doi: 10.1109/ASSCC.2013.6691068.
- [39] J. Van Rethy, V. De Smedt, W. Dehaene, and G. Gielen, "Towards Energy-Efficient CMOS Integrated Sensor-to-Digital Interface Circuits," 2015, pp. 379-397.
- [40] A. Quintero, F. Cardes, C. Perez, C. Buffa, A. Wiesbauer, and L. Hernandez, "A VCO-Based CMOS Readout Circuit for Capacitive MEMS Microphones," *Sensors*, vol. 19, no. 19, doi: 10.3390/s19191426.
- [41] W. Petchmaneelumka, P. Phankamnerd, A. Rerkratn, and V. Riewruja, "Capacitive sensor readout circuit based on sample and hold method," *Energy Reports*, vol. 8, pp. 1012-1018, 2022/04/01/ 2022, doi: <https://doi.org/10.1016/j.egy.2021.11.128>.
- [42] M. M. Ghanbari, J. M. Tsai, A. Nirmalathas, R. Muller, and S. Gambini, "An Energy-Efficient Miniaturized Intracranial Pressure Monitoring System," *IEEE Journal of Solid-State Circuits*, vol. 52, no. 3, pp. 720-734, 2017, doi: 10.1109/JSSC.2016.2633510.
- [43] H. Song, Y. Park, H. Kim, D.-i. D. Cho, and H. Ko, "Fully Integrated Low-Noise Readout Circuit with Automatic Offset Cancellation Loop for Capacitive Microsensors," *Sensors*, vol. 15, no. 10, pp. 26009-26017, doi: 10.3390/s151026009.
- [44] R. A. Brookhuis, T. S. J. Lammerink, and R. J. Wiegerink, "Differential capacitive sensing circuit for a multi-electrode capacitive force sensor," *Sensors and Actuators A: Physical*, vol. 234, pp. 168-179, 2015/10/01/ 2015, doi: <https://doi.org/10.1016/j.sna.2015.08.020>.
- [45] R. A. Brookhuis, R. J. Wiegerink, T. S. J. Lammerink, and G. J. M. Krijnen, "Three-axial force sensor with capacitive read-out using a differential relaxation oscillator," in *SENSORS, 2013 IEEE*, 3-6 Nov. 2013 2013, pp. 1-4, doi: 10.1109/ICSENS.2013.6688398.
- [46] J. Wei, C. Yue, Z. L. Chen, Z. W. Liu, K. A. A. Makinwa, and P. M. Sarro, "Implementation and Characterization of a femto-Farad Capacitive Sensor for pico-Liter Liquid Monitoring," *Procedia Chemistry*, vol. 1, no. 1, pp. 120-123, 2009/09/01/ 2009, doi: <https://doi.org/10.1016/j.proche.2009.07.030>.
- [47] G. Gervasoni, M. Carminati, and G. Ferrari, "FPGA-based lock-in amplifier with sub-ppm resolution working up to 6 MHz," in *2016 IEEE International Conference on Electronics, Circuits and Systems (ICECS)*, 11-14 Dec. 2016 2016, pp. 117-120, doi: 10.1109/ICECS.2016.7841146.
- [48] G. Stimpson, M. Skilbeck, R. Patel, B. Green, and G. Morley, "An open-source high-frequency lock-in amplifier," *Review of Scientific Instruments*, vol. 90, p. 094701, 09/01 2019, doi: 10.1063/1.5083797.
- [49] H. Ouh *et al.*, *Sub-fF trimmable readout circuit for tri-axes capacitive microaccelerometers*. 2012, pp. 1-4.
- [50] B. E. Boser, "Capacitive Interface Electronics for Sensing and Actuation," *University of California, Berkeley*, 2012.
- [51] S. Xia, K. Makinwa, and S. Nihtianov, "A capacitance-to-digital converter for displacement sensing with 17b resolution and 20 μ s conversion time," in *2012 IEEE International Solid-State Circuits Conference*, 19-23 Feb. 2012 2012, pp. 198-200, doi: 10.1109/ISSCC.2012.6176973.

- [52] J. T. Kung and H. S. Lee, "An integrated air-gap-capacitor pressure sensor and digital readout with sub-100 attofarad resolution," *Journal of Microelectromechanical Systems*, vol. 1, no. 3, pp. 121-129, 1992, doi: 10.1109/84.186391.
- [53] P. Ciccarella, M. Carminati, M. Sampietro, and G. Ferrari, "Multichannel 65 zF rms Resolution CMOS Monolithic Capacitive Sensor for Counting Single Micrometer-Sized Airborne Particles on Chip," *IEEE Journal of Solid-State Circuits*, vol. 51, pp. 2545-2553, 11/01 2016, doi: 10.1109/JSSC.2016.2607338.
- [54] J. Pérez Sanjurjo, E. Prefasi, C. Buffa, and R. Gaggl, "A Capacitance-To-Digital Converter for MEMS Sensors for Smart Applications," *Sensors*, vol. 17, no. 6, doi: 10.3390/s17061312.
- [55] Y. He, Z. y. Chang, L. Pakula, S. H. Shalmany, and M. Pertijs, "27.7 A 0.05mm² 1V capacitance-to-digital converter based on period modulation," in *2015 IEEE International Solid-State Circuits Conference - (ISSCC) Digest of Technical Papers*, 22-26 Feb. 2015 2015, pp. 1-3, doi: 10.1109/ISSCC.2015.7063138.
- [56] N. Couniot, L. A. Francis, and D. Flandre, "A 16 x 16 CMOS Capacitive Biosensor Array towards Detection of Single Bacterial Cell," *IEEE Transactions on Biomedical Circuits and Systems*, vol. 10, 05/14 2015, doi: 10.1109/TBCAS.2015.2416372.
- [57] G. Scotti, S. Pennisi, P. Monsurrò, and A. Trifiletti, "88- μ A 1-MHz Stray-Insensitive CMOS Current-Mode Interface IC for Differential Capacitive Sensors," *IEEE Transactions on Circuits and Systems I: Regular Papers*, vol. 61, no. 7, pp. 1905-1916, 2014, doi: 10.1109/TCSI.2014.2298275.
- [58] D. Lin, "An atto-Farad resolution closed loop impedance measurement bridge for capacitive sensors," *TU Delft*, Master Thesis 2018.
- [59] Y. Lu, A. Nathan, T. Manku, and Y. Ning, "Thin film magnetostrictive sensor with on-chip readout and attoFarad capacitance resolution," in *International Electron Devices Meeting. Technical Digest*, 8-11 Dec. 1996 1996, pp. 777-780, doi: 10.1109/IEDM.1996.554095.
- [60] A. Devices, "AD7746 Datasheet," Datasheet.
- [61] Smartec, "UTI Evaluation Board Datasheet," Datasheet 2017.
- [62] A. Devices, "AD7746EB Datasheet," Datasheet.
- [63] [Online]. Available: http://www.falco-systems.com/low_noise_high_voltage_amplifiers.html.
- [64] FemtoTools, "FT-NMT03 product description." [Online]. Available: <https://www.femtotools.com/previousproducts/ft-nmt03-nanomechanical-testing-system>.

Appendix A

Literature review on OoCs and EHTs

A.1 Introduction

In 2010 Dongeun Huh, a Postdoc at Harvard University working at the Wyss Institute [1] in the group of Professor Donald Ingber, published a paper called “Reconstituting Organ-Level Lung Functions on a Chip” [2]. Even if this paper was aimed to recapitulate the functionality of lungs on a small platform, the academic community immediately saw the possibility to exploit this novel approach to recapitulate different organs. Thus, with that paper, the researchers pioneered the field of Organs-on-Chip (OoC) and formally marked the start of this innovative technology.

Twelve years later, the interest that gathers around this technology both in academia and in the industry is still increasing and led to the creation of multiple research groups, organizations, companies, and start-ups [3]. This great interest is motivated by the fact that OoC technology is expected to build a new paradigm for disease modelling and drug development, solving some of the biggest problems of these research fields. The development of microfluidic devices containing living cell cultures and replicating (at least in part) organs’ functionalities may contribute to the development of disease models that are more accurate than the ones utilized until now, and tests and experiments aimed to study the reaction of these tissues to drugs can open the road to cheaper, faster, and more accurate pre-clinical trials [4]. Moreover, thanks to this in-vitro approach that can recapitulate some advantages of the in-vivo experiments, it may be possible to find an alternative to ethically controversial animal tests; and new development in genetics may pave the road to a new concept of medicine which is more efficient because of personalization of treatments and dosages.

Since this paradigm applies to multiple diseases to develop different types of drugs, the number of papers that have been published about OoC in the last years has increased constantly [5]. The focus of the researchers has spread in many directions, creating platforms that can recreate the functionalities (such as absorption or contraction) of many different organs and tissues, from lungs to skeletal muscles. In the last years, also multi-organ platforms have been proposed to assess the relations of different tissues, an aspect that is particularly interesting in relation to drugs’ toxicity [6]. One of the organs that gathered more interest in the literature is the heart, because of the complexity related to modelling cardiac diseases and because these diseases are the main cause of death in our society [7]. Moreover, many drugs show cardiotoxicity in a late stage of their development, therefore platforms that allow to assess the cardiotoxicity of substances in a more reliable way are urgently needed.

Despite the great enthusiasm that characterized the development of this recent technology, the main reason why it cannot be considered yet as entirely mature is that it still has some gaps that need to be filled before it can be applied in an industrial environment. Moreover, agencies that regulate drugs development such as EMA and FDA have very strict regulations, and sufficient proof

of the effectiveness of Organ-on-Chip is still missing [4]. Therefore, even though OoCs are considered among the most promising innovations to improve the quality of medicine worldwide, more research and multiple steps need to be performed to fill the gap.

A.2. Organs-on-Chip

Organs-on-Chip are defined as “microdevices engineered to contain (human) cells and tissues and to model or mimic organ structures, functions and recreations to biological conditions, stressors, or compounds” [8]. These devices aim to host and cultivate the smallest functional modules of tissues using microfluidics, microelectronics, and microfabrication. Therefore, OoC developers do not want to create a real and living organ, but just to recreate a minimal function, to model a single or a few processes [9]. This translates into the idea that the devices, to mimic a single functionality of an organ, must be “as simple as possible, as complex as needed” [4].

Single functionalities, such as contraction or absorption, are strictly related to the dynamic condition of the organ inside the body and can be replicated using mechanical, electrical, or biochemical stimuli. Studying how the functionalities of the tissues change in response to drugs or to application of these stimuli allow researchers to develop new and more accurate models not only for healthy organs but also for diseased tissues, studying how these react to drugs. These reactions can be assessed because cell conditions can ideally be monitored in real-time thanks to imaging or to sensors integrated into the platform.

As said, OoC platforms must allow the stimulation of the tissue to mimic the normal functioning of the organs. To better recreate this functioning, platforms are normally not planar and frequently exploit mechanical parts that allow the creation of tridimensional structures, such as cavities, pillars, or scaffolds. These structures can move, bend, or deflect exerting forces on the tissues that are studied, thus providing the stimuli needed for the testing [9]. Besides that, microfluidics structures such as wells or pipes are integrated into the platform, in order, for example, to recreate liquids or nutrient flow that are normally present in organs [6]. An illustration of different investigated OoCs and of their working principle is shown in Figure A.1.

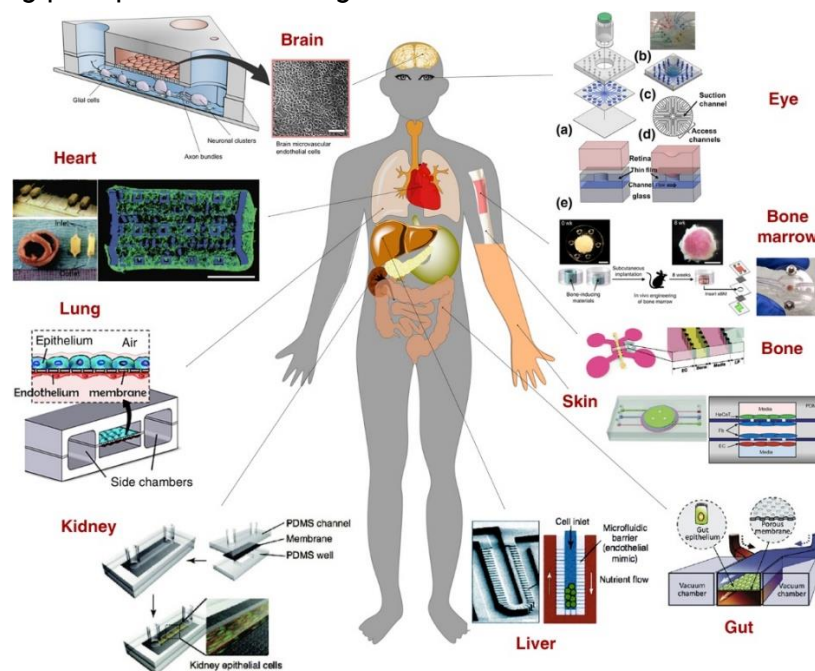


Figure A.1: Illustration of different OoC and their working principle (Derived from [10]).

Because of the visual inspection that often needs to be performed on the cell cultures to verify their functionality and their reactions, one of the desired characteristics for the materials of which the platforms are made of is high optical transparency. Moreover, these materials, since they are in contact with cells and other biological compounds, need to be biocompatible and need to be suitable for microfabrication techniques because of the small features that need to be fabricated in the platforms. The most common material to satisfy all the above-mentioned requirements is a silicone elastomer called polydimethylsiloxane (PDMS) which is elastic, a characteristic that is essential to guarantee the dynamic functioning of the platforms.

A.2.1 Reasons for the development

The huge interest raised by OoC development has four main reasons, which will be listed below, and that directly come from four limitations of the actual medical paradigm.

Low precision of standard developed models. The first limitation is that the development of models for diseases used in pre-clinical studies has been very effective in many situations, but failed in many other cases [11]. Until now, these models have been developed mainly after studies that considered cell cultures containing a single cell type, generally cultured in bi-dimensional structures. These methods did not take into account the human genome, physical factors, or any other type of external stimulation [4]. This approach is demonstrated to fall short in certain situations, and many models are not able to capture the features of a disease. The effect is that most of the drugs developed for this kind of models are effective to cure the symptoms of a disease, but not the cause of it. Since 2D cell cultures have different physiological properties and therefore different responses to drugs and stimuli, and since treatments that work in 2d structures may fail in 3d structures [12], using dynamic three-dimensional tissue formations made of multiple cell types which interact with each other seems to be a promising way to develop more accurate models.

Cost and duration of drugs development. The second limitation, and probably the most important, is related to the process of developing new drugs. The first thing to consider is that for many diseases effective drugs are still to be discovered and developed. The second is that, even for diseases that now have an effective drug, the drug development process is long and expensive. It is estimated that on average, the time needed to develop a new drug is around 12 years and that the cumulative cost for each new drug is between 1 and 3 billion dollars [4]. This is not expected to get any better, according to an empirical law that could be called Eroom's law (in opposition to Moore's law for the semiconductor industry [13]) which says that the number of developed drugs per billion dollars spent on research is constantly lowering [14]. The main reasons for these costs being so high are mainly the long processes required to approve a medicine (that consists of multiple phases) and drug failures that happen at a late chemical testing stage.

Because of the better reproduction of organs' physiology, OoCs are expected to make drug development not only faster and cheaper but also more reliable [12]. In detail, estimations say that the cost reduction for drug development can be up to 26% of the total cost, thus reducing the commercial price of drugs and making them more affordable for a bigger part of the population.

Low drug effectiveness. The third problem in modern medicine is that drug effectiveness in the population is extremely low. As shown in Figure A.2, for the most used medicines in the US the

effectiveness on the patient goes from a best case of 25% to a worst case of 4%. This means that only four patients out of one hundred would witness benefits coming from the treatment.

The other 96 people may find the treatment useless and receive no benefits from it, but a small part of them may also react differently and experience side effects, which constitute the 4th case of death in the US [5]. The reason behind it is that many factors affect the response to medicines, among which are age, gender, ethnical aspect, and alimentation. Generally, the cells on which medicines are tested are derived from a population that is small if compared to all the possible combinations.

OoC technology may lead toward a more personalized idea of medicine since it is ideally possible to create a platform to simulate the organs of every single individual. Thus, it may be possible to evaluate not only the individual reaction to a drug in advance but also the correct dosage, which can be identified before starting the treatment.



Figure A.2: Effectiveness of the ten most profitable drugs in the US (Derived from [15]).

Extended and systematic use of animal testing. The last limitation of actual medicine is that it heavily relies on animal testing. Animals' anatomy, physiology, and metabolism can be similar to humans', but will never be the same. For instance, the genome of a mouse is 95% similar to the genome of a human, meaning that there is still a 5% difference that can lead to errors in modelling and in testing [4]. Besides this aspect, animal testing frequently raises ethical questions, and public opinion is shifting toward the rejection of this practice. The use of animal testing has already been prohibited in Europe in 2013 in relation to the cosmetic industry and is getting more and more strict for medical development too since many countries are already adopting the 3Rs protocol for animal testing: reduction, refinement, and replacement [4]. However, animals are full organisms and the tests conducted on them allow researchers to investigate the full systemic interaction of different

organs with each other: this is the reason why not only single Organs-on-chip are developed, but also multiple-organ platforms are researched, with final target to develop a Human-on-Chip platform.

A.2.2 A multidisciplinary field

OoC is by its intrinsic nature a multidisciplinary research field, which is located at the convergence between biology (in particular genetics), mechanics (and in detail its down-scaled applications such as microfluidics and microfabrication), electronics, and chemistry. It should be no surprise, therefore, that the development of such a field started only after all these disciplines reached a certain degree of maturity and were put in contact.

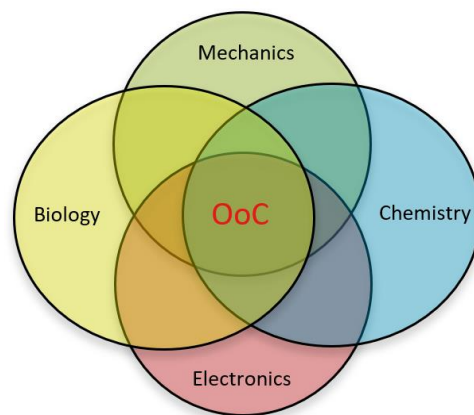


Figure A.3: OoC and its multidisciplinary domain.

The last 50 years marked the strong affirmation of electronics as the discipline with the biggest impact on society, thanks to the great research that led to the fast and constant development explained by Moore's law [13]. With the constant downscaling that characterized electronic development, the industry had to keep pace and develop microfabrication capabilities that were impossible to foresee only 40 years ago. When it became clear that these capabilities could be used not only to create electrical devices but also to downscale the – until then – typically macroscopic mechanical world, a new research field developed: MEMS (Micro Electro Mechanical Systems) were born.

In the meantime, also thanks to the introduction of PDMS, the field of fluidics started to explore its downscaled version as well, thus creating what later became microfluidics.

In 2000 the human genome was sequenced, thus paving the road to modern genetics, and in 2007 Yamanaka won the Nobel Prize for the discovery of Human-induced Pluripotent Stem Cells (HiPSC) [16]. These cells could be taken from the skin, blood, or urine of every individual, and could be reprogrammed altering their DNA sequences to be able to form every cell in the body. The two main revolutions introduced by this discovery were the possibility of recreating every cell of the body starting from a different type of cell, and the possibility to create cells that showed certain characteristics depending on the individual they were taken from. The problem with these cells is that they are less developed than primary cells, and therefore in some cases, a biopsy would be preferable even if the invasive surgery required makes it a less viable option. But the drawbacks are highly compensated by the advantages: HiPSC can be taken from anyone, and this allowed to

recreate several types of cells that, depending on the person they were taken from, could be healthy or diseased and can also show age ethnical differences.

It is now clear why OoC was first developed in 2010: this technology needed all the above-mentioned developments to be effective.

A.2.3 Different types of OoC

The first developed OoC platform was related to lung functionalities, and it aimed to mimic an alveolus to study inflammations due to inhaled nanoparticles. After this first module, many others were developed, trying to reproduce diseases such as pneumonia, asthma, SARS-CoV-2, SARS, and MERS. Large interest was also lifted by the possibility to create a model for the absorption of drugs via the lungs (inhalation).

After this first organ was successfully mimicked and reproduced, many other attempts have been reported with different organs, and many of them have been successfully reproduced. Here is a list of the most commonly reproduced OoC, with the main diseases that motivate the development of the platforms [4-6, 8, 11, 12].

- **Gut-on-chip:** intestine is responsible for the absorption of nutrients and is also related to the immune system, therefore research has been performed to inquire about these aspects.
- **Kidney-on-chip:** these platforms were developed mainly in relation to the investigation performed around chronic kidney failure.
- **Liver-on-chip:** liver has a fundamental role in the human body concerning the absorption of toxic substances. Hepatotoxicity is one of the main reasons for drug failure at the initial stages. Huge interest was also lifted by the study of widespread diseases such as cirrhosis and hepatitis.
- **Brain-on-chip:** research in this field is especially related to blood-brain barriers. OoC technology has been particularly explored in relation to the brain because of the dramatic difference between human brains and models derived from animals. Better models can help to cure pathologies like Alzheimer, ADHD, epilepsy, and depression.
- **Heart-on-chip:** as mentioned, cardiotoxicity is one of the main side effects of developed drugs. Diseases such as coronary artery disease, thrombosis, and arrhythmia are among the main causes of death worldwide.

Not only single organs have been investigated, but also platforms connecting different tissues and cell types have been reported. For example, liver and kidney platforms have been connected in an experiment to test drug toxicity [17], and even four-organs models have been developed [18].

Apart from organs, also other tissues and cell types with specific functionalities have been reproduced, for example, a great interest is lifted by the study of some of the biggest health challenges in western society: thrombosis, and atherosclerosis. The study of such diseases required the development of Blood-Vessels-on-Chip [19]. Another example is provided by Skin-on-Chip, that have been reported to test inflammatory response, burns, and eczema but has also been used as a testing platform for cosmetic products [20].

Considerable importance is also given to the modelling of real diseases on a chip, such as in the case of the biggest challenge of modern medicine, which is cancer. Cancer-on-Chip has been developed to derive better models for metastasis, which is the main cause of death in cancer patients [21].

A.2.4 Gaps and unmet needs

Despite the great interest lifted by the OoC technology and the intense research effort conducted in the last years, this technology is still to be considered a big promise. The reason is that great gaps still exist and need to be filled before this technology can be adopted by pharmaceutical industry protocol [4]. The main and obvious reason is because of the still insufficient evidence of the superiority of this approach compared to the standard protocols adopted until now. Because of that, the OoC approach has just recently been considered by the American Food and Drug Administration (FDA) agency as an alternative to the strict regulations for the development of drugs [22], which has to follow long and articulated protocols consisting of multiple phases to ensure the safety of the new developments and therefore the quality of the models used. In this sense, the OoC approach is still to be verified because cells developed from hiPSC are proven to be different from the cells that can be found in adult tissue.

In addition to that, to confirm the quality of OoC as drug testing platforms, a “library” of reference drugs should be created, thus creating a paradox: to decide if drug testing results are reliable, there is the need to use drugs that have already been tested with other methods [4].

The second gap to be filled is still the low fabrication yield of such devices, that at the moment is around 50%-60% and makes OoC a very good option for research environment, but not yet a marketable solution [23].

Strictly related to the fabrication issue is the fact that PDMS, which is the most widely used material to fabricate OoC platforms, has been proven to absorb small hydrophobic molecules. This absorption can change solution concentrations in the channels, causing potential alteration of experimental results [24], and therefore alternative materials are being evaluated.

To allow standardization of tests and of procedures, bigger steps need also to be taken in terms of microfluidics knowledge, since the dimensions of the devices are becoming so small that surface effects start to have an important role, and in terms of imaging and readout, since the preferred way to assess contraction and movements of the tissues is still optical sensing, while integrated sensing and readout in the platform would allow a real-time assessment of the functionalities. The creation of multipurpose systems, to obtain “libraries” of solutions in terms of microfluidics or readout, is another aspect that must be investigated to allow OoC technology to reach its full potential.

A.2.5 Next steps to be taken

To bridge the gap discussed in the previous section between academic research and industry, many interdisciplinary organizations have been formed to create a roadmap and to agree on further steps that need to be taken to push the technology to a more mature stage. In the Netherlands, inside the Human Organ and Disease Model Technology (hDMT) consortium, Netherlands Organ-on-Chip Initiative (NOCI) was created to reserve a special focus on OoC: and in the same context also European projects were created, such as the Organ-on-Chip Development (ORCHID) project, which later led to the formation of the European Organ-on-Chip Society (EUROOCS).

The guidelines provided by the organizations all point in the same direction. First of all, they focus on standardization [25]. This can be translated into the creation of sets of standardized tests and procedures for the assessment of the quality of experiments and of the safety of the protocols followed, together with guidelines related to sizes and interface rules for OoC devices.

Scaling, together with the creation of multipurpose platforms, may help to increase the yield of platforms' production, exploiting the common procedures of industrial microfabrication that can lead to the development of volume manufacturing, thus allowing for lower production costs.

A.3. Engineered Heart Tissue

As said, OoC are developed mainly because disease models derived from bidimensional cell cultures sometimes fail to accurately mimic human physiology. Therefore, special attention is given to those organs that suffer from diseases that are difficult to model, or for which an effective medical treatment is still lacking. This is the case of the heart, which has been widely investigated and reproduced through different platforms in the last decade. The main reasons behind the special attention reserved to Heart-on-Chip are two: heart diseases are the first cause of death in western society, and cardiotoxicity is the first reason why drugs are retired from the market. It is estimated that for every drug that is retired, pharmaceutical companies suffer 1 billion dollars of loss [12]. Concerning cardiac diseases, animal models were demonstrated to be particularly inefficient because of the great anatomic difference between the animal heart and the human heart. Moreover, cardiac tissue is formed by distinct types of cells, and this complexity is hardly replicated in classical in-vitro cultures, leading to inappropriate modelling. The development of Heart-on-Chip platforms, where multiple types of cells can be cultured in 3D environments and that allow the development of more precise models for cardiac diseases has therefore main relevance.

It was discovered that cardiac cells derived from HiPSC, when cultured in-vitro, contract autonomously as if they were in a real heart [26]. These cells initially are not mature, but a full development may be reached if the correct stimuli (mainly mechanical load and electrical stimulation) are applied. Because of this need for mechanical stimulation, the cells are cultured in devices made of flexible polymers (mainly PDMS) and designed to have mechanical structures that can provide these loads such as micropillars, used as anchors.

The main interest at this stage of Heart-on-Chip development is reserved for the assessment of tissue's contractile properties in reaction to different stimuli (mechanical, electrical, or biochemical) and to drugs. These contractions are mainly measured via optical readout measurements, by evaluating the displacement of the pillars caused by the contraction and, knowing the force-displacement function (which is related to the stiffness of the structure), relating this displacement to the force applied by the tissues.

Multiple platforms have been reported in the literature with the objective to assess cultured heart cells' properties, and the following sections will analyse some of them.

A.3.1 Different platforms for EHT and HoC

In the literature, multiple Heart-on-Chip (HoC) or Engineered Heart Tissue (EHT) platforms are reported. The main differences between the platforms that can be found in the literature are reported in terms of the geometrical shape of the constructs, which can be various, and which determines the working principle of the platform. Figure A.4 illustrates different possibilities that have been designed or produced in the last decade.

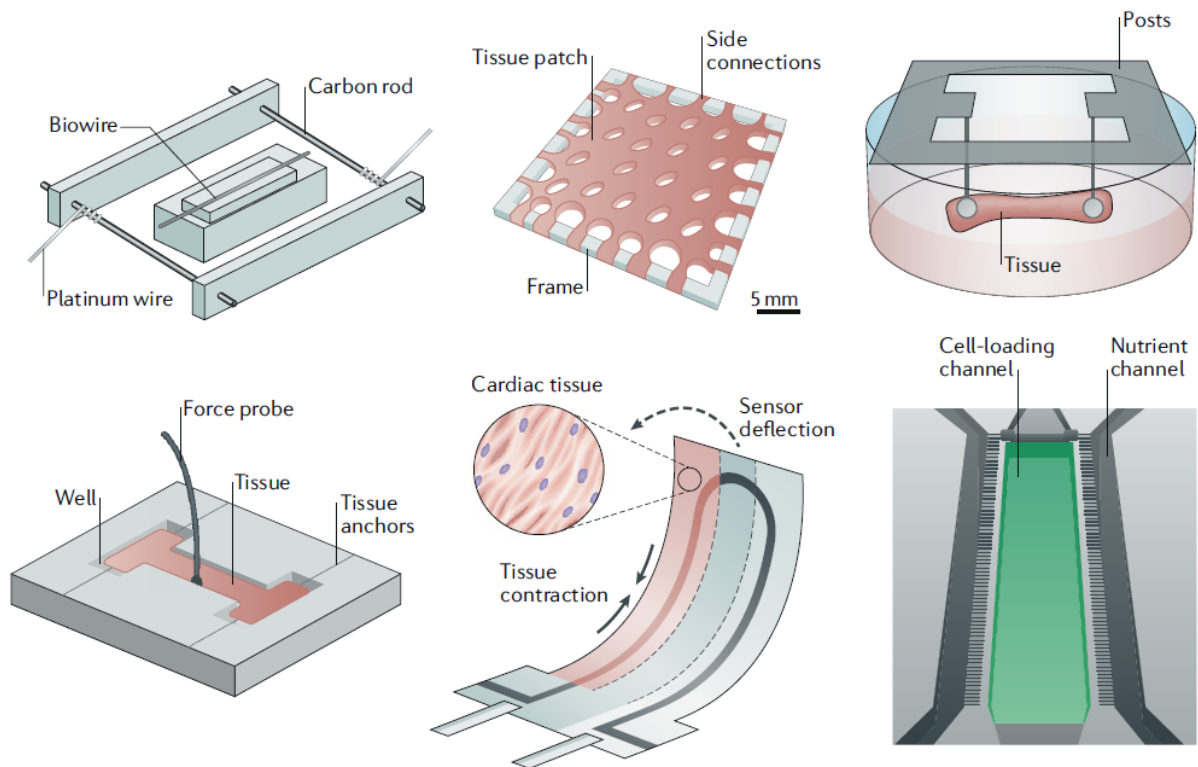


Figure A.4: Example of different Heart-on-Chip platforms (Derived from [11]).

Even when the geometrical shapes are similar, as in the case of the platform proposed by Dostanic [27] and Boudou [28], the purpose of the study might be different and therefore testing might require different measurement protocols.

Most frequently measures are made isometrically using a force transducer with no deformation or elongation of the tissue[29]. The main alternative is to optically record the deflection of the structure, but in this case, the force applied by the anchors to the tissue is constant and cannot be controlled. In the study of Boudou, different platforms that differed in the mechanical stiffness of the anchors were used, to assess the reaction of the tissue to this change in the stiffness of the structure. The study concluded that, even if cell alignment was reduced, the contractive capabilities of the tissue increased with a stiffer structure, meaning that the tissue could be “trained” as human muscle. The same study revealed that this increase in tissue functionalities was also obtained with electrical stimulations, thus demonstrating for the first time the impact of these physical aspects on the maturation and functionality of the engineered tissues [28].

The approach followed by Sidorov in the development of the so-called I-wire device [29, 30] brought the analysis of the tissue development related to mechanical stimulation to the next step. Using a structure created with PDMS casting molds and with a probe, it was possible to develop a system that could allow the real-time tuning of the stiffness of the structure by moving the probe through a magnetically actuated cantilever, without the need to use a different platform for different experiments. This solution created a way to control stiffness, thus creating a variable reactive force that generated tunable auxotonic contraction. The study concluded, in accordance with Boudou, that the stiffer the structure, the higher the contractive capabilities [29].

Marsano [31] used a different structure with pneumatic actuation to provide stimuli during the culture of the cells. This study concluded that not only mechanical stimulation improved contractive capabilities, but also caused a faster maturation of tissues during the culture process.

Since non-mature HiPSC are more similar to neonatal cells than to real heart cells [32], and since the predictive power of models developed with platforms that contain this type of cells is limited by

the cells' immaturity, a way to overcome this limitation and to reach a full maturation of HiPSC has been researched.

Particularly relevant for this project is the analysis of the platform developed by Parsa [33]: as in Marsano's study, this platform used pneumatic actuation to provide mechanical stimuli, but the most interesting part is related to the interface used for this actuation. This was performed with real-time on-chip circuitry that allowed individual loading, perfusing, and monitoring of the platform.

The trend to focus on real-time monitoring of the tissue is confirmed in a paper from Sakamiya [34]. In his platform, the monitoring of the tissue is not only continuous and in real-time but is also performed both with optical measurement and with piezoelectric sensors at the same time, using a readout as shown in Figure A.5. This approach, even if it does not push the limit to the integration of readout and/or sensor in the Heart-on-Chip platform, highlights the actual trend to progressively use other types of sensors integrated into the substrate that can assess the tissue functionality. These sensors are aimed to replace, or even better to accompany and work together with, the predominant optical sensing that is seen in most of the platforms.

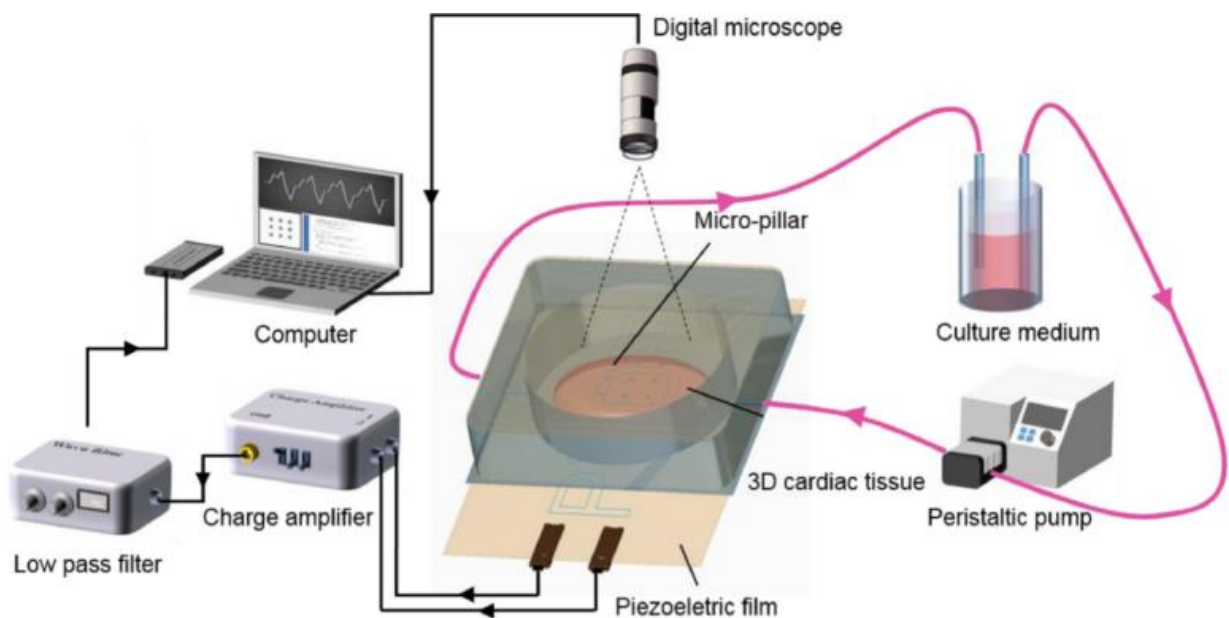


Figure A.5: Real-time online readout method used for the EHT platform (Derived from [34]).

A different approach for real-time monitoring was highlighted in Zhang's work [35], who developed a device containing a microfluidic channel for cell culture, platinum electrodes for stimulation of the tissue, and gold electrode arrays for the real-time in-situ acquisition of electrophysiological signals. An interesting aspect of this research was the test conducted on stimulated and non-stimulated tissues with reference drugs that were already known to influence the functionality of the human heart: only the stimulated tissues reacted to the drugs, thus showing the unreliability of models obtained with non-stimulated HiPSC [35]. But even more than this, what is relevant for this review is the fact that the contraction of tissue was measured electrically using gold electrodes. Even in this case, the array was connected to a multi-purpose biosensing platform and not to a "tailored" readout circuit, but this once more confirmed the trend to integrate the sensing in the platforms.

This specific topic is treated in a well-structured and complete review of sensing in Heart-on-Chip platforms [36]. In this review, the first sensing methodology illustrated is also the most widely diffused: optical sensing to measure the contraction of beating tissues. Because of its incapability to perform real-time measurements due to its time-consuming nature that requires complicated imaging

algorithms, this approach is gradually being substituted by alternative approaches. A possibility is constituted by electrical sensors, enabling reliable and real-time monitoring of cardiac functionalities. This is often performed using impedance or strain sensors, which have the drawback of directly exposing cells to current flow. Two more innovative techniques that can overcome the limitations of these types of sensors are based on electrodes allowing the monitoring of the electrophysiological signals, both outside the cells (extracellular) and inside the cells (intracellular), as also investigated in [37]. These techniques generally use Micro Electrode Arrays (MEAs) that can sense the electric potential change of the cells caused by ionic flow through the cellular membrane. The review concludes that the integration of advanced sensors in the platforms or the interaction of sensors with cardiac cell biology is expected to give a huge contribution to Heart-on-Chip technology, and is one of the priorities for future research [36].

To give an idea of the broad spectrum of possibilities offered by the EHT technology, completely different approaches to the OoC technologies started to appear in the last years. One example is the method proposed by Querdel [38], who created an EHT platform in a patch-like fashion to successfully muscularize an injured heart. Similar ideas are found in various research, as pointed out by Vunjak-Novakovic [39].

Table 2.1: Comparison of seven EHT platforms and their characteristics.

Reference	Year	Author	Tissue	Structure	Readout
[28]	2011	T. Boudou	Neonatal rat cardiomyocytes	Multiple platforms with flexible microcantilevers with different stiffness	High-speed imaging (No real-time)
[31]	2016	A. Marsano	Neonatal rat and HiPSC cardiomyocytes	Array of hanging posts and pneumatic actuation to induce strain	Imaging (No real-time)
[29]	2017	V. Sidorov	Neonatal rat cardiomyocytes	Well with two titanium wires as anchors and a flexible probe to provide strain via lateral displacement	High-speed imaging (No real-time)
[33]	2017	H. Parsa	Neonatal rat cardiomyocytes	Well with two micropillars and microchannels pneumatically controlled to induce strain in the tissue	Real-time on-chip circuitry to analyze tissue phenotype
[27]	2020	M. Dostanic	HiPSC cardiomyocytes and HiPSC cardiac fibroblasts	Platform with two flexible micropillars having constant stiffness	High-speed imaging (No real-time)
[34]	2020	M. Sakamiya	Neonatal rat cardiomyocytes	Micropillar array within a culture chamber	Online real-time monitoring via imaging and piezoelectric sensing
[35]	2021	F. Zhang	HiPSC cardiomyocytes	Platform with two rows of trapezoidal posts and with microfluidic channels	Gold electrode arrays for real-time recording of electrophysiological signals

As can be easily seen from this short analysis, the number of different platforms and research performed and developed around the topic of Heart-on-Chip is remarkably high. This makes it difficult to make a direct comparison between designs and between results obtained by separate groups with different tests. In this direction, international organizations are trying to push toward the creation of standards that can allow benchmarking and the comparison of results obtained across the world. Until then, in any case, a literature survey does allow the identification of general trends and of new shared directions to undertake in the future, as was highlighted in this section. Table A.1 summarizes the main platforms analyzed, listing their main characteristics.

A.4. Summary

This literature review presented a short and general introduction to the world of OoC and, in detail, to Heart-on-Chip technology. The primary features of general OoC platforms were analysed, and the relevance of this new field was explained thanks to the concrete reasons that pushed its development and that raised a huge interest in this field in the past years. The main organs that have been reproduced were shown, together with some of the diseases that motivated the development of relative platforms. OoC technology still presents some gaps to be filled before taking the leap between academia and industry, and these gaps have been listed and analysed shortly, together with the next steps to be taken to fill them.

The focus has then been moved to a specific OoC application: the one related to Engineered Heart Tissue. Typical characteristics shared by most of the available Heart-on-Chip platforms have been analysed, and the main reasons for developing such devices were presented. An examination of the literature tried to highlight the latest trends in the development of EHT platforms to identify potential future developments of EHT platforms. The literature search provided two main trends, namely the mechanical and electrical stimulation of the hiPSC tissue to obtain a more complete maturation of the tissue, and the integration of sensors in the platform to assess contractile properties and to progressively replace optical measurements.

References

- [1] "WYSS institute website." [Online]. Available: <https://wyss.harvard.edu/technology/human-organs-on-chips/>.
- [2] D. Huh, D. Matthews Benjamin, A. Mammoto, M. Montoya-Zavala, Y. Hsin Hong, and E. Ingber Donald, "Reconstituting Organ-Level Lung Functions on a Chip," *Science*, vol. 328, no. 5986, pp. 1662-1668, 2010/06/25 2010, doi: 10.1126/science.1188302.
- [3] B. Zhang and M. Radisic, "Organ-on-a-chip devices advance to market," (in eng), *Lab Chip*, vol. 17, no. 14, pp. 2395-2420, Jul 11 2017, doi: 10.1039/c6lc01554a.
- [4] Dutch-Foundation-for-Biosciences-and-Society, "Mini Organs-on-Chips: Towards new research models for studying disease and finding treatments," 2020. [Online]. Available: <https://www.biomaatschappij.nl/wp-content/uploads/2020/11/BWM-Mini-Organs-on-Chips.pdf>.
- [5] M. Mastrangeli, S. Millet, T. Orchid Partners, and J. Van den Eijnden-van Raaij, "Organ-on-chip in development: Towards a roadmap for organs-on-chip," (in eng), *Altex*, vol. 36, no. 4, pp. 650-668, 2019, doi: 10.14573/altex.1908271.
- [6] Mauriac, "Organs on chip review." [Online]. Available: <https://www.elveflow.com/microfluidic-reviews/organs-on-chip-3d-cell-culture/organs-chip-review/>.
- [7] S. S. Virani *et al.*, "Heart Disease and Stroke Statistics-2021 Update: A Report From the American Heart Association," (in eng), *Circulation*, vol. 143, no. 8, pp. e254-e743, Feb 23 2021, doi: 10.1161/cir.0000000000000950.
- [8] L. A. Low, C. Mummery, B. R. Berridge, C. P. Austin, and D. A. Tagle, "Organs-on-chips: into the next decade," *Nature Reviews Drug Discovery*, vol. 20, no. 5, pp. 345-361, 2021/05/01 2021, doi: 10.1038/s41573-020-0079-3.
- [9] A. van de Stolpe and J. den Toonder, "Workshop meeting report Organs-on-Chips: human disease models," *Lab on a Chip*, 10.1039/C3LC50248A vol. 13, no. 18, pp. 3449-3470, 2013, doi: 10.1039/C3LC50248A.
- [10] V. Palaninathan *et al.*, "Multi-organ on a chip for personalized precision medicine," *MRS Communications*, vol. 8, no. 3, pp. 652-667, 2018, doi: 10.1557/mrc.2018.148.
- [11] B. Zhang, A. Korolj, B. F. L. Lai, and M. Radisic, "Advances in organ-on-a-chip engineering," *Nature Reviews Materials*, vol. 3, no. 8, pp. 257-278, 2018/08/01 2018, doi: 10.1038/s41578-018-0034-7.
- [12] hDMT, "Organ-on-chip Technology and hDMT," 2016.
- [13] G. E. Moore, "Cramming more components onto integrated circuits, Reprinted from Electronics, volume 38, number 8, April 19, 1965, pp.114 ff," *IEEE Solid-State Circuits Society Newsletter*, vol. 11, no. 3, pp. 33-35, 2006, doi: 10.1109/N-SSC.2006.4785860.
- [14] J. W. Scannell, A. Blanckley, H. Boldon, and B. Warrington, "Diagnosing the decline in pharmaceutical R&D efficiency," *Nature Reviews Drug Discovery*, vol. 11, no. 3, pp. 191-200, 2012/03/01 2012, doi: 10.1038/nrd3681.
- [15] N. J. Schork, "Personalized medicine: Time for one-person trials," (in eng), *Nature*, vol. 520, no. 7549, pp. 609-11, Apr 30 2015, doi: 10.1038/520609a.
- [16] K. Takahashi and S. Yamanaka, "Induction of Pluripotent Stem Cells from Mouse Embryonic and Adult Fibroblast Cultures by Defined Factors," *Cell*, vol. 126, no. 4, pp. 663-676, 2006/08/25/ 2006, doi: <https://doi.org/10.1016/j.cell.2006.07.024>.
- [17] J. Theobald *et al.*, "In vitro metabolic activation of vitamin D3 by using a multi-compartment microfluidic liver-kidney organ on chip platform," *Scientific Reports*, vol. 9, no. 1, p. 4616, 2019/03/15 2019, doi: 10.1038/s41598-019-40851-9.
- [18] T. GmbH, "HUMIMIC Chip4." [Online]. Available: <https://www.tissuse.com/en/humimic/chips/humimic-chip4/>.
- [19] S. R. Moses, J. J. Adorno, A. F. Palmer, and J. W. Song, "Vessel-on-a-chip models for studying microvascular physiology, transport, and function in vitro," *American Journal of Physiology-Cell Physiology*, vol. 320, no. 1, pp. C92-C105, 2021/01/01 2020, doi: 10.1152/ajpcell.00355.2020.
- [20] Q. Zhang, L. Sito, M. Mao, J. He, Y. S. Zhang, and X. Zhao, "Current advances in skin-on-a-chip models for drug testing," (in eng), *Microphysiol Syst*, vol. 2, p. 4, 2018, doi: 10.21037/mps.2018.08.01.
- [21] A. Sontheimer-Phelps, B. A. Hassell, and D. E. Ingber, "Modelling cancer in microfluidic human organs-on-chips," *Nature Reviews Cancer*, vol. 19, no. 2, pp. 65-81, 2019/02/01 2019, doi: 10.1038/s41568-018-0104-6.
- [22] U. Senate, "FDA Modernization Act of 2021," 2021. [Online]. Available: <https://www.congress.gov/bill/117th-congress/senate-bill/2952>.
- [23] D. Huh *et al.*, "Microfabrication of human organs-on-chips," *Nature Protocols*, vol. 8, no. 11, pp. 2135-2157, 2013/11/01 2013, doi: 10.1038/nprot.2013.137.
- [24] M. W. Toepke and D. J. Beebe, "PDMS absorption of small molecules and consequences in microfluidic applications," (in eng), *Lab Chip*, vol. 6, no. 12, pp. 1484-6, Dec 2006, doi: 10.1039/b612140c.
- [25] ORCHID, "Organ-on-Chip In Development: ORCHID Final Report," 2020.

- [26] K. Ronaldson-Bouchard *et al.*, "Advanced maturation of human cardiac tissue grown from pluripotent stem cells," *Nature*, vol. 556, no. 7700, pp. 239-243, 2018/04/01 2018, doi: 10.1038/s41586-018-0016-3.
- [27] M. Dostanić *et al.*, "A Miniaturized EHT Platform for Accurate Measurements of Tissue Contractile Properties," *Journal of Microelectromechanical Systems*, vol. 29, no. 5, pp. 881-887, 2020, doi: 10.1109/JMEMS.2020.3011196.
- [28] T. Boudou *et al.*, "A Microfabricated Platform to Measure and Manipulate the Mechanics of Engineered Cardiac Microtissues," *Tissue Engineering Part A*, vol. 18, no. 9-10, pp. 910-919, 2012/05/01 2011, doi: 10.1089/ten.tea.2011.0341.
- [29] V. Y. Sidorov, P. C. Samson, T. N. Sidorova, J. M. Davidson, C. C. Lim, and J. P. Wiksw, "I-Wire Heart-on-a-Chip I: Three-dimensional cardiac tissue constructs for physiology and pharmacology," *Acta Biomaterialia*, vol. 48, pp. 68-78, 2017/01/15/ 2017, doi: <https://doi.org/10.1016/j.actbio.2016.11.009>.
- [30] A. K. Schroer, M. S. Shotwell, V. Y. Sidorov, J. P. Wiksw, and W. D. Merryman, "I-Wire Heart-on-a-Chip II: Biomechanical analysis of contractile, three-dimensional cardiomyocyte tissue constructs," *Acta Biomaterialia*, vol. 48, pp. 79-87, 2017/01/15/ 2017, doi: <https://doi.org/10.1016/j.actbio.2016.11.010>.
- [31] A. Marsano *et al.*, "Beating heart on a chip: a novel microfluidic platform to generate functional 3D cardiac microtissues," *Lab on a Chip*, 10.1039/C5LC01356A vol. 16, no. 3, pp. 599-610, 2016, doi: 10.1039/C5LC01356A.
- [32] E. Tzatzalos, O. J. Abilez, P. Shukla, and J. C. Wu, "Engineered heart tissues and induced pluripotent stem cells: Macro- and microstructures for disease modeling, drug screening, and translational studies," *Advanced Drug Delivery Reviews*, vol. 96, pp. 234-244, 2016/01/15/ 2016, doi: <https://doi.org/10.1016/j.addr.2015.09.010>.
- [33] H. Parsa, B. Z. Wang, and G. Vunjak-Novakovic, "A microfluidic platform for the high-throughput study of pathological cardiac hypertrophy," *Lab on a Chip*, 10.1039/C7LC00415J vol. 17, no. 19, pp. 3264-3271, 2017, doi: 10.1039/C7LC00415J.
- [34] M. Sakamiya, Y. Fang, X. Mo, J. Shen, and T. Zhang, "A heart-on-a-chip platform for online monitoring of contractile behavior via digital image processing and piezoelectric sensing technique," *Medical Engineering & Physics*, vol. 75, pp. 36-44, 2020/01/01/ 2020, doi: <https://doi.org/10.1016/j.medengphy.2019.10.001>.
- [35] F. Zhang *et al.*, "Design and fabrication of an integrated heart-on-a-chip platform for construction of cardiac tissue from human iPSC-derived cardiomyocytes and in situ evaluation of physiological function," *Biosensors and Bioelectronics*, vol. 179, p. 113080, 2021/05/01/ 2021, doi: <https://doi.org/10.1016/j.bios.2021.113080>.
- [36] K. W. Cho, W. H. Lee, B.-S. Kim, and D.-H. Kim, "Sensors in heart-on-a-chip: A review on recent progress," *Talanta*, vol. 219, p. 121269, 2020/11/01/ 2020, doi: <https://doi.org/10.1016/j.talanta.2020.121269>.
- [37] H. Liu *et al.*, "Heart-on-a-Chip Model with Integrated Extra- and Intracellular Bioelectronics for Monitoring Cardiac Electrophysiology under Acute Hypoxia," *Nano Letters*, vol. 20, no. 4, pp. 2585-2593, 2020/04/08 2020, doi: 10.1021/acs.nanolett.0c00076.
- [38] E. Querdel *et al.*, "Human Engineered Heart Tissue Patches Remuscularize the Injured Heart in a Dose-Dependent Manner," *Circulation*, vol. 143, no. 20, pp. 1991-2006, 2021/05/18 2021, doi: 10.1161/CIRCULATIONAHA.120.047904.
- [39] G. Vunjak-Novakovic, K. O. Lui, N. Tandon, and K. R. Chien, "Bioengineering Heart Muscle: A Paradigm for Regenerative Medicine," *Annual Review of Biomedical Engineering*, vol. 13, no. 1, pp. 245-267, 2011, doi: 10.1146/annurev-bioeng-071910-124701.

Appendix B

PCB schematics and layout

All the schematics and layout of the developed PCBs are listed in this appendix, together with a brief list of improvements in case of PCB re-design.

B.1. Capacitive board

Two versions of the board used to implement small variable capacitance have been developed.

B.1.1 Version 1

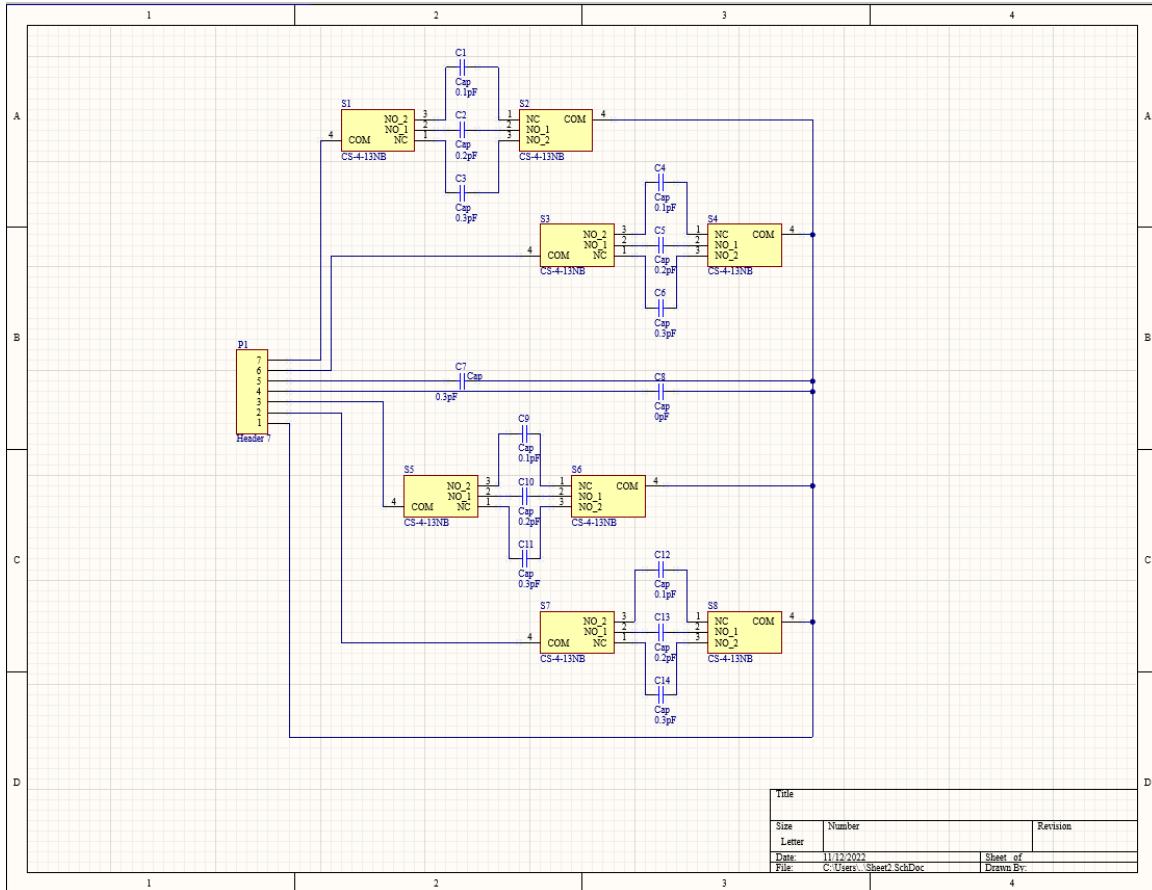


Figure B.1: Schematic of Capacitive Board V1

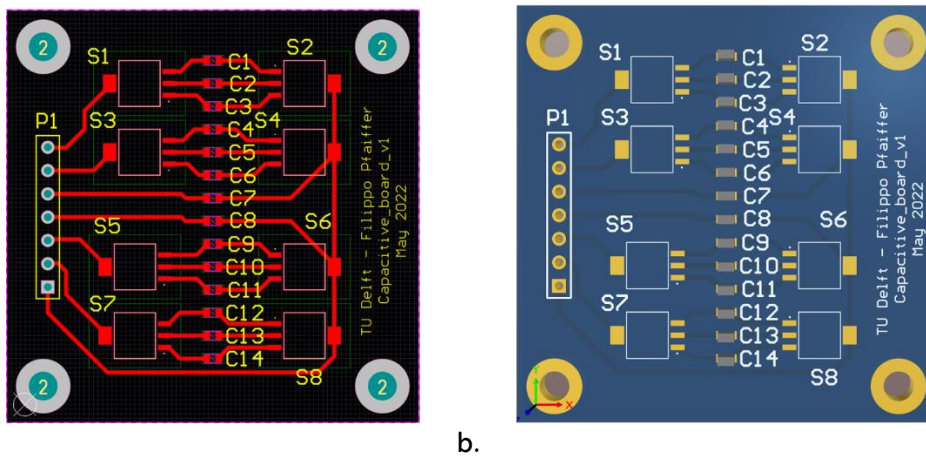


Figure B.2: Layout (a.) and 3D model (b.) of Capacitive Board V1

B.1.2 Version 2

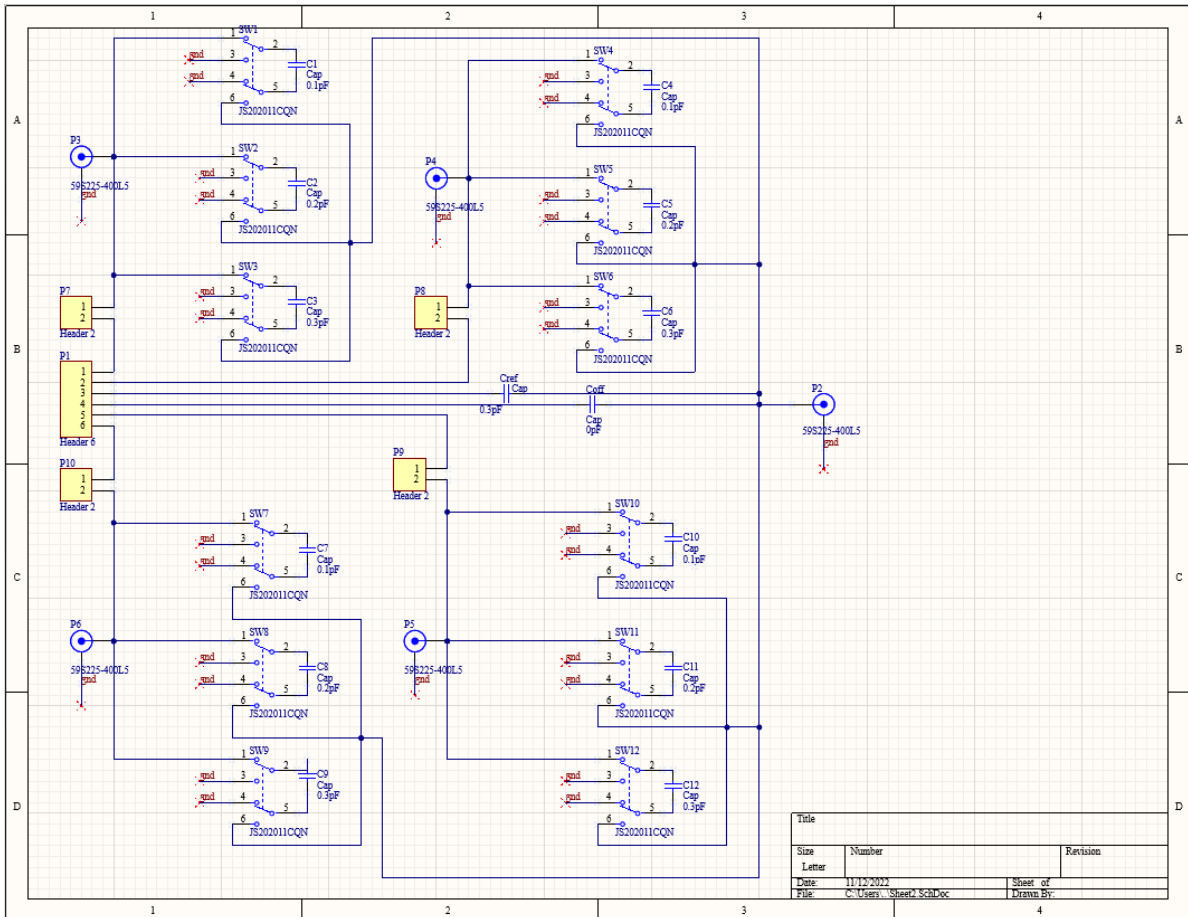


Figure B.3: Schematic of Capacitive Board V2

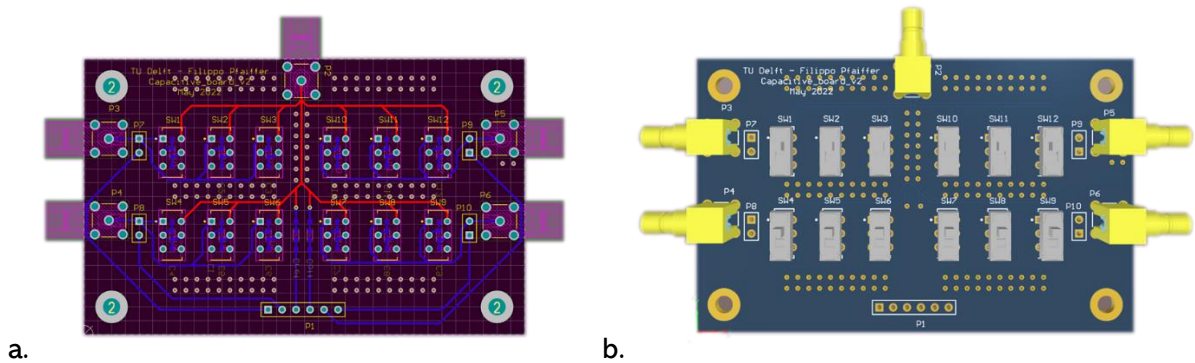


Figure B.4: Layout (a) and 3D model (b) of Capacitive Board V2

List of improvements:

- Addition of ground planes
- Addition of coaxial connectors
- Substitution of switches with Double Pole Double Through DPDT switches (allows grounding of non-connected capacitors)

B.2. UTI_To_Ali Board

This board was developed to allow the use of Heidary's improved version of UTI together with a standard UTI evaluation board.

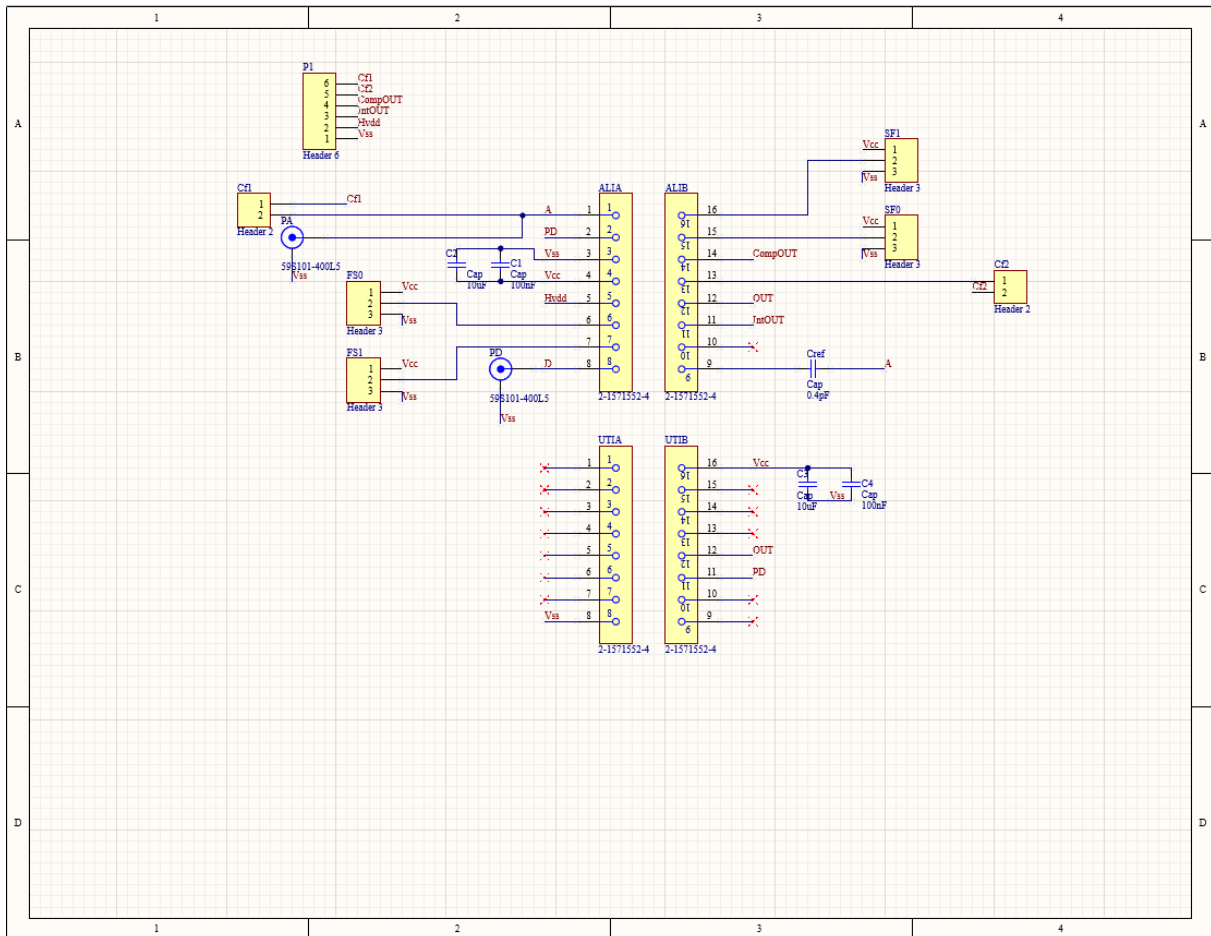
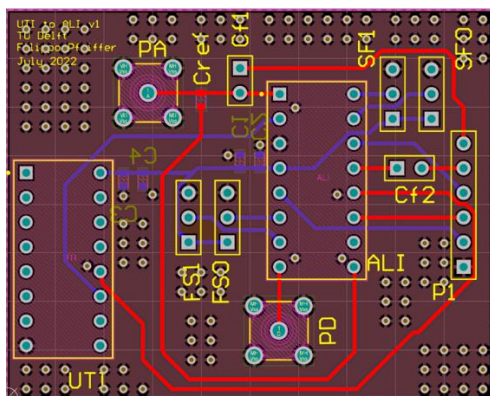
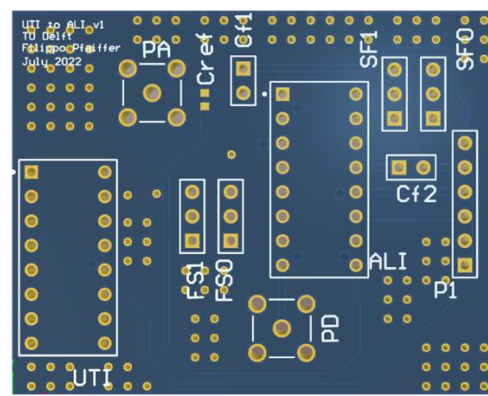


Figure B.5: Schematic of UTI_To_Ali Board



a.



b.

Figure B.6: Layout (a.) and 3D model (b.) of UTI_To_Ali Board

B.3. EHT_Wire_bonding board

Three versions of the board used to transfer and assemble EHT platforms have been developed.

B.3.1 Version 1

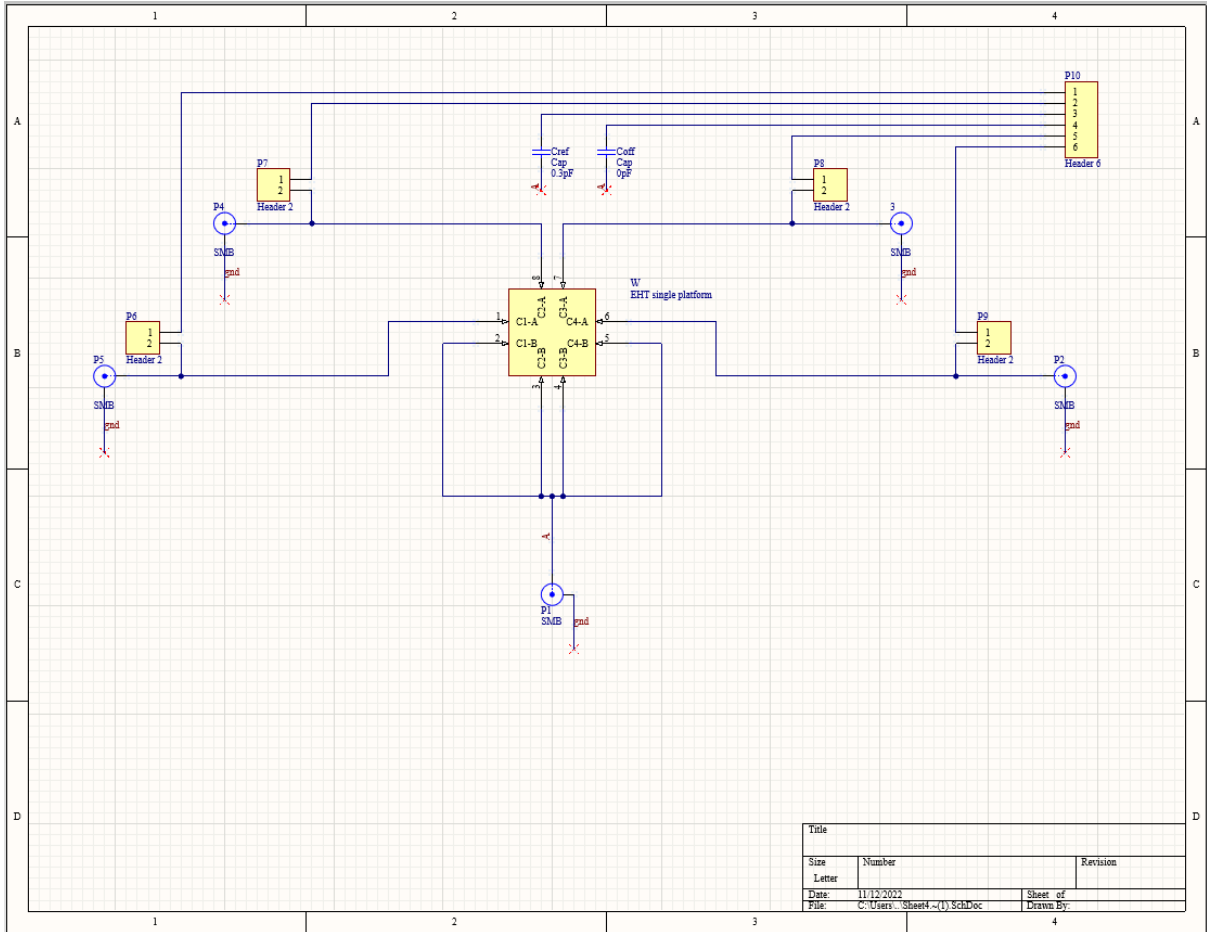


Figure B.7: Schematic of EHT_Wire_bonding V1

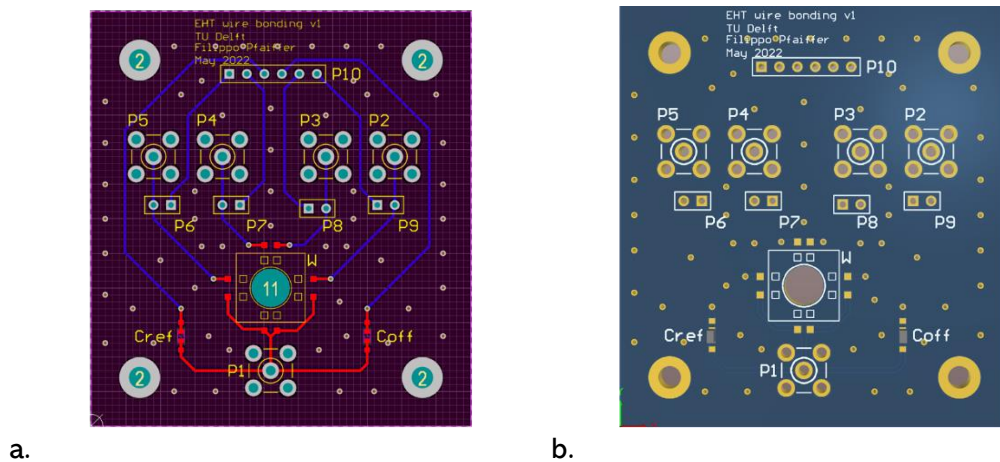


Figure B.8: Layout (a.) and 3D model (b.) of EHT_Wire_bonding Board V1

B.3.2 Version 2

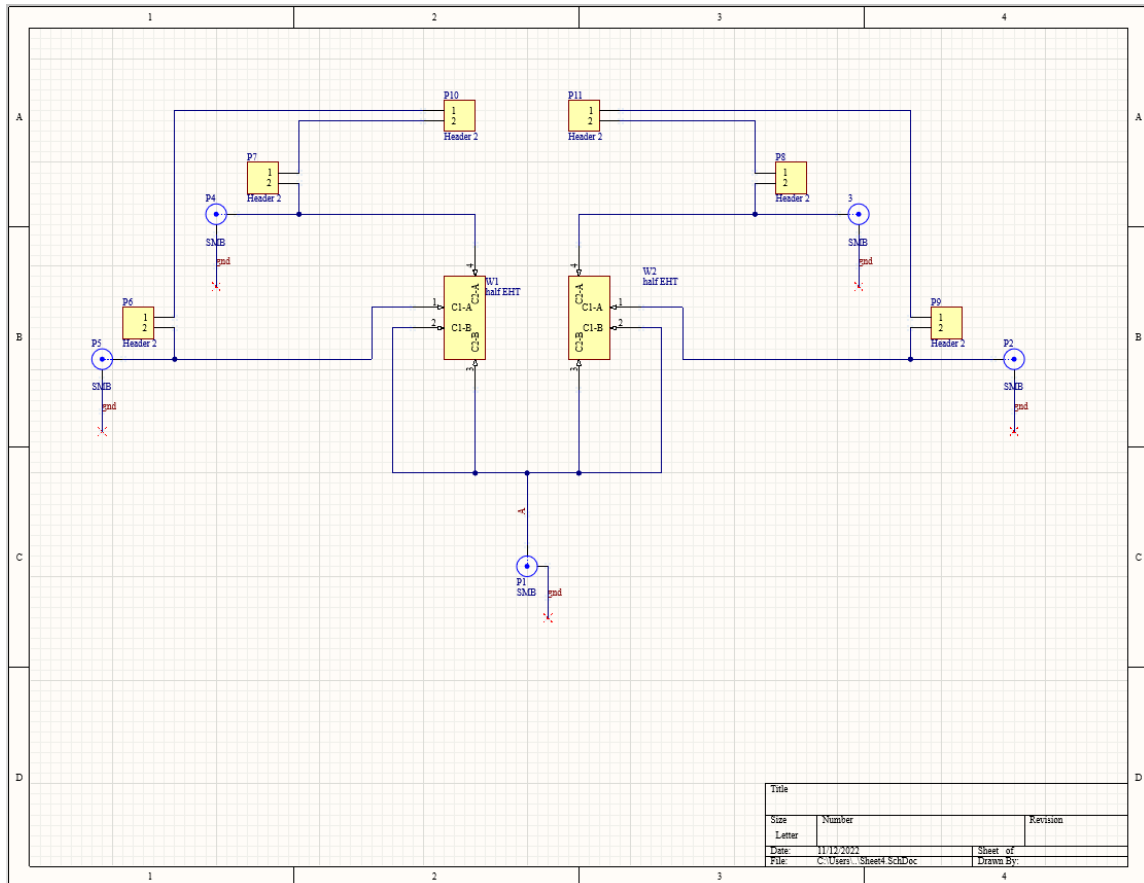


Figure B.9: Schematic of EHT_Wire_bonding Board V2

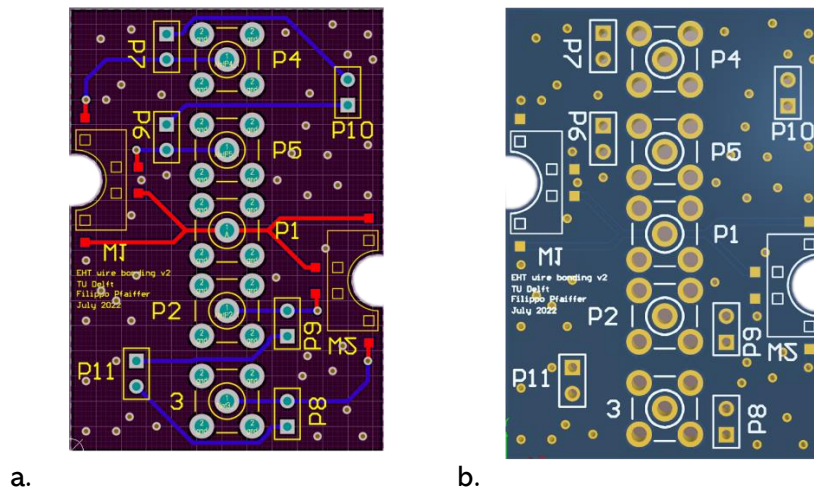


Figure B.10: Layout (a.) and 3D model (b.) of EHT_Wire_bonding Board V2

List of improvements:

- Change in the layout: two half wells placed at the edges of the board to allow nanoindentation of the pillars without presence of nanoindenter holder above the PCB.

B.3.3 Version 3

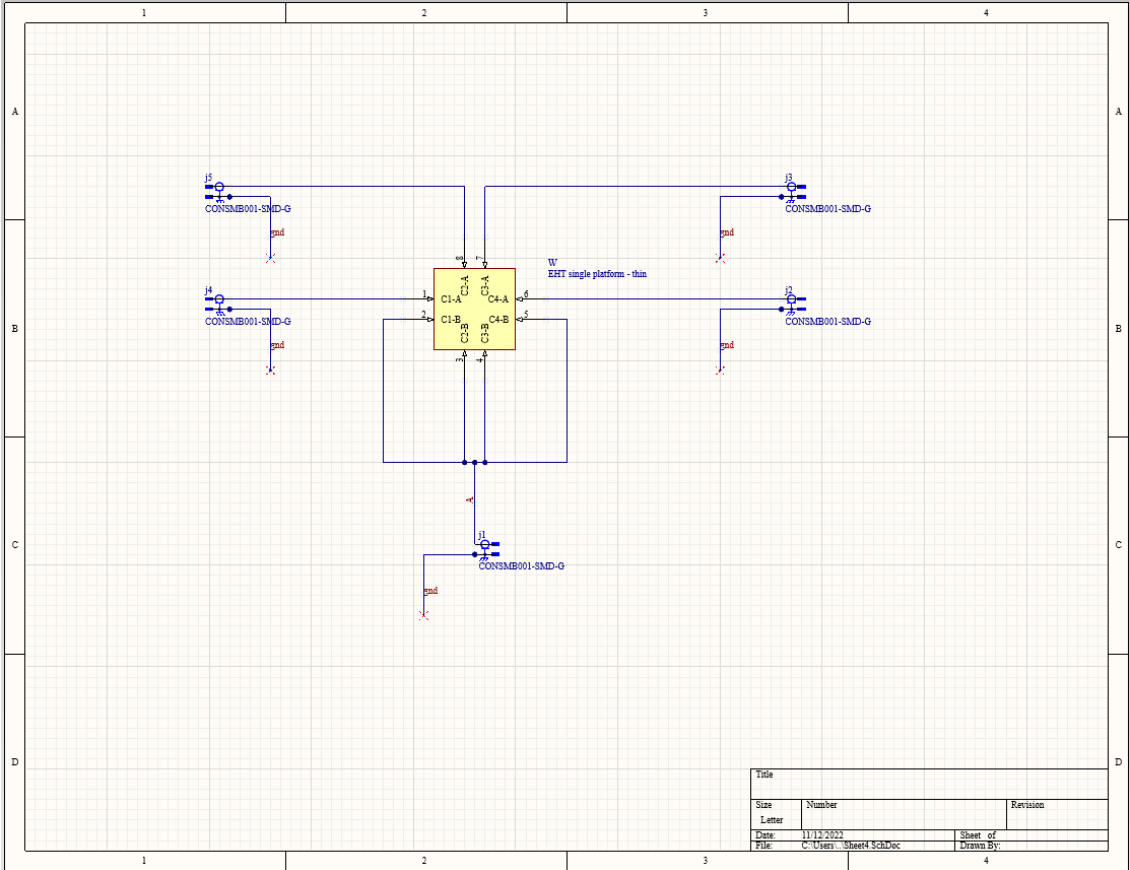


Figure B.11: Schematic of EHT_Wire_bonding Board V3

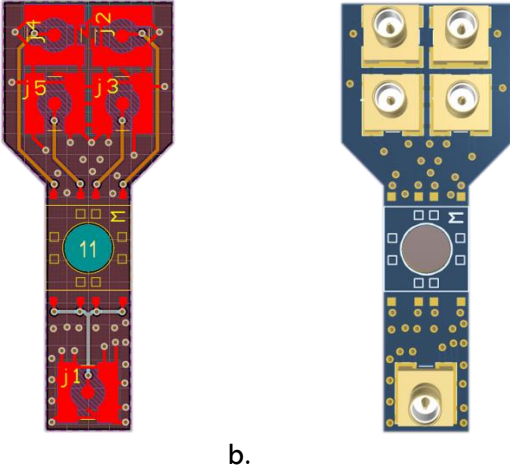


Figure B.12: Layout (a.) and 3D model (b.) of EHT_Wire_bonding Board V3

List of improvements:

- Use of SMD connectors
- Addition of two (top and bottom) copper grounded layers to shield the traces
- Change in the layout and shape of the board

B.4. Inverter_Buffer Board

This board was developed to try to implement a differential readout using UTI component. It was developed but never really tested.

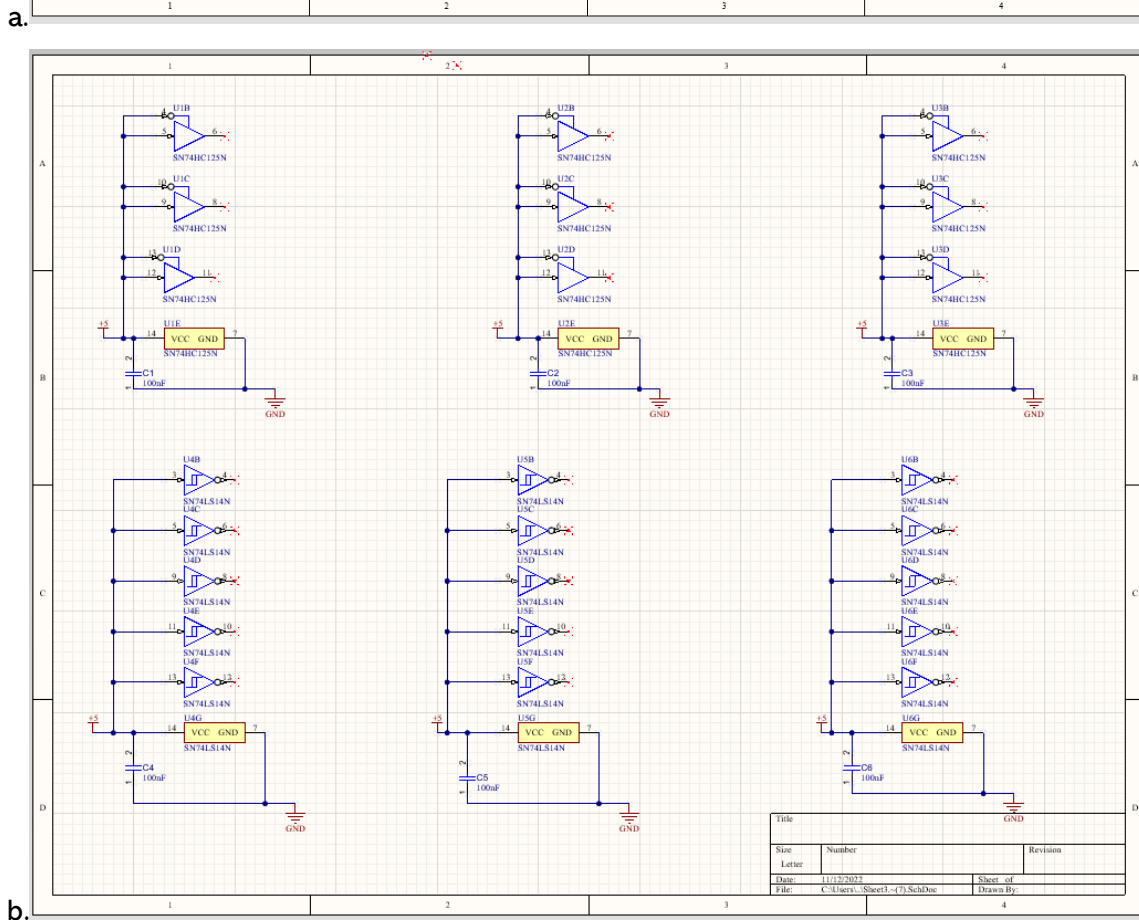
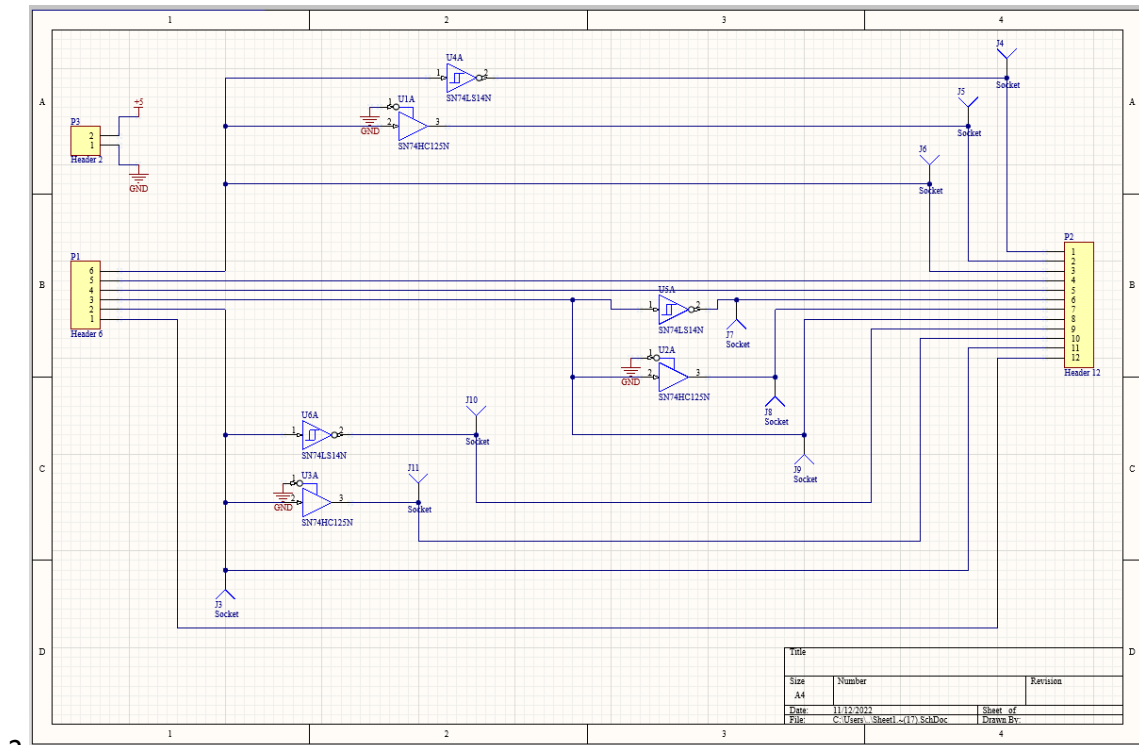


Figure B.13: Schematic sheets 1 (a.) and 2 (b.) of Inverter_Buffer Board

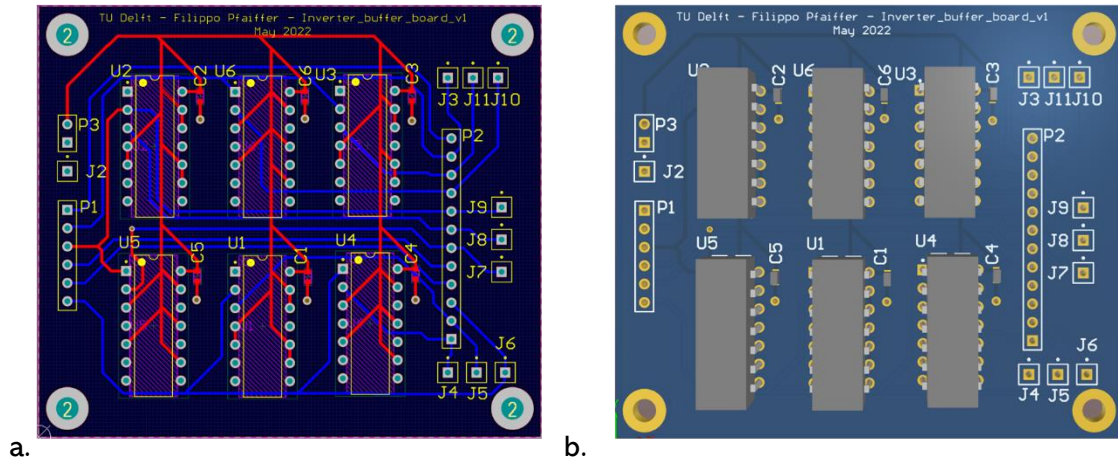


Figure B.14: Layout (a.) and 3D model (b.) of Inverter_Buffer Board

NOTE: The chosen components for inverter and buffer were respectively Texas Instruments SN74LS14 and Texas Instruments SN74HC125. Each component implements several structures, but the design choice was to use a single component for each signal, to avoid cross-couplings between the signals.

Appendix C

Datasheets of components

Datasheets relative to all the components used in relation to this project are provided at the following drive link:

<https://drive.google.com/drive/folders/1RyVYM8hGXvPlwA-Rn1clg9xSMV-5AgXV?usp=sharing>

Both datasheets for the components used in the developed PCBs are available, but also datasheets and manuals for all the instrumentation that was used for capacitive readout: not only UTI and AD7746, but also 4284A, 4294A, and U1732A.

The content of the directory is:

- 4284A Datasheet and Operation Manual
- 4294A Operation Manual
- AD7746 Datasheet and Evaluation Board Datasheet
- U1732A Datasheet
- UTI Datasheet and Evaluation Boards Datasheets
- SMB connectors datasheets (through hole and SMD)
- Switches Datasheets (x2)
- Capacitors Datasheets (x4)
- SN74HC125 Datasheet
- SN74LS14 Datasheet
- SMB coaxial cables Datasheet

Appendix D

Guide: how to connect and use AD7746

A quick guide related to setup and procedure to use the AD7746 component and evaluation board for capacitive readout is provided.

First, download the “AD7745_AD7746_Evaluation_Software.zip” directory at the following drive link:

<https://drive.google.com/drive/folders/1rWBSNecTqN4dm4gQZ8YEnThERDvzoK-u?usp=sharing>

Open the .exe file and start the setup. Follow the instructions and, once finished, the following app should be installed.

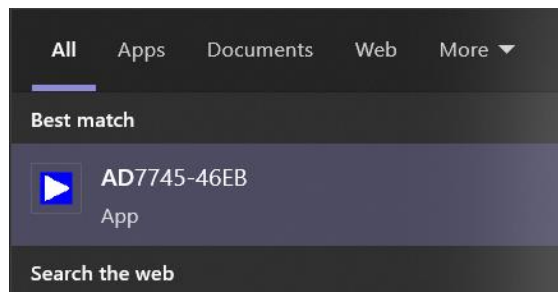


Figure D.1: AD7746 evaluation software icon.

Open the app. The following screen appears:

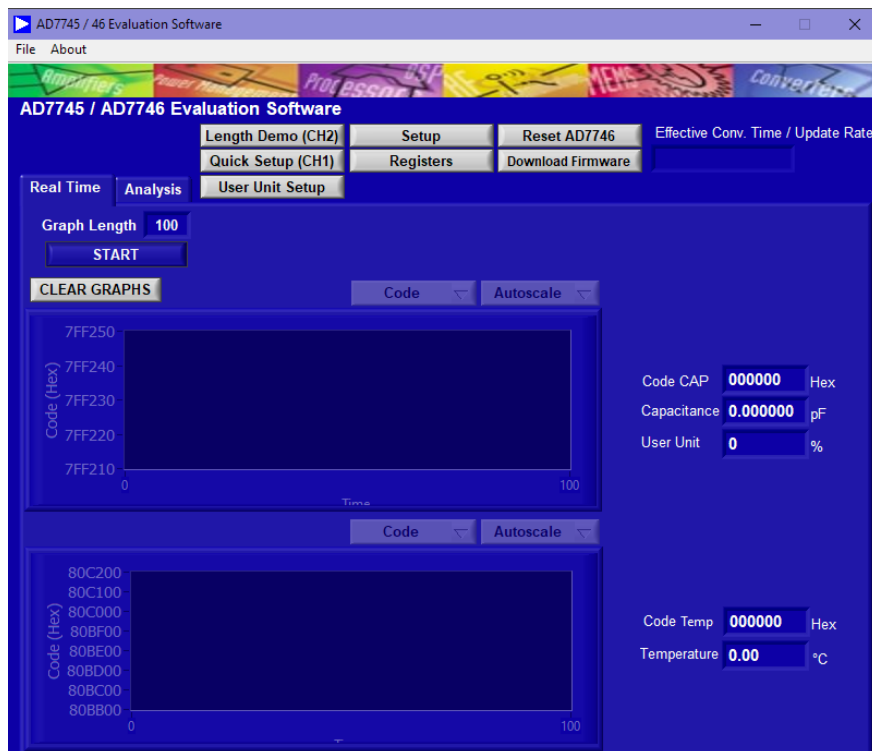


Figure D.2: AD7746 evaluation software user interface.

For this application, the only three relevant buttons in the top menu are *Setup*, *Reset AD7746*, and *Download firmware*. Firmware download should be automatically done when the program is opened with a board connected to the USB. If this is not the case, it can be downloaded again. AD7746 can be reset by clicking the button if something is not working for any reason.

Pressing on *Setup*, the following screen appears:



Figure D.3: AD7746 setup screen.

In the *Capacitive Channel Setup* group, “*Capacitive Channel Enable*” box should be ticked. *Conversion time* can be selected between the available options (62ms is the standard) and *Input* can be chosen between single-ended and differential (choose single-ended unless needed). Chopping can be enabled, doubling the conversion time (options related to conversion time will change when *Chop Enable* is ticked.)

In the *Excitation Voltage Setup* group tick both EXCA and EXCB buttons and leave the rest as it is, unless different specifications for the excitation signal are required.

Voltage/Temperature Channel Setup and *CAP DAC Setup* can be left as they are for this application.

In *Mode of Operation* menu, select continuous conversion. Click apply and ok. Compared to Figure D.2, the top graph will be highlighted when the setup window closes.

Select the number of points that will be visible in the real-time plot typing the number in *Graph Length* (ideal graph length depends on measurement time and on the application, in general 200 is a fair value). Click on *Code* and select *Capacitance* to change Y axis.

Click START and check if the graph starts filling with points.

If so, SMB cables can be connected. There are 4 SMB connectors on the board: for the measurement of one sensor, use the ones labelled with EXCA and CIN1+. When the cables are connected, a change in the readout level (parasitic form cables) should be visible, meaning that calibration needs to be performed.

Open again the setup and select *Mode of Operation* “Cap Offset Cal”. *Apply. Ok.*

Press START. Only one point will be acquired and then a message will appear. Click OK. Open again the setup and *Mode of Operation* will automatically be set to Idle.

Click it and select Continuous conversion again. *Apply, ok*.

By clicking START, the level of the acquisition should be now shifted to zero, meaning that the device is calibrated.

Connecting the sensor/capacitor to the SMB cables (order does not matter if a single capacitor is measured in single-ended input mode), the value of your sensor/capacitor should appear on the graph.

If Noise analysis needs to be performed, press on "*Analysis*" tab. Select *num of samples* (higher number provides more precise results but translates to longer time to perform the analysis). Click *Histogram* and select waveform, click *Codes* and select capacitance.

Click START (points will not appear on the graph until the acquisition is over). Once it is done, values can be checked on the right part of the screen.

This guide should contain all the information needed for the basic operation of the system. For a more detailed explanation and use of extra features, component and board datasheets can be consulted.

Appendix E

Naming of the sensors

A naming strategy was developed for identifying the different sensors. Every platform, after the fabrication process on the wafer, can be identified univocally by a letter (A, B, C, or D depending on the type), and by a number that depends on the positioning of the platform after fabrication. Figure E.1 shows the naming of each of the platforms produced on a wafer. This naming is given keeping the wafer's primary flat at the bottom.

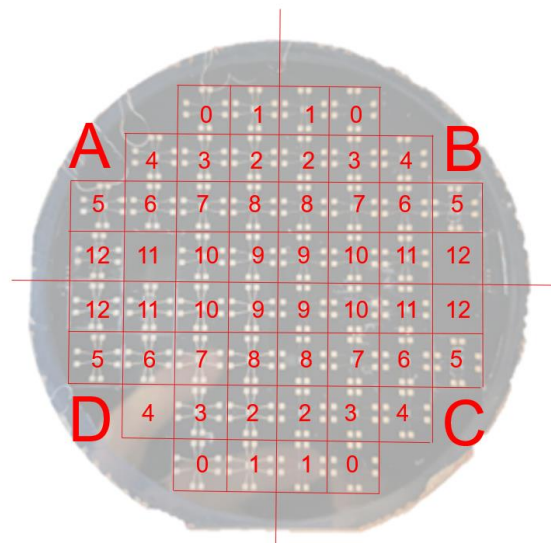


Figure E.1: Naming for the platforms.

Each platform has four sensors: keeping the orientation of the platform the same throughout the whole assembly process they can be identified using their position with a letter code that is listed below and can be seen in Figure E.2:

- L left
- ML middle left
- MR middle right
- R right

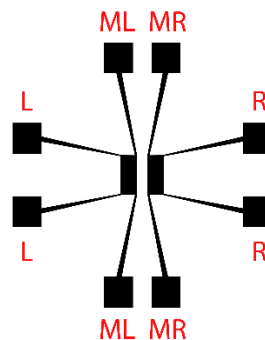


Figure E.2: Naming of the sensors.

So, for example, a sensor name can be B_10_MR. This code univocally identifies the sensors.

During assembly, the same orientation of the platform must be kept. This allows to identify which traces and therefore which connectors route the signal referred to a specific sensor. In the boards, there is always one connector that needs to be attached to pin EXCA/EXCB on the AD7746 evaluation board, and that routes this excitation to four electrodes, one for each sensor. The other four electrodes are connected to one coaxial connector each. Attaching one of these connectors to the EXC1+ pin of the evaluation board allows the readout of the sensors, whose signal is routed through the connector used. This relation between sensors and connectors is shown using labels in Figure E.3, keeping the naming previously used for the sensors.

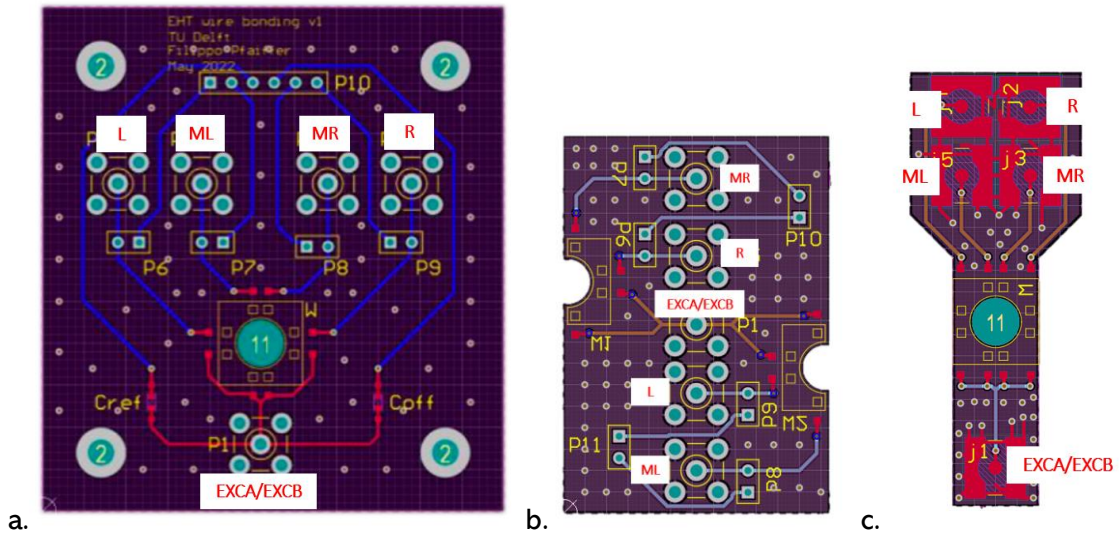


Figure E.3: Relation between connector used and sensor measured for the three developed boards.

Appendix F

MATLAB smoothdata: investigation

In Section 6.5 a smoothed version of a noisy signal was extracted using MATLAB function `smoothdata`. From the smoothed curve, the difference between the capacitive signal at the moment when no force is applied to the pillar and the capacitive signal at the moment when maximum force is applied (ΔC) was extracted.

Function `smoothdata` performs a moving average of the noisy signal to obtain a smooth curve. Obviously, the number of points averaged by the function (that can be given as parameter) affects the smoothing result: averaging fewer points will provide a curve that will follow more faithfully the original noisy dataset, while averaging more points will provide a smoother curve. This principle can be seen in Figure F.1.

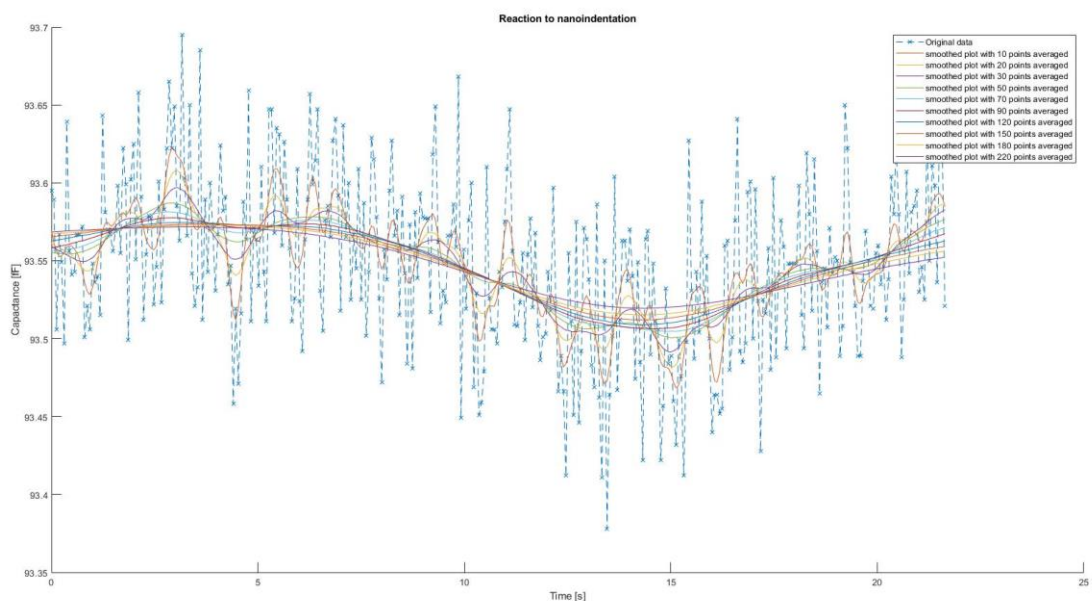


Figure F.1: Effect of different number of points used to calculate the moving average in `smoothdata` function.

Obviously, if we consider the error (the difference between the original noisy curve and the result of the smoothing for every point), it will be higher for a bigger number of points averaged, and lower for the smallest number.

The `smoothdata` function can also implement different methods for the smoothing (see <https://nl.mathworks.com/help/matlab/ref/smoothdata.html>), with each method having pros and cons and providing a different result for the smoothing. The curves obtained using `smoothdata` function with all the different smoothing methods available (using always the same number of averaged points) were plotted and provided the result shown in Figure F.2.

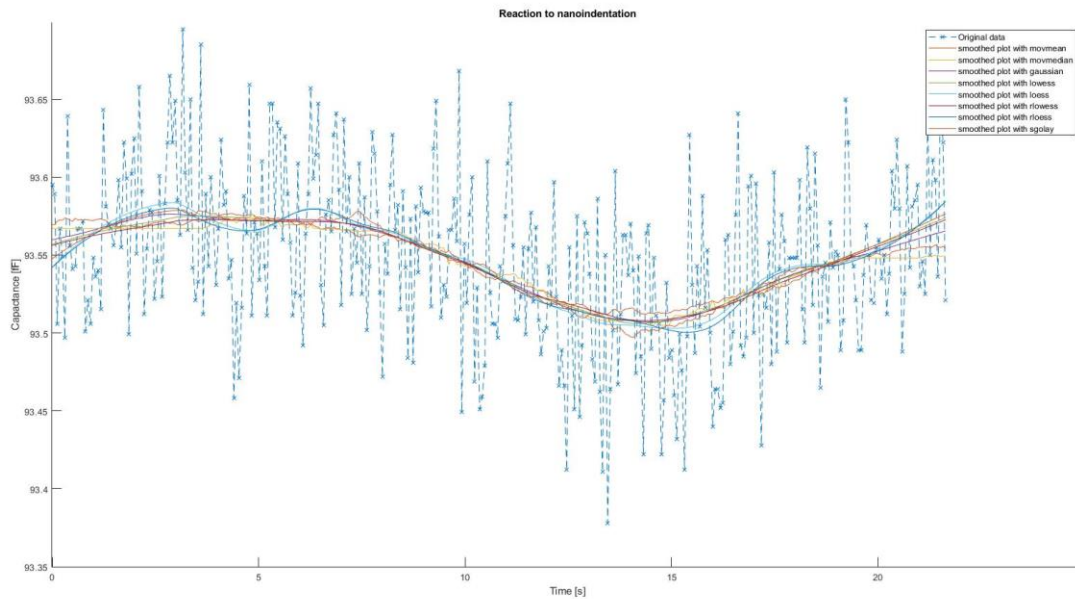


Figure F.2: Effect of different methods used to perform smoothdata function.

This proves that also the method used for the smoothing influences the result of the smoothing. Obviously, different methods or different numbers of points provide different curves, which will therefore provide a different ΔC for the same set of original data. Since there is no unique and correct solution when trying to clean noisy data and to reconstruct an underlying signal, it is not possible to identify a correct method or a correct number of points to be averaged to provide the correct result. The result obtained will in every case be an approximation.

A good method for this type of problems is to use Gaussian Process Regression (GPR), which is a stochastic process that assumes that the signal that underlies the noisy dataset is affected by gaussian white noise, and does not provide a precise line as result, but provides confidence intervals within which the real signal is likely to underlie.

This method was investigated, and the smoothdata function with method and number of points providing the closest signal to the confidence interval obtained using GPR method was chosen for the final implementation of the smoothing. This method was therefore set to "Gaussian", and averaged number of points to "100". Extraction of ΔC with these parameters was therefore performed on all the noisy curves obtained with different measurements, and the results obtained were used to generate the plot of Figures 6.15-6.16-6.17. In any case, the extraction of the different ΔC was also experimented using different methods and different number of averaged points. Obviously, these attempts provided different smoothed curves, and different values for ΔC associated with the same noisy signal. In any case, it was noticed (as expected) that the different methods used and the different number of points affected all the curves in the same way, increasing or reducing the ΔC in similar ways for every different dataset smoothed using the same method/number of points averaged.

From this evaluation, it must therefore be clear that, even using different methods or different number of averaged points compared to the ones used within the scope of this thesis, the general trends shown in Figures 6.15-6.16-6.17 are confirmed. The absolute values of the data will be different, the slopes might face slight variations, but the principle and the behaviour of the curves will be, within a reasonable margin, unaltered.

Appendix G

Videos and recordings

Some videos of the most interesting measurements and of the most critical failure modes were recorded and are available at the following drive link:

https://drive.google.com/drive/folders/1UK4rp9EZsp_MRE_byC55ighvRSxATEwC?usp=sharing

The content of the directory is:

- Recording of manual displacement of the pillar
- Recording of nanoindentation
- Recording of failure related to wire bonding

Appendix H

LabVIEW for UTI interfacing

A LabVIEW project for interfacing with Smartec UTI was developed by the company, and provided. It is contained in a .zip directory at the following drive link:

https://drive.google.com/drive/folders/1p74_BUDOWPiuX-ZrASOjb-1BLDkWDxcz?usp=sharing

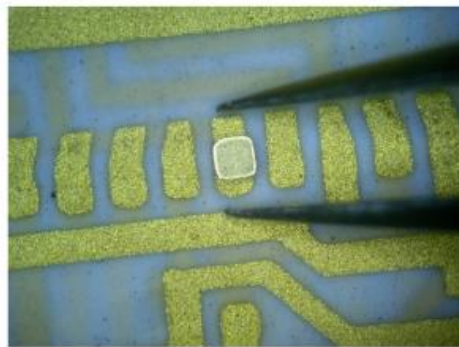
In the Uti.LLB file multiple versions can be found: Uti.vi is the original file. Some modifications were performed during this Master Thesis to adapt the file to the needs, and are provided in the same Uti.LLB file. Uti_v2.vi displays the value of all three unknown capacitors instead that only the value of the first one. Uti_noise_fast.vi is a modification to display data acquired using the fast evaluation board (70MHz), and Uti_noise_fast_matlab.vi has extra blocks that allow the communication between LabVIEW and MATLAB to automatically plot the recorded data on MATLAB as soon as the recording is stopped.

Appendix I

Gold shims - reference material

Bonding Source gold plated shims/pedestals ([Gold Plated Bonding Shims-In Stock \(bondingsource.com\)](http://bondingsource.com)) were used to allow wire bonding of the sensors to the PCBs. Data provided by the manufacturing company can be accessed below.

bonding source



About the Bonding Shims:

Molybdenum Characteristics:

- Low co-efficient of thermal expansion (5.1×10^{-6} m/m/°C) which is about half that of most steels
- Good thermal conductivity
- Good electrical conductivity
- Good stiffness, greater than that of steel (Young's Modulus 317MPa)
- High melting point (2615°C)
- Good hot strength
- Good strength and ductility at room temperature
- High density (10.2 g/cm^3)

The "moly shim" is plated with 50 microinches of nickel minimum, under 50 microinches minimum of gold.

The shims are typically soldered to the circuit board or epoxied with electrically conductive epoxy. Once attached to the circuit or substrate, you can wire bond or solder to the top of the shim. It's great to have a vial of these in the assembly area in the event you get solder on a bond site, damage a trace, or need a standoff.

www.bondingsource.com

603-595-9600

Appendix J

Wire bonding parameters

TPT HB30 (<https://www.tpt-wirebonder.com/hb30/>) Heavy Wire Bonder that can be found at EKL facilities at TU Delft was used for the wire bonding of the sensors and the platforms. The first bond was performed on the gold shim and the second on gold bonding pads placed on the support PCB. HB30 allows, for each of the two bonds, the setting of parameters related to the bonding, such as ultrasonic power, time and force applied by the tip during the bonding. These parameters need to be selected in function of the substrate, the material of the wire and the material of the contact. The investigated parameters for the application treated in this Master Thesis (first bond on Au shim and second bond on Au contact pad on PCB) are shown in Figure J.1.

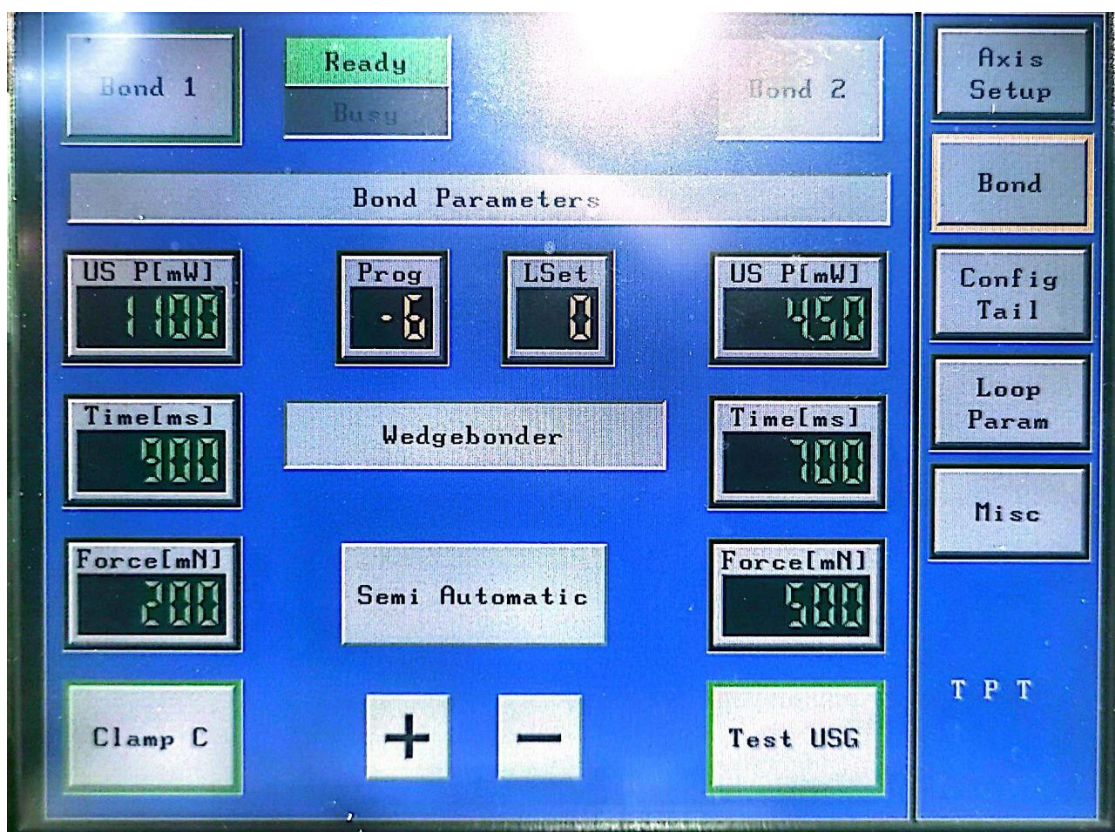


Figure J.1: HP30 bonding parameters.

Appendix K

Fabrication process with Polyimide

A fabrication process using polyimide (PI) as a stress buffer and insulation layer between the PDMS substrate and the aluminum traces was previously developed for similar applications, and is shown in Figure K.1. It was discarded in relation to this application because it would have altered the mechanical properties of the structure, lowering the responsivity of the sensors.

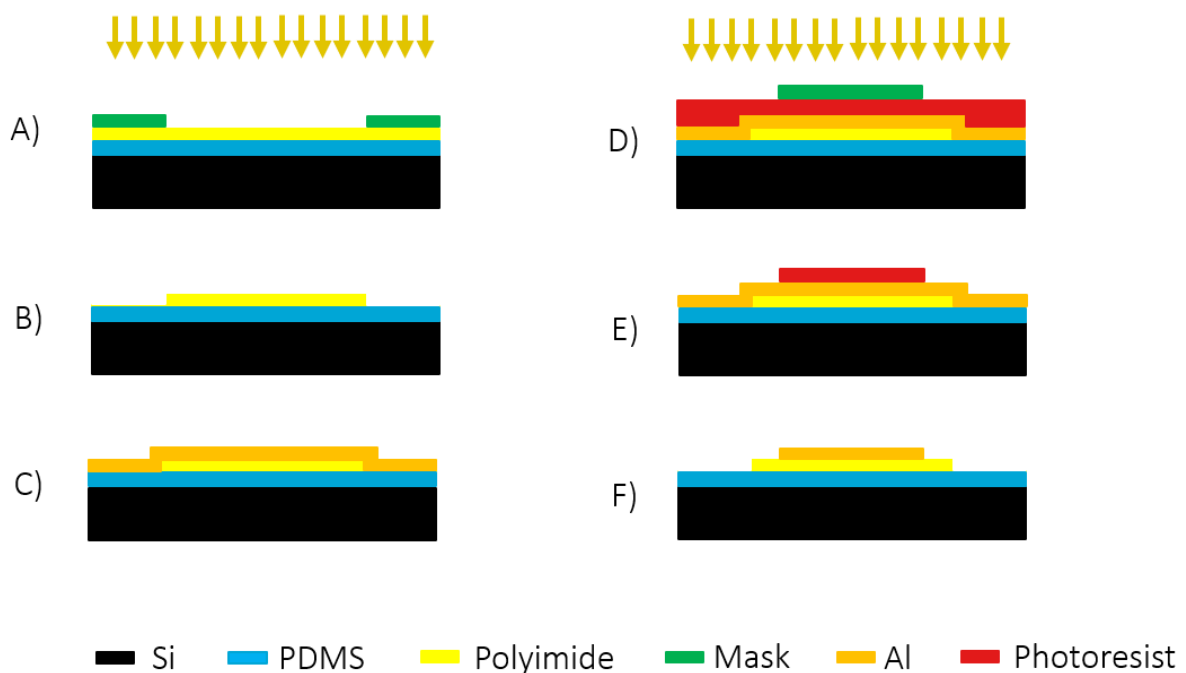


Figure K.1: Fabrication process with polyimide buffering layer.

A thin polyimide layer is spincoated on top of PDMS substrate. Since PI behaves as a negative photoresist, photolithography is used to pattern the desired structures using a mask (Figure K.1A). Development provides the patterned PI structure (Figure K.1B) on top of which aluminium is sputtered (Figure K.1C). Wafer is then coated with positive photoresist and a different mask is used for this second photolithography step (Figure K.1D). Figure K.1E shows the cross-section of the process after development. The aluminium layer with photoresist is then patterned using reactive ion etching. The final result is shown in Figure K.1F: a thin layer of polyimide serves as a stress buffer between the spin-coated PDMS and sputtered metal later, as it encapsulates Al interconnects and contact pads.

